École polytechnique de Louvain

Experimental characterization of an axisymmetric supersonic air ejector

Authors: **Loric BROSTEAUX, Quentin DOUCET**
Supervisors: **Yann BARTOSIEWICZ, Grégoire WINCKELMANS**
Readers: **Philippe CHATELAIN, Romain DEBROEYER**
Academic year 2023–2024
Master [120] in Mechanical Engineering

Acknowledgments

Nous tenons à exprimer notre profonde gratitude à toutes les personnes qui ont contribué à la réalisation de ce mémoire.

Tout d'abord, nous remercions chaleureusement nos promoteurs, les Professeurs Yann Bartosiewicz et Grégoire Winckelmans, pour leur encadrement, leurs conseils avisés et leur soutien lors des diverses réunions.

Nous souhaitons également remercier Romain Debroeyer qui nous a accompagnés avec dévouement et rigueur. Son aide précieuse dans les moments clés de notre travail et sa disponibilité ont grandement facilité la réalisation de ce mémoire.

Nous exprimons notre gratitude aux techniciens de la plateforme CREDEM, et plus spécialement à Hervé, Julien, Frank, Victor, Arnaud et Vincent. Leur compétences techniques et leur aide logistique ont été indispensables pour la mise en place et le bon fonctionnement du montage expérimental. Merci aussi à Benoît Herman pour ses conseils et son aide.

Nous voulons aussi remercier Grégoire et Pascal d'Atelier François, pour leur aide, leur disponibilité et leur confiance quant à l'utilisation du compresseur.

Nous tenons également à remercier nos prédécesseurs, Guillaume et Nicolas, dont le travail précédent a servi de base solide à notre recherche et qui furent présents et disponibles tout au long de l'année pour répondre à nos questions.

Enfin, un grand merci à nos proches pour leur soutien inébranlable, leur patience et leur encouragement tout au long de cette aventure. Leur présence à nos côtés a été un pilier essentiel pour nous permettre d'avancer sereinement.

Utilisation de l'IA

L'intelligence artificielle ChatGPT a été utilisée comme outil d'amélioration de l'écriture et de correction orthographique.

Abstract

Supersonic ejectors are passive components in thermodynamic cycles, functioning as compressors that utilize two streams of fluid. The primary stream, characterized by high stagnation pressure, entrains the secondary stream, which has a lower stagnation pressure. The two streams mix in a constant-area duct, where momentum and energy are exchanged. The mixed flow is then expanded through a diverging section and reaches an intermediate pressure that matches the downstream conditions.

Thanks to their ability to operate on low-grade energy, such as waste heat, solar energy, and renewable energies in general, supersonic ejectors have attracted more and more attention at a time when finding solutions to climate change has become a priority. Additionally, since ejectors are passive devices, their maintenance requirements and overall costs are relatively low.

Studies on supersonic ejectors have been conducted for decades, beginning with 1-D models and recently advancing to 2-D and 3-D analyses using Computational Fluid Dynamics (CFD) simulations. The need to study ejectors is driven by their relatively low performance in refrigeration cycles, as measured by the Coefficient of Performance (COP). Although their use of low-grade energy sources is appealing, they still cannot compete with traditional compressors in terms of efficiency.

The purpose of this Master's thesis is then clearly drawn: better understand the behavior of supersonic ejectors, and in particular, how do the experimental results compare to 2D Reynolds-Average Navier-Stokes (RANS) simulations, based on an axisymmetric ejector designed and analysed numerically during a previous Master's thesis. The experimental setup must be made fully operational before commencing the testing campaign. Once the setup is operational, measurements are taken under various operating conditions. The reliability of measurements is ensured through an extensive evaluation of their uncertainty. The resulting data is then set side by side with the results from the RANS simulations, and this comparison enables qualitative and quantitative analyses aimed at explaining the observed discrepancies.

Contents

Nomenclature

Abbreviations

CFD	Computational Fluid Dynamics
DAQ	Data Acquisition
DNS	Direct Numerical Simulation
EXP	Experimental
FANS	Favre-Averaged Navier-Stokes
GUM	Guide to the expression of Uncertainty in Measurement
LES	Large Eddy Simulation
NXP	Nozzle Exit Position
P&ID	Piping & Instrumentation Diagram
RANS	Reynolds-Averaged Navier-Stokes

Greek letters

β	Compound-flow indicator	[-]
Δ	Variation of any quantity	
δ	Small difference between variables	
ϵ	Expansibility factor	[-]
η	Efficiency	[-]
γ	Isentropic exponent	[-]
μ	Dynamic viscosity	[Pa s]
ν	Number of degrees of freedom in t-distribution	[-]
ϕ	Relative humidity	[-]
ρ	Static density	[kg/m^3]
σ	Standard deviation	

ξ	Diameter ratio	[-]

Alpha numeric symbols

$\dot{m}$	Mass flow rate	[kg/s]
A	Cross-sectional area	[m^2]
A_m	Mixing duct cross-sectional area	[m^2]
A_t	Throat cross-section area	[m^2]
C_d	Discharge coefficient	[-]
c_i	Sensitivity coefficient	
D	Pipe diameter	[m]
d	Orifice diameter	[m]
ER	Entrainment ratio	[-]
f	Function	
I	Invariant term	
k_p	Coverage factor	[-]
M	Mach number	[-]
M_m	Molar mass	[kg/mol]
M_{eq}	Equivalent Mach number	[-]
MFP	Mass Flow Parameter	[m s $\sqrt{K}$]
p	Static pressure	[Pa]
p^*	Critical sonic pressure	[Pa]
$p^*_{0,out}$	Critical back-pressure	[Pa]
$p^b_{0,out}$	Break-down back-pressure	[Pa]
p_0	Total (stagnation) pressure	[Pa]
p^*_{eq}	Static pressure corresponding to the compound-choking condition	[Pa]
p_{sat}	Saturation vapor pressure	[Pa]
R	Specific gas constant	[J/(kg K)]
r	Correlation coefficient	
R_u	Universal gas constant	[J/(mol K)]
Re	Reynolds number	[-]

s	Experimental standard deviation	
T	Static temperature	[K]
t	Static temperature	[°C]
t_p	t-factor	[-]
U	Expanded uncertainty	
u	Standard uncertainty	
u_c	Combined standard uncertainty	
x	Axial coordinate	[m]
X_i	Measured quantity	
x_i	Estimate of X_i	
x_v	Absolute humidity	[$\mathrm{kg}_w/\mathrm{kg}_{da}$]
Y	Measurand	
y	Estimate of Y	

Operators

$\bar{\cdot}$	Average over independent measurements

Subscripts

0	Reservoir conditions	
1	Related to the primary stream	
2	Related to the secondary stream	
a	Related to upstream of the orifice plate	
b	Related to downstream of the orifice plate	
d	Related to the diffuser	
da	Related to dry air	
m	Related to the mixing	
out	Related to the ejector outlet	
p	Coverage probability	[-]
w	Related to water	
y	Related to the hypothetical throat	

Chapter 1

Introduction

1.1 Context

Supersonic ejectors are passive devices used in engineering applications where a fluid must be compressed. They consist of a high pressure primary stream that reaches supersonic speed through a converging-diverging nozzle. A secondary stream is entrained by the primary stream and accelerated through the exchange of momentum and energy. The two streams mix in a constant-area section, where a series of oblique shocks increases the pressure of the mixture and decreases its speed. Finally, the resulting fluid is expanded through a diverging section to match downstream conditions.

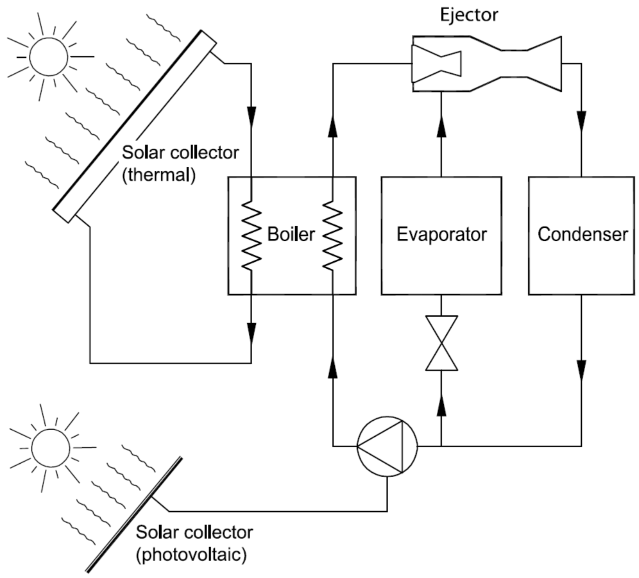

Figure 1.1: The use of an ejector in a refrigeration cycle. [1]

One of the main applications where a supersonic ejector can be used is in refrigeration cycles (Figure 1.1), where it serves as the compressor. In this application, the fluid exiting the condenser is separated into two streams. The first stream is compressed with a pump, heated through a boiler, and becomes the primary stream of the ejector, which then entrains the secondary stream. The secondary stream follows the typical refrigeration cycle: it is first expanded, then exchanges heat in the evaporator, and is subsequently sucked into the ejector. The mixed and compressed fluid at the outlet continues the cycle.

An advantage of using this device lies in the heat source provided to the boiler. Indeed, supersonic air ejectors only require low-quality energy sources, such as waste heat from industrial processes, solar energy, and renewable energies in general. In an era where environmental issues are a major problem to tackle, using supersonic air ejectors may be a viable solution, which aligns well with the growth of renewable energies. Additionally, as passive devices without any moving parts, supersonic ejectors are easier to manufacture and maintain, resulting in relatively low maintenance and operation costs.

According to Elbel and Hrnjak [2], the study of ejector-type devices dates back to the mid-19th century when Henry Giffard invented a condensing-type injector used in steam engine boilers to refill their reservoirs. The term "injector" is typically used when the outlet pressure can reach that of the primary fluid, whereas it is referred to as an "ejector" when the exit pressure is closer to that of the secondary fluid. However, the fundamental principle remains the same, and Henry Giffard's work represents the earliest exploration of this type of device. In the early 20th century, low-grade energy source cycles emerged, notably with the work of Leblanc in 1910, who utilized a vapor jet ejector to produce a refrigeration effect. This system found applications in the air-conditioning of large buildings and railway wagons.

The first 1-D model of an ejector originated from the studies of Keenan et al. [3]. This model was further developed with the introduction of the Fabri choking [4] in 1958 and the compound-choking by Bernstein et al. [5] in 1967.

While using an ejector as a compressor for various applications can be beneficial regarding its low-grade energy source, its performances in a refrigeration cycle, characterized by the Coefficient Of Performance (COP), can not yet compete with the typical devices used nowadays [6].

1.2 Ejector theory

1.2.1 Concept

The design of a typical supersonic ejector is illustrated in Figure 1.2. The primary flow, initially at a high reservoir pressure, passes through a converging-diverging nozzle. As the primary flow reaches the nozzle throat, it achieves sonic conditions and becomes choked. Exiting the nozzle, the flow is supersonic, with very low static pressure. This high-velocity primary flow entrains the secondary flow, which initially has a low reservoir pressure, through turbulent entrainment due to shear stresses between both streams. Both flows then mix in the constant-area mixing duct, where they exchange momentum and exergy. The mixed flow undergoes a series of normal and oblique shocks to recover static pressure. Finally, the divergent section expands the flow to further increase its static pressure and match the downstream conditions.

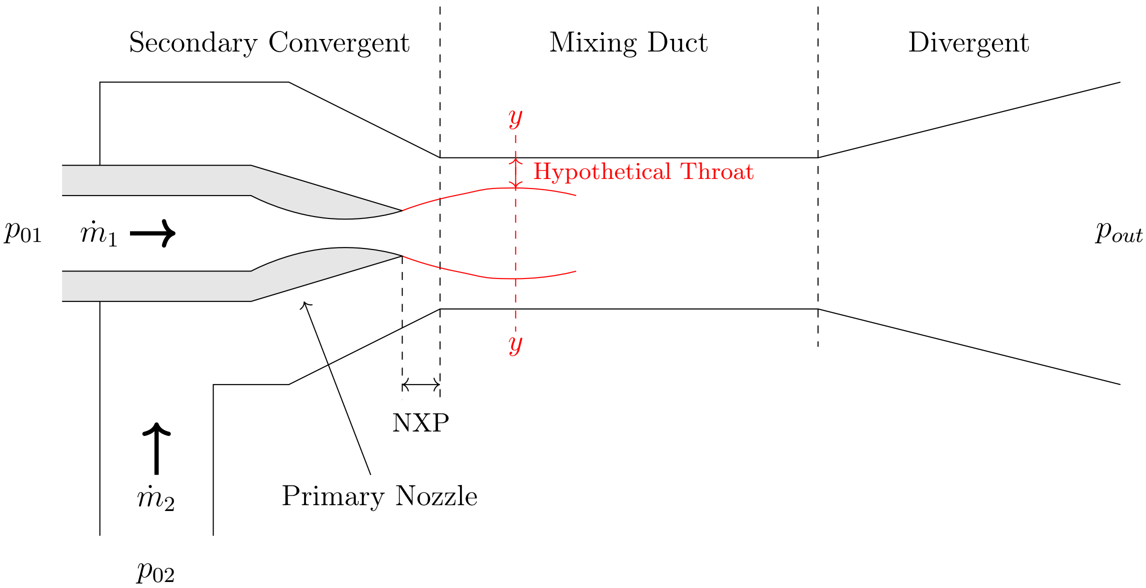

Figure 1.2: Schematic representation of a supersonic ejector. An illustration of the Fabri-choking theory is overlaid in red.

There are two types of ejector configurations, depending on the position of the primary nozzle exit. If the exit is located within the constant-area section of the ejector, it is referred to as a "constant-area mixing ejector". Indeed, with this design, the mixing of both flows occurs in the constant-area section. On the other hand, if the primary nozzle exit is located upstream of the constant-area section, within the convergent section of the secondary flow, the ejector is referred to as a "constant-pressure mixing ejector". The latter will be considered in this work, since it is the design which is said to have the best performances (Keenan et al. [3]).

The reservoir (or total) pressure of the primary and secondary flows are denoted as p_{01} and p_{02}, respectively. p_{out} represents the static pressure at the ejector outlet, or back-pressure. Although p_{out} is often the pressure prescribed in numerical simulations or experimental analysis, it is worth noting that since the flow Mach number at the outlet is very small, the total and static pressures can be considered approximately equivalent at this state: $p_{out} \approx p_{0,out}$.

The key parameter to describe the ejector performance is the entrainment ratio $ER = \frac{\dot{m}_2}{\dot{m}_1}$. Indeed, the purpose of the supersonic ejector is to drive a maximum of secondary flow for the least amount of primary flow. According to the prescribed back-pressure, $p_{0,out}$, which is made dimensionless by dividing it by p_{02}, there are three modes of operation. These modes originate from the choking phenomenon and they significantly impact the ejector performance, as presented on Figure 1.3. This representation is known as the characteristic curve of the ejector.

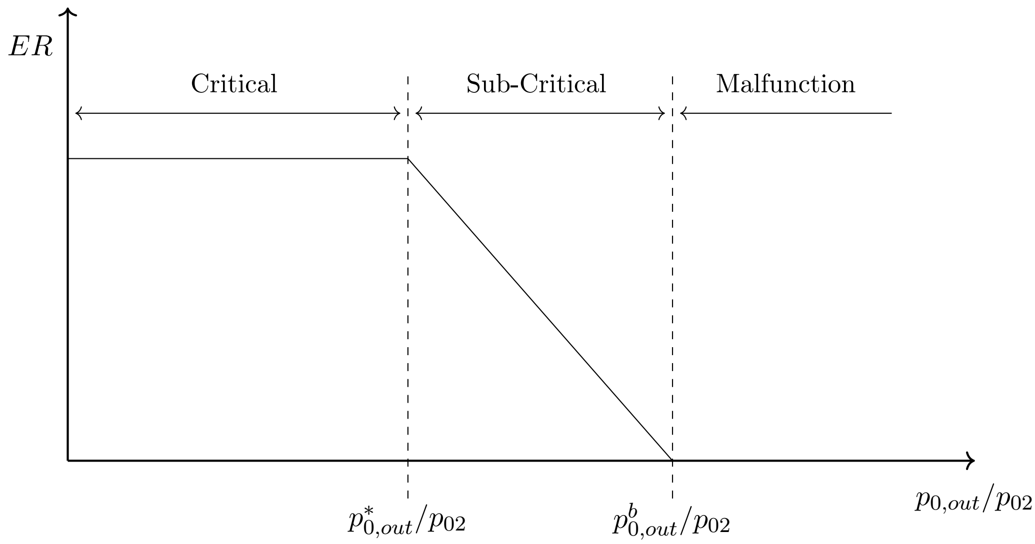

Figure 1.3: Typical characteristic curve of an ejector.

When a flow is choked, it is independent of downstream conditions. The primary flow being accelerated through a classical convergent-divergent nozzle, it will reach sonic conditions near the throat. Consequently, $\dot{m}_1$ will always be choked, independently of the downstream conditions. Given a fixed throat area, $\dot{m}_1$ will only depend on the reservoir conditions. Therefore, the operational mode of the ejector will depend on the behavior of the secondary flow. For a fixed p_{02} :

- If $p_{0,out}$ is smaller than the critical back-pressure $p^*_{0,out}$, the secondary flow will also be choked. This mode is referred to as "critical", "double-choking" or "on-design". If both flows are choked, the entrainment ratio will be independent of downstream conditions. ER will stay constant at its maximum value as long as $p_{0,out} < p^*_{0,out}$.
- If $p_{0,out}$ is greater than the critical back-pressure $p^*_{0,out}$, but smaller than the break-down back-pressure $p^b_{0,out}$, the secondary flow will not be choked. This mode is referred to as "sub-critical" , "single-choking" or "off-design". In this case, the entrainment ratio will decrease linearly as $p_{0,out}$ increases.
- If $p_{0,out}$ is greater than the break-down back-pressure $p^b_{0,out}$, $\dot{m}_2$ will be negative. This means that the secondary flow will be reversed, leading to the malfunction of the ejector.

1.2.2 Choking of the secondary flow

The choking of the secondary flow is important for the performance of an ejector. It is therefore crucial to better understand this phenomenon. There are two principal theories to explain it : the Fabri-choking theory, and the compound-choking theory.

Fabri-choking theory

This theory, initially formulated by Fabri and Siestrunck [4], assumes that the secondary flow is choked by reaching sonic conditions at a virtual throat created between the primary flow and the ejector wall. The primary flow would indeed fans out without mixing with the entrained flow after the primary nozzle exhaust, which would therefore create a converging duct for the secondary flow. The latter would then reach sonic condition at a hypothetical throat located at a certain section y-y of the mixing duct. (Munday and Bagster [7]). This is illustrated in red on Figure 1.2.

The main hypothesis of this theory are the following [4, 8, 9] :

- The flow is steady and one-dimensional.
- The kinetic energy at the primary and secondary flow inlets, as well as at the outlet, can be neglected, meaning that total and static pressures are assumed to be roughly equal at those places.
- Constant pressure mixing occurs inside a constant area section.
- The isentropic relations can be used as an approximation, with coefficients taking the non-ideal processes into account to be determined experimentally.
- The primary flow fans out without mixing with the entrained flow until reaching a certain cross section y-y inside the constant-area section (hypothetical throat). At this point, they begin to mix with uniform pressure, and the secondary flow becomes choked.
- The inner walls are adiabatic.

Compound-choking theory

This theory was introduced by Bernstein et al. [5] and is illustrated on Figure 1.4. Unlike the Fabri-choking theory, the compound-choking theory takes both streams under consideration to analyze the choking phenomenon, as their combination may behave like a sonic stream. Bernstein et al. [5] studied the behaviour of a one dimensional compound flow composed of n streams, with the following assumptions:

- The flow in each stream is one-dimensional, steady and isentropic.
- The static pressure cannot change from stream-to-stream across the nozzle, but only along the nozzle.
- Each fluid is a perfect gas with constant thermodynamic properties.

In this theory, β, the compound-flow indicator, determines the nature of the flow. The flow is compound-subsonic if $\beta < 0$ and compound-supersonic if $\beta > 0$. The flow is choked only if the flow becomes compound-sonic ($\beta = 0$) at a certain section. Bernstein et al. [5] demonstrated that the compound-choking of the flow can only occur at the throat of the nozzle. When the flow is choked, the individual stream Mach numbers are not necessarily equal to 1.

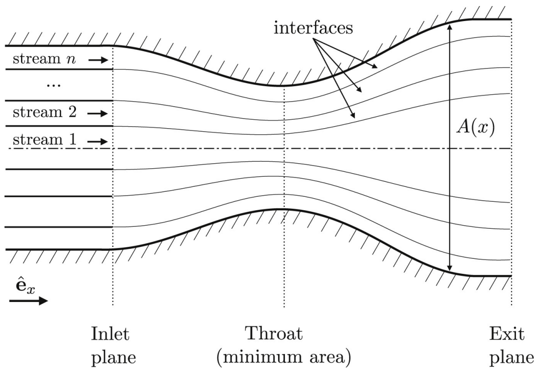

Figure 1.4: Schematic drawing of the compound-compressible nozzle flow. [10]

$$\beta(x) = \sum_{i=1}^{n} \frac{A_i(x)}{\gamma} \left(\frac{1}{M_i^2(x)} - 1 \right) \tag{1.1}$$

Hedges and Hill [11] defined an equivalent Mach number M_{eq} which is the compound flow analog to the Mach number in singe-stream flows. For a compound-subsonic flow, M_{eq} is smaller than 1, while for a compound-supersonic flow, M_{eq} is greater than 1. The flow is then choked when M_{eq} is equal to 1, which also corresponds to $\beta = 0$.

$$M_{eq}(x) = \left(\gamma \frac{\beta(x)}{A(x)} + 1 \right)^{-1/2} \tag{1.2}$$

1.2.3 Simplified models

Simple models to predict ejector performance are based on one-dimensional (1-D) fluid dynamics. The use of 1-D models offers significant advantages in terms of computational efficiency compared to more complex models or Computational Fluid Dynamics (CFD). Additionally, they can predict and cover a wide range of operating conditions for the ejector [9].

The first investigation of an ejector performance was made by Keenan and Neumann in 1942 [12]. Their model was latter refined by Keenan et al. in 1950 [3], assuming a constant-pressure mixing of the two streams from the primary nozzle exit to the constant-area section. They showed that constant-pressure mixing offers better performances than constant-area mixing.

To explain the choking of the secondary flow, Fabri and Siestrunck [4] first developed their theory, latter referred to as Fabri-choking, in 1958. This theory was then used in most research concerning supersonic ejectors. Later, in 1977, Munday and Bagster [7] postulated the presence of an hypothetical throat formed by the primary flow, where the secondary stream reaches sonic velocity and is then effectively choked. The mixing of both flows would then start only after this throat. The following studies all relied on the Fabri-choking theory, assuming constant-pressure mixing occurring inside the constant-area section.

Huang et al. [8] performed in 1999 the 1-D analysis of a constant-pressure ejector performance at the critical mode. Their model was semi-empirical, since some losses coefficients must be determined experimentally. They also stated that the critical back-pressure was an independent parameter which must be obtained from experimental data. Later, Zhu et al. [13] took the non-uniformity of the velocity into account by introducing a shock circle. However, they still assumed the pressure to be uniform in the radial direction. More recently, Chen et al. [9] performed a 1-D performance analysis at the critical and sub-critical regimes. For the latter regime, they assumed that there was also an effective area where the velocity of the secondary stream is the highest. Unlike Huang et al. [8], they stated that the critical back-pressure was not an independent parameter, but is actually an output variable, the entrainment ratio being calculated from an experimental induced flow cross-sectional area A_2.

Another theory for the choking of the secondary flow, the compound-choking theory, arose in 1967 by Bernstein et al. [5], introducing a compound-flow indicator β. Later in 1974, Hedges and Hill [11] defined an equivalent Mach number M_{eq} for the compound flow. This theory wasn't exploited much compared to the Fabri-choking theory. However, more recently, Lamberts et al. [10] showed that this compound-choking theory generally performed better to predict the on-design entrainment ratio of supersonic ejectors. In 2022, Metsue et al. [14] investigated the effect of non-isentropic nozzles. This led to a new definition of the compound-flow indicator β, by defining polytropic efficiencies for each stream.

While the use of 1-D thermodynamic models allows for fast and relatively good predictions of the ejector phenomena, their performance is poorer compared to the predictions CFD can provide. The motivation behind the use of computers lies in resolving smaller scales as well as providing field quantities over the whole ejector setup, improving the understanding of this device.

1.2.4 CFD in supersonic ejector performance analysis

As mentioned earlier, the use of CFD found its motivation in obtaining better results and having predictions and models that are closer to what is observed in practice during experiments.

CFD methods including turbulence are of mainly three types: Direct Numerical Simulation (DNS), Large Eddy Simulation (LES) and Reynolds-Averaged Navier-Stokes (RANS). While the DNS method is by far the most complete one, as it resolves all turbulence length scales, it is also the most expensive, its number of operations being proportional to the cubic power of the Reynolds number, Re^3. Since ejectors are used in supersonic conditions, DNS becomes too expensive compared to other simpler methods. An easy way to reduce the number of operations is by modelling the smaller scales, while resolving the larger ones. This method is called LES and offers relatively good results, though it still requires great computational resources. The last one, RANS, is by far the most commonly used nowadays. While being implemented in most of the commercial softwares, it allows scientists to obtain great results in many applications. The use of the RANS method requires to choose a turbulence closure scheme. Although lots of turbulence models exist, two of them stand out, the $k-\epsilon$ and $k-\omega$. These are the most recognised and used closure schemes in applications working with RANS methods [15, 16].

The first use of CFD goes back to the mid 1990's, where Riffat et al. [17] worked with a commercial CFD software package to evaluate the performance of ejectors in refrigeration systems. Although most of the studies focused on axisymmetric ejectors, hence 2-D analysis, their ejector geometry showed asymmetrical parts, requiring them to perform 3-D analysis. Taking into account that velocities reach high values in an ejector, they decided to use a standard $k-\epsilon$ model to include turbulence effects. However, the geometry being complicated, they were forced to make assumptions regarding the fluid, such as incompressibility and no phase change. Nevertheless, their work showed interesting results regarding the nozzle geometry and position, matching the observations of Keenan et al. [3] four decades prior, stating that constant-pressure mixing ejector performs better than constant-area mixing ejectors.

Later in 2006, Sriveerakul et al. [18] showed that CFD could efficiently predict the entrainment ratio and the ejector critical back-pressure on critical operation mode, reaching a maximum error of 13% compared to experimental values. However, it failed to predict the off-design mode, as discrepancies of 40 to 50% were observed [1].

Three years later, Hemidi et al. [1] performed CFD analysis using a slightly different approach regarding the variable density flows, where they used Favre-Averaged quantities in their equations, giving a Favre-Averaged Navier-Stokes (FANS) method, instead of RANS. They came up with better results than what was found in literature, especially for the off-design operation. Even though the $k-\epsilon$ turbulence model performed well, it was adviced that the $k-\omega$ model, among others, should be considered for further studies regarding off-design operation analysis. Finally, part of their studies focused on double-phase flows, for which they observed that water droplets would not decrease the ejector performance, as said in the literature back then, but could actually improve the off-design regime.

Two years ago, in 2022, Croquer et al. [19] were able to do LES on a geometry based of a rectangular cross-section ejector, designed by Lamberts [10] a few years before. They focused their study on the flow topology in the mixing chamber, obtaining results on shock trains, turbulent structures and compound-choking. As one could guess, the LES analysis offered better results in terms of ejector predictions and understanding its phenomena than the RANS method could provide in the past.

One could also mention other uses of CFD that helped at understanding the ejector phenomena, such as the work of Lamberts [10] on the compound-choking theory, or from Bozkir [20] regarding the geometric properties of the ejector (different convergent-divergent nozzle angles, NXP value, mixing chamber length, etc).

As exposed in the present section, the CFD methods became a must when it comes to analysing aero/thermodynamic quantities, especially regarding supersonic ejectors. With the ever-evolving technologies related to the availability of computational resources, more and more studies will appear using LES method or even DNS someday, enabling predictions that may very closely match the experimental observations.

1.3 Objectives & Structure

This Master's thesis examines the experimental performances of an axisymmetric supersonic ejector, contributing to the ongoing PhD thesis of Romain Debroeyer, which focuses on the numerical and experimental characterization of a cylindrical supersonic air ejector. He will present findings from his thesis at the 1st European Fluid Dynamics Conference (EFDC1) in Aachen, Germany, from September 16th to 20th, 2024. This work is part of a broader research initiative at UCLouvain that has been exploring supersonic ejectors for several years. Previously, Olivier Lamberts investigated a supersonic ejector with a rectangular geometry in his PhD thesis [21]. Further foundational work was done by Nicolas Baguet and Guillaume Querinjean in their Master's thesis [22], where they designed and conducted most of the manufacturing of the new axisymmetric ejector. They also performed extensive numerical investigations to characterize the flow within the ejector. This Master's thesis builds directly on their research.

The main objectives of this Master's thesis are twofold :

1. To ensure the swift and successful assembly of the entire experimental setup by the CREDEM technicians, and to make it fully operational.

2. To conduct a comprehensive testing campaign by taking reliable measurements under various inlet and outlet conditions, and to compare these results with 2D RANS simulations on a numerical setup developed by G. Querinjean and N. Baguet [22].

1.3.1 Finalizing the experimental setup

By the beginning of the academic year, the design and most of the manufacturing of the components for the ejector assembly had been completed. This foundational work was conducted by Guillaume Querinjean and Nicolas Baguet as part of their Master's thesis [22] in 2022-2023. However, finalizing the setup took much longer than anticipated. Despite having the main components already machined or purchased, several tasks remained. Firstly, additional flanges needed to be machined. Following this, all components, both industrial and custom-machined, had to be assembled through welding, bolting, and other methods. The support structure for the ejector assembly also required modifications to fit the setup. Consequently, the entire first semester was dedicated to assembling these parts, and it took about a month into the second semester to position everything correctly on the support.

During this period, significant attention was given to the acquisition system. This involved selecting and calibrating the most suitable sensors for each measurement location. An acquisition program (LabView) was also developed to collect and store data from the various sensors and to control the setup. This program was not made from scratch, as it was adapted from an existing one used for the previous rectangular ejector, which was the focus of the PhD thesis conducted by Olivier Lamberts [21].

Once the installation was fully assembled and the acquisition system was operational, initial tests were conducted. However, the results were unsatisfactory as the experimentally obtained entrainment ratio was significantly lower than expected. This led to an extensive investigation into potential issues, such as leaks, sensors malfunction, and assembly errors. Leaks were identified in several parts of the installation, including flanges and valves, and were subsequently sealed. Despite this, the problem persisted. Additional measures were taken, such as installing an orifice plate for outlet mass flow rate measurement and adding extra sensors. Ultimately, the issue was traced back to an incorrect assembly of the orifice plates. Once this was rectified, the setup was completed, although it was already the beginning of May by this time.

1.3.2 Obtaining reliable results and comparison

The second objective of this Master's thesis was achieved despite the limited time remaining. Progress on this objective had already begun even before the installation was fully operational and reliable.

The first step was to ensure the reliability of future results by understanding how to evaluate the uncertainty on measurements. This required studying the Guide to the Expression of Uncertainty in Measurement (GUM) [23], a key reference for uncertainty evaluation. Gaining a thorough understanding of how to combine uncertainties from sensors and independent measurements allowed for the application of this theory to the specific case under consideration. Additionally, it was essential to accurately evaluate the mass flow rate from the pressure and temperature measurements around the orifice plates. This required studying and adhering to the method outlined in the ISO 5167 standard for orifice plates [24, 25].

Although the initial tests did not yield correct results, they were still useful to develop the post-processing code. Written in *Python*, this code processed the raw data exported by LabView, returning all exploitable values, uncertainties, and graphs. The code implemented the methods for mass flow rate computation and uncertainty evaluation, among other things.

Once consistent results were obtained, the experimental campaign commenced. Over approximately one month, the vast majority of the planned tests were successfully conducted. Each test was performed up to five times to evaluate uncertainty from independent measurements, as it will be detailed in chapter 3 and chapter 4.

The post-processed data from the experimental campaign were then analyzed and discussed. Key results included characteristic curves and wall static pressure profiles for various operating conditions. These were compared with 2D RANS simulations using the numerical setup developed by N. Baguet and G. Querinjean [22] under test conditions, as well as with 1D models. While some discrepancies were observed, further investigation was conducted to explain them, leading to several interesting conclusions.

1.3.3 Structure

The structure of the manuscript is exposed here. It is composed of three main chapters, excluding the introduction and the conclusion.

Chapter 2: Experimental setup

This chapter is dedicated to the presentation of the experimental setup. It covers the key elements of the installation, explaining their purposes within the setup. Since the initial design has evolved compared to the one developed by G. Querinjean and N. Baguet, the changes and the reasons for them are discussed. Following this, all information related to the sensors and the acquisition system is detailed. Finally, the main information about the installation operation is explained.

Chapter 3: Evaluation of the uncertainty of measurements

The chapter 3 aims to present the method for computing uncertainties. It begins with an overview of general theoretical concepts, as outlined in the Guide to the Expression of Uncertainty in Measurement (GUM) [23]. The theory is then applied to the current case, eventually leading to the determination of the uncertainties for the entrainment ratio and the pressure along the wall. This chapter also includes the method to determine the mass flow rates and their uncertainties, following the ISO 5167 standard [24, 25]

Chapter 4: Experimental results and comparison with RANS simulations

As its title suggests, this chapter will present all the results obtained experimentally, along with quantitative and qualitative analyses comparing them to the corresponding RANS simulations. First, the experimental campaign and the test procedure are described. Following that, theoretical material regarding 1-D models is provided. The CFD setup is then shortly explained. Finally, the results are presented, and explanations for the observed differences with the RANS simulations are given. The main results presented are the characteristic curves and the wall static pressure profiles.

Chapter 2

Experimental setup

This section presents the final ejector setup, following the design detailed in the Master's thesis of Nicolas Baguet and Guillaume Querinjean [22]. It begins by revisiting the current mechanical design and explaining the changes made to it. Then, an overview of the P&ID and acquisition system is provided. Finally, an explanation on how to operate the installation is given.

2.1 Mechanical Design

The mechanical design of the ejector has evolved from its original concept to its current implementation. First of all, the fundamental elements of the design outlined by N. Baguet and G. Querinjean [22] are revisited. Subsequently, the required alterations and their justifications are presented.

2.1.1 Pre-existing design

The overall design of the ejector was part of the work done in the Master's thesis of N. Baguet and G. Querinjean [22]. All the pieces constituting the ejector were manufactured already, except for a few gaskets and flanges that required additional work due to particularities such as their shape and geometry. General dimensions were measured to ensure compliance with the technical drawings. The error with the theoretical dimensions were of the order of a tenth of a millimeter, which seemed acceptable. After adding up all the small errors due to the tolerance of the pieces, the NXP value (Nozzle Exit Position), corresponding to the distance between the exit of the primary nozzle and the start of the mixing duct, was larger by 0.24 [mm] compared to the nominal value from the technical drawings. The NXP is represented on Figure 1.2. This difference was taken into account in further numerical simulations.

The key elements of the installation are exposed hereafter. A picture of the complete installation is shown below on Figure 2.6, where those key elements are highlighted.

Primary circuit

The primary circuit, framed in blue on Figure 2.6, is supplied with air coming from a tank, with its pressure being controlled by a pressure regulator. This regulator allows the primary inlet pressure to reach up to 10 bar. The tank is connected to the primary circuit through a flexible pipe and is filled by a compressor from *Ateliers François* during the operation of the ejector.

The air then flows through the DN80 primary tube and through an orifice plate used for measuring the mass flow rate. The tube is sufficiently long before and after the orifice plate to ensure accurate measurement in accordance with the ISO 5167 norm [25].

The air is then brought to the primary convergent-divergent nozzle, which is inside and attached to a "T-connection", or "plenum". Ensuring the coaxial alignment of the nozzle with the T-connection during mounting was paramount. This alignment is crucial for maintaining an axisymmetric annular region at the secondary flow inlet. This coaxiality is ensured thanks to aligned flanges positioned on both sides of the T-connection and on the primary tube and ejector convergent. A groove was also implemented on the flange welded to the primary tube, facilitating the fitting of the T-connection piece into it. On top of that, a temporary custom-made piece was placed in the nozzle which kept it perfectly coaxial during the mounting and tightening of the flanges. A groove was also placed in the converging part of the ejector shroud to center it with the T-connection. All of these particularities can be seen on Figure 2.1, taken from [22].

The nozzle itself also had to be very precisely manufactured, as the primary flow choking depends highly on the nozzle geometry. This justifies the need of strict tolerances during the machining process.

Subsequently, the flow continues to the mixing duct and leaves through a diffuser.

Secondary circuit

The secondary circuit takes ambient air which is brought to the T-connection by suction provided from the primary flow. The pressure of the secondary flow is managed by a butterfly valve, which almost allows vacuum to be produced when it is fully closed. The secondary inlet pressure is then always equal or lower than the ambient pressure. After going through the valve, the air evolves into a DN200 tube and an orifice plate. Once again, the length of the pipe is sufficient long downstream and upstream of the orifice plate to have a measurement of the mass flow rate respecting the norm. Following that, an elbow pipe is utilized to direct the flow into the "T-connection". This plenum allows the flow to be slow enough to consider the measured static pressure to be nearly equal to the total pressure at the ejector inlet $p_2 \approx p_{02}$. The secondary circuit is framed in green on Figure 2.6.

T-connection

The T-connection, or plenum, is the central piece of the setup, allowing the secondary flow to reach nearly zero velocity, which makes the measured static pressure p_2 really close to the total pressure p_{02}, as explained above. This piece had to be perfectly coaxial with respect to the primary nozzle and the ejector shroud in order to have an axisymmetric annular secondary flow at the inlet of the ejector. To achieve this, the edges of the plenum are embedded into grooves. The groove on the primary pipe side is located in the flange, while the groove on the ejector side is in the shroud of the convergent part of the ejector. The contact with the groove inner surface is made with the T-connection external diameter. The T-connection is an industrial piece bought as is. Therefore, the flanges and ejector shroud had to be machined to adapt to its geometry.

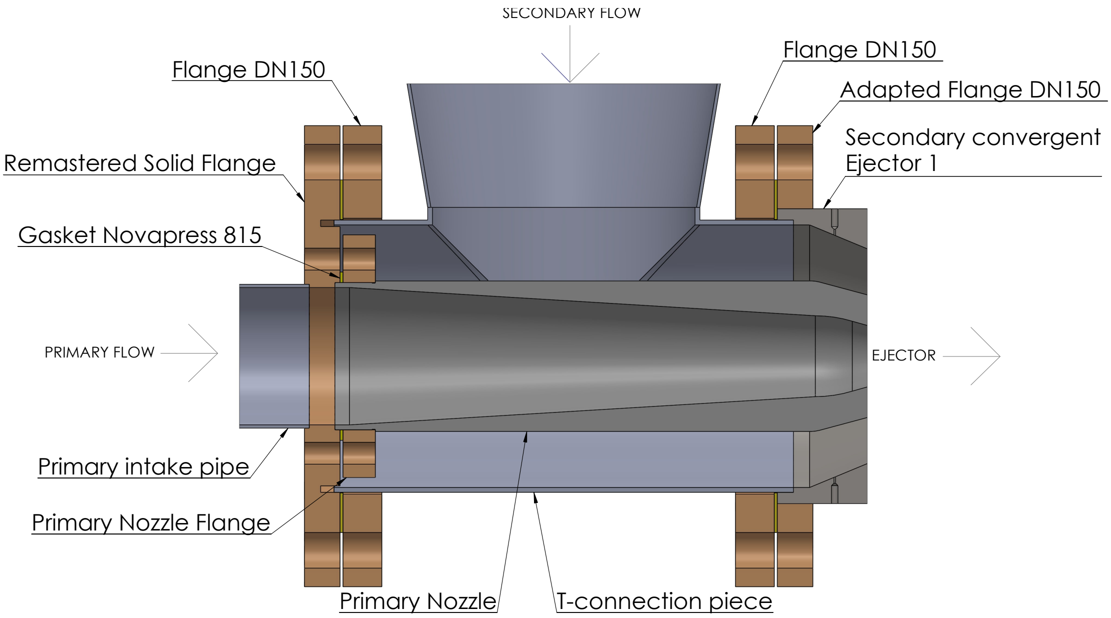

Figure 2.1: Sectional view of the T-connection, from [22].

Ejector shroud

The ejector shroud is the assembly of four physical parts, which must be distinguished from its three functional parts, namely : the converging section, the constant-area mixing duct, and the diverging section. The distinction between physical and functional parts can be more clearly visualized in Figure 2.4. The installed ejector shroud and T-connection are depicted in the picture shown in Figure 2.2. A sectional view of this part is displayed in Figure 2.3, where the primary nozzle can also be seen.

The first part of the ejector shroud, flow-wise (i.e. from left to right), contains the converging section and a small part of the mixing duct. This piece was machined and a groove was made to fit the T-connection. The converging section will accelerate the secondary flow.

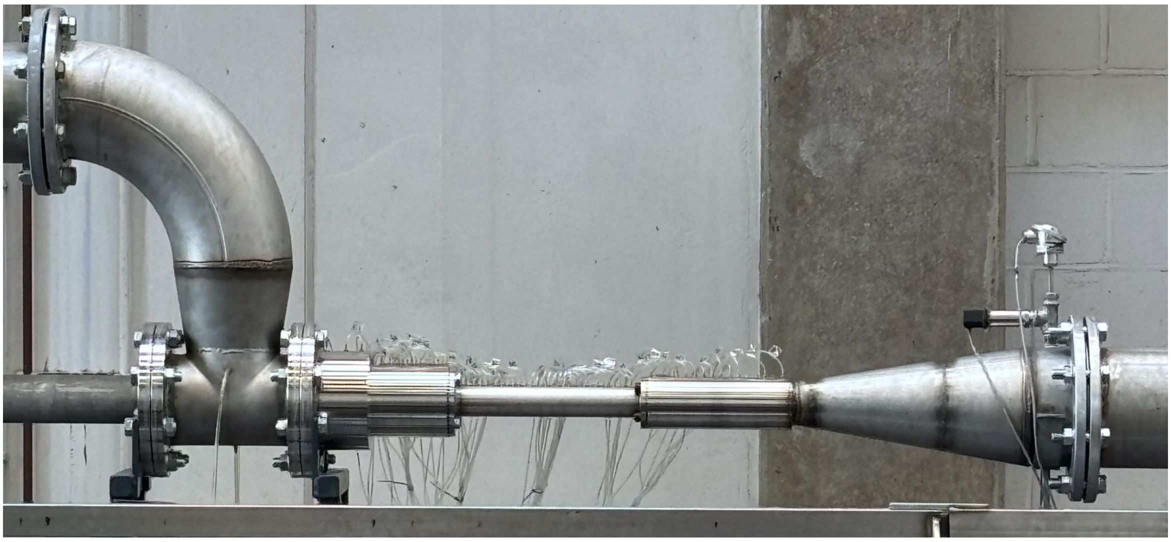

Figure 2.2: Picture of the ejector part of the installation.

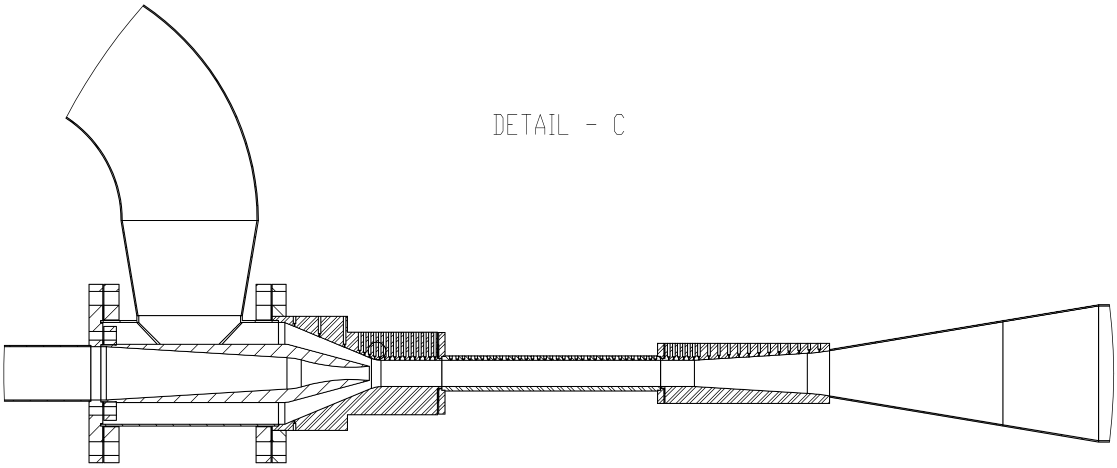

Figure 2.3: Detailed view C of Figure 2.7.

The second part represents the majority of the constant-area mixing duct. It was also machined and assembled to the previous part thanks to welded flanges. The mixing duct is where momentum and exergy is exchanged between both flows, meaning it is the place where they actually mix.

The third part contains once again a small portion of the mixing duct, as well as the beginning of the diverging section. This piece was manufactured to ensure high precision on its angles, a low one of 3.5°, followed by a higher one of 9.5°. The angle increases in order to match the next part of the assembly. It was also assembled with the previous part through welded flanges.

The fourth and last physical part of the ejector shroud is an industrial divergent. It was bought as is, hence the need to adapt the previous piece to match the inclination angle of this part. This piece was directly welded to the previous part. The diverging section, or diffuser, is necessary to expand the mixed flow to match the downstream outlet pressure and slow down the flow.

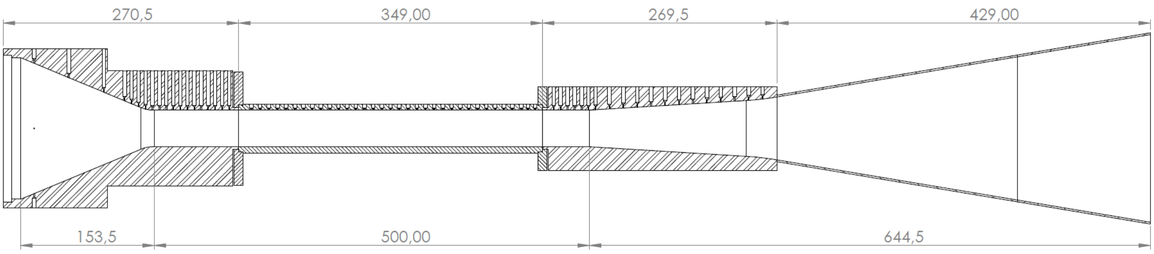

Figure 2.4: Technical drawing of the ejector assembly, from [22]. The length of the physical parts are displayed above, while the length of the functional parts are displayed below. The dimensions are in millimeters.

The first 3 physical parts of the ejector shroud are pierced throughout their length to allow the successive measurement of the static pressure along the wall. There is a total of 75 tapped holes, but 11 will be closed during operation, leaving 64 pressure taps open for measurement. These can be seen on Figure 2.5. More information about this pressure measurement are given later on in this chapter.

As mentioned earlier, the setup is said to be a "constant-pressure mixing ejector", meaning that the primary nozzle exit is located within the secondary flow convergent. The NXP is the length between the primary nozzle exit and the start of the mixing duct. It is a very important quantity, as it determines the ejector's performances.

Outlet

Another butterfly valve is located at the outlet to control the desired outlet pressure. An elbow pipe has been placed downstream of this valve, to redirect the flow towards the ceiling for safety reasons. As it will be explained right after, it was decided to extend the setup to allow the computation of the total mass flow rate. Upstream of the orifice plate, a DN200 pipe is connected to the industrial diverging section through flanges. The downstream pipe is similarly linked to the outlet butterfly valve using flanges. This part of the installation is framed in red on Figure 2.6.

2.1.2 Changes made to the pre-existing design

Some adjustments were made to the design imagined by N. Baguet and G. Querinjean throughout the year. The main change was the addition of an outlet mass flow rate measurement. It was motivated by a desire to validate or invalidate the measurements of the inlet flow rates. Indeed, during the first tests, the entrainment ratio was found to be abnormally low, coming from a too small measured mass flow rate at the secondary inlet. To deduce if there was any leakage that would suck air elsewhere than in the secondary duct, it was decided to also measure the total mass flow rate coming out.

To do so, a new orifice plate had to be placed. According to the ISO 5167 standard [24, 25], there must be a minimum constant section pipe length of 10 times the pipe diameter upstream of the orifice plate, and 5 times downstream. The new DN200 pipe then considerably increased the total length of the installation, also requiring additional supports to hold everything in place.

An additional pressure sensor was also placed. Originally, only a pressure sensor located at the T-connection was planned to measure the secondary flow inlet pressure. However, during the mounting, this sensor was settled upstream of the orifice plate in the secondary stream tube to precisely measure the mass flow rate. Therefore, the originally planned pressure sensor at the T-connection had to be added to have the real secondary pressure at the beginning of the numerical domain. Indeed, some pressure losses occur between those two sensors, the main ones coming from the orifice plate in the secondary pipe. On top of that, a silencer was added at the outlet to reduce the noise emitted when the installation is running.

2.2 P&ID and Acquisition system

This section aims at both presenting the sensors used to collect all the data, and showing the acquisition system, while explaining a few of its particularities. The Piping & Instrumentation Diagram (P&ID) finds its purpose in helping the technicians with the placing of the sensors, as well as providing overall information about the orifice plates to measure the mass flow rates.

2.2.1 P&ID

The P&ID is shown on Figure 2.7 hereunder. It has been designed through the work of N. Baguet and G. Querinjean [22], but some changes were done regarding the notation of the sensors, as well as the dimensions of the orifice plates used for the calculations of the mass flow rates. Furthermore, it was decided to compute the total mass flow rate at the exit of the installation, by following the same ISO regulations as for the primary and secondary circuits, as explained before.

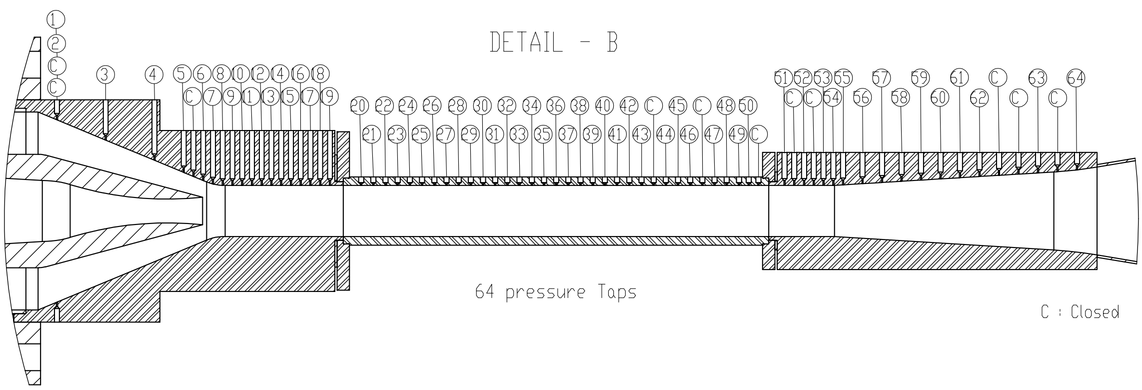

Figure 2.5: Detailed view B of Figure 2.7.

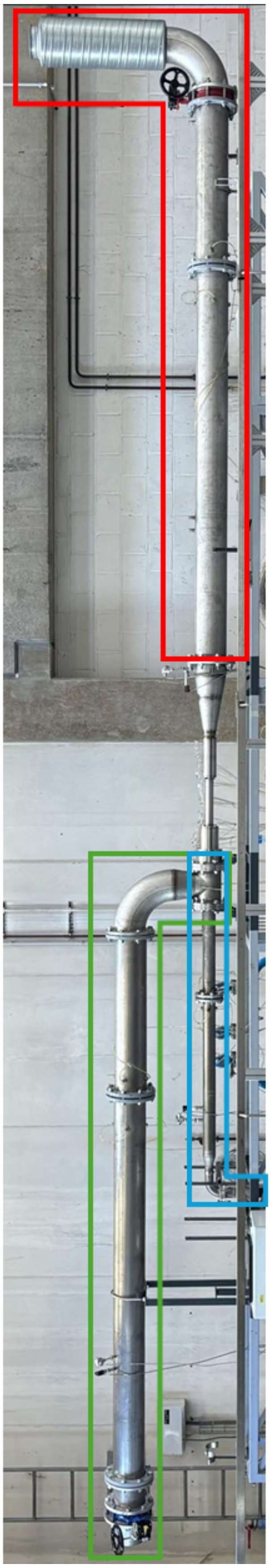

Figure 2.6: Picture of the complete installation.

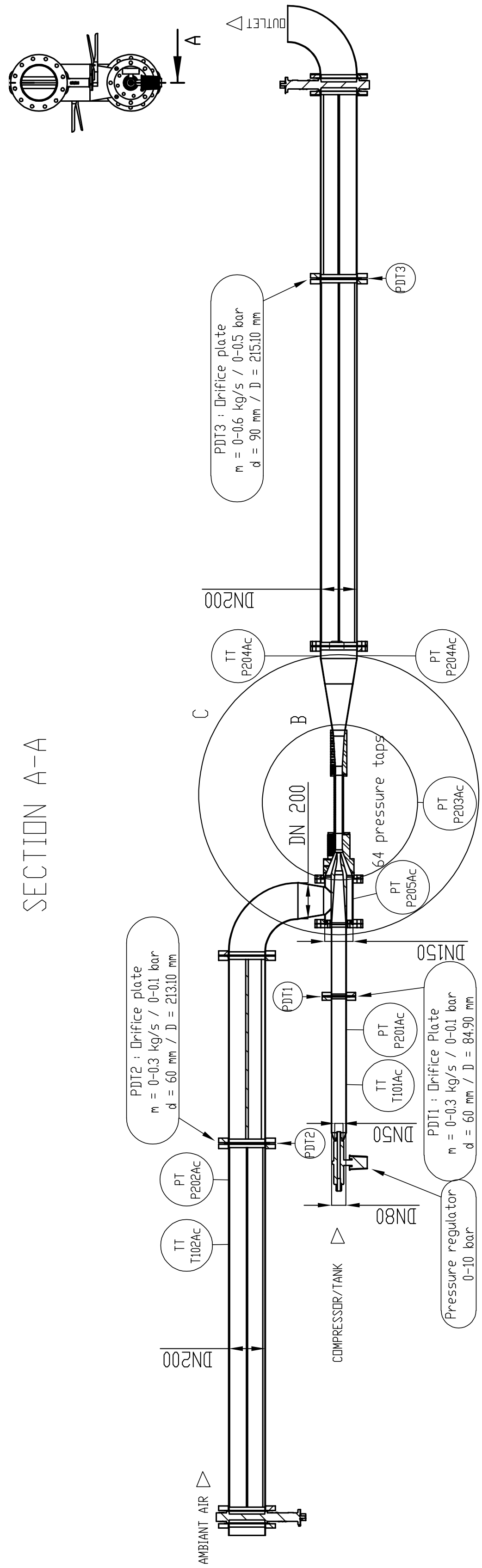

Figure 2.7: P&ID of the ejector setup.

2.2.2 Sensors selection

The positions of the various sensors and their referencing are displayed on Figure 2.7. To accurately measure pressures and temperatures within the desired ranges, selecting the appropriate sensors was essential.

For the primary circuit, the pressure sensor *P201Ac* has two purposes. It is necessary to know exactly the primary pressure delivered by the compressor, and it is needed in the computation of the primary mass flow rate. As the primary pressure required for the measurements will lie between 3 and 7 [bar], a type RAG relative pressure sensor from Kistler with a pressure range between 0 and 10 [bar] and an accuracy of 0.5% was chosen [26]. Regarding the temperature sensor *T101Ac*, also useful for the mass flow rate determination, a probe Pt100 from Thermibel and ranging from 0 to 100 [°C] has been picked. This type of probe has an accuracy of ± 0.5 [°C] at ambient conditions. Lastly, the differential pressure sensor *PDT1* is needed around the orifice plate to also compute the mass flow rate. For this purpose, a PMD75 sensor from Endress and Hauser [27], allowing for a measurement of a pressure difference of maximum $\pm$ 0.1 [bar], was placed. This sensor has a fine accuracy, reaching 0.05% for the "Platinum" version.

For the secondary circuit, same as for the primary one, the pressure, temperature and differential pressure sensors are required for the mass flow rate computation. Moreover, the pressure sensor *P202Ac* also allows to observe the pressure changes when moving the butterfly valve at the inlet. There, the desired pressure is between 0 and 1.2 [bar], which lead to the choice of an absolute pressure sensor from Endress and Hauser (PMP131 model) [28], with a range going from 0 to 1.6 [bar] and an accuracy of 0.5%. The temperature probe *T202Ac* and the differential pressure sensor *PDT2*, for their part, are the same models as for the primary circuit.

Moving forward, a pressure sensor in the plenum, or T-connection, *P205Ac*, is placed to measure the pressure of the secondary stream at the inlet of the ejector, and therefore at the inlet of the numerical domain. Indeed, the pressure measured by this sensor will be lower than the one measured by *P202Ac*, due to pressure losses, especially the one occurring through the orifice plate. This pressure is also used to make the inlet, outlet, and wall pressures dimensionless and to determine in which regime the ejector is operating, through the ratios p_{01}/p_{02} and $p_{0,out}/p_{02}$. As the pressure measured there is of the same range than upstream in the secondary circuit, *P205Ac* is the same type of pressure sensor as *P202Ac*. Moreover, the pressure there is measured on three different spots around the T-connection to take into account the fact that the secondary stream comes from the top, and goes around the primary circuit, which may cause the pressure to not be uniform everywhere in the plenum.

Then, one single sensor is required to measure the pressure along the ejector wall. This measurement is realized through 64 pressure taps, which are represented on Figure 2.5. There are actually 75 tapped holes in the ejector shroud, but some of them are closed (denoted 'C' on the figure). The first four tapped holes are actually at the same spot axially, but positioned around the ejector shroud, separated by 90°. At this place, the flow may indeed not be fully axisymmetric yet due to the way the secondary stream enters into the plenum upstream. The pressure taps can be moved between the holes if one desires to change the position of the measurements. The 64 electronic valves (8x8 sets) allow to switch between the various pressure taps of the ejector. The pressure measurement is retrieved through 2 acquisition cards (2x32). There is thus a single pressure transducer, denoted *P203Ac*, for the whole 64 ports. The expected pressure, based on simulations, lies between 0.4 and 2.5 [bar]. Therefore, the chosen sensor is an absolute pressure sensor, ranging from 0 to 10 [bar], coming from Druck as the PTX1400 model [29]. This sensor is more precise than the others, with a maximum accuracy of 0.25%.

Finally, the outlet pressure set by the butterfly valve is observed through the absolute pressure sensor *P204Ac* from Endress and Hauser as well (PMP21 model) [30], with a 0 to 10 [bar] range and an accuracy of 0.3%, as the desired pressure there is between 0.8 and 2.4 [bar]. The temperature probe *T104Ac* is useful to change the boundary conditions of the simulations. The probe was chosen based on the ones available in the CREDEM reserve, with a measuring rod long enough to reach the center of the pipe. The probe is thus a Couple K model from Thermibel, ranging from 0 to 650 [°C]. Further, these two sensors, combined with another differential pressure sensor (also PMD75), *PDT3*, allowing for a delta of ± 0.5 [bar], are used to compute the total mass flow rate.

A summary of the names of the various sensors, along with their locations in the installation, measuring ranges, and accuracy, is presented in Table 2.1.

Location	Name	Range	Accuracy
Primary inlet	*P201Ac*	0-10 [bar]	0.5%
	T101Ac	0-100 [°C]	0.5 [°C]
	PDT1	±0.1 [bar]	0.05%
Secondary inlet	*P202Ac*	0-1.6 [bar]	0.5%
	T102Ac	0-100 [°C]	0.5 [°C]
	PDT2	±0.1 [bar]	0.05%
Plenum	*P205Ac*	0-1.6 [bar]	0.5%
Ejector wall	*P203Ac*	0-10 [bar]	0.25%
Outlet	*P204Ac*	0-10 [bar]	0.3%
	T104Ac	0-650 [°C]	0.5 [°C]
	PDT3	±0.5 [bar]	0.05%

Table 2.1: Summary of the location, range and accuracy of the selected sensors.

2.2.3 Orifice plates selection

As already explained above, the mass flow rate determination requires the measure of a differential pressure through an orifice plate. For each differential pressure measurement, an appropriate orifice plate must therefore be chosen. According to the ISO 5167 standard [25], the limits of use of orifice plates with differential pressure measured using tappings placed at a distance of D upstream and $D/2$ downstream of the orifice place (D and $D/2$ pressure tappings) are :

$$\begin{cases} d \geq 12.5\ [mm]; \\ 50\ [mm] \leq D \leq 1000\ [mm]; \\ 0.1 \leq \xi \leq 0.75; \\ Re_D \geq 5000 \text{ for } 0.1 \leq \xi \leq 0.56; \\ Re_D \geq 16000\xi^2 \text{ for } \xi \geq 0.56. \end{cases}$$

where d is the orifice diameter, D is the pipe diameter, ξ is the ratio between the two, $\frac{d}{D}$, and Re_D is the Reynolds number. On top of that, the selection of the orifice diameter d was made in order to have a differential pressure with a good order of magnitude. Indeed, an orifice which is too narrow would lead to a too large Δp, which may be above the sensor's measuring range. On the other hand, a too large orifice would lead to a too small Δp, increasing the sensitivity of the measurement, and thus the uncertainty on the measured mass flow rate. The orifice diameters were thus chosen among the available orifice plates to have a Δp of a few thousands of [Pa] for each one. This led to a diameter $d = 60$ [mm] for both the primary and secondary inlet orifice plates, resulting in a ratio of $\xi \approx 0.71$ and $\xi \approx 0.28$, respectively. For the orifice plate measuring the total mass flow rate, a diameter of $d = 90$ [mm] was chosen, since the flow rate will necessarily be greater. This leads to a ratio $\xi \approx 0.42$.

2.2.4 Sensors Calibration

After choosing the right sensors, a calibration process had to be done to ensure that future measurements would be correct. The calibration was done for all the pressure sensors. For the differential pressure ones, *PDT1*, *PDT2* and *PDT3*, an air calibration unit was used by adding several disks representing a known pressure, which led to the linear relationship between the voltage and the physical quantity. For the other pressure sensors, an oil calibration unit was utilized with other disks. After obtaining the coefficients of the linear relationships, these were incorporated in the acquisition system. Further details on the calibration points of the sensors and their associated linear curve can be found in section B.2 of Appendix B.

All of the sensors are listed in an Excel sheet, referred to as the "DAQ" (Data Acquisition, see section B.1), with their range, positioning, reference, as well as the corresponding coefficients of the linear relationships. The DAQ file is then read by the LabView program, which is detailed in the next sub-section, to translate an input voltage into an output physical quantity.

2.2.5 Acquisition system

The data acquisition is realised through the software LabView, installed on a CREDEM computer. Every sensor is connected to the LabView, as well as the pressure regulator, which controls the primary inlet pressure. The different values of pressures, temperatures and mass flow rates at different places on the installation can easily be visualized on the program. Figure 2.8 depicts a screenshot of what the interface looks like while running an experiment.

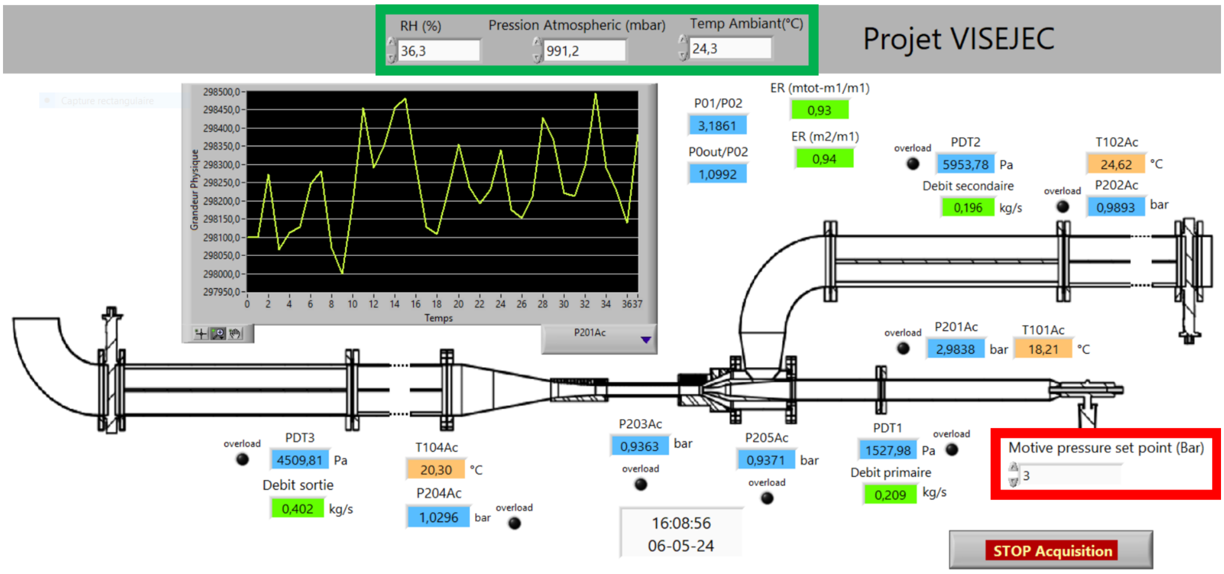

Figure 2.8: LabView interface.

The mass flow rates, as well as their uncertainties, are computed within the program. The calculation process follows the ISO 5167 standard [25] using the differential pressure, static pressure and temperature measurements, provided the geometry of the orifice plate. However, to take into account type A uncertainties using several independent measurements, the mass flow rate computation is done again using a *python* code during the post-process. The detailed calculation will be explained in chapter 3.

It is worth noting that the LabView used for this experiment was adapted from a pre-existing LabView conceived for the previous project VISEJEC conducted by Olivier Lamberts [21].

The values of the different quantities of interest are registered each second in a text file. The latter is then post-processed to get clear results, which will be presented in chapter 4.

2.3 Operation

A user manual has been written as part of a risk analysis regarding the installation. The main guidelines are about starting up the compressor, plugging in the cables to the computer, and then launching the LabView software, from which all the necessary information are displayed. The whole manual can be found in Appendix A. However, the key control and response variables can be briefly exposed here.

2.3.1 Control variables

The main control parameter is the primary inlet pressure, which is defined by setting the motive pressure in LabView (framed in red on Figure 2.8). A pressure regulator will then allow to set the desired pressure at the primary inlet. The pressure at the secondary inlet and at the outlet are controlled through butterfly valves present on the installation.

The ambient conditions, i.e. temperature, pressure and relative humidity, also have to be set by the user before running the experiment (framed in green on Figure 2.8). Setting the right atmospheric pressure is important for a pressure measurement with a relative pressure sensor. Indeed, the physical quantity retrieved from the sensor measurement must be added to the atmospheric ambient pressure to get the absolute pressure. These ambient conditions are retrieved from precise sensors located in the room where the ejector is installed.

The acquisition of the pressure measurements along the mixing duct can also be controlled through LabView. The 64 pressure points are all connected to the same sensor through a pressure scanner, in which resides 64 valves that can be opened or closed at will. The method to acquire those data can be either manual or automatic. With the former mode, represented on Figure 2.9a, one can choose to open or close any of the 64 valves manually, allowing the measurement of any of the 64 pressure points. On the other hand, with the automatic mode represented on Figure 2.9b, each of the valves is successively switched on, while all the others remain closed. The time during which each valve remains open can be set by the user. During the experiments, this time interval was set to 15 seconds.

2.3.2 Response variables

The LabView interface displays every static temperature, static pressure, and differential pressure measurements. The ratios of primary inlet total pressure and outlet total pressure to secondary inlet total pressure, p_{01}/p_{02} and $p_{0,out}/p_{02}$, are also shown to help in achieving the desired ratios through valve tuning.

The mass flow rates are also displayed. Those are computed directly in LabView following the ISO 5167 standard [25]. Additionally, the entrainment ratio is shown to allow instantaneous assessment of whether the results are consistent. Note that those quantities are re-computed properly in post-processing, taking into account several independent measurements to get both type A and type B uncertainties.

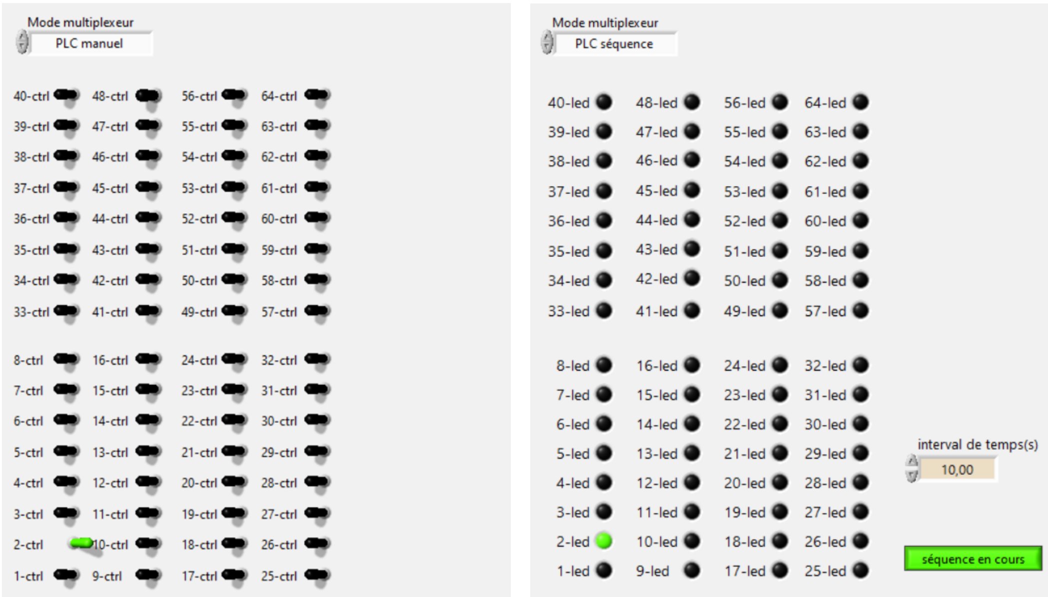

(a) Manual mode (b) Automatic mode

Figure 2.9: LabView interface for the operation of the 64 valves.

The LabView records each variable every second, and saves them in a text file, which is then post-processed to obtain the results discussed in chapter 4. The next chapter will be dedicated to the explanation of the method followed to acquire precisely the values of interests and their uncertainties.

Chapter 3

Evaluation of the uncertainty of measurements

In order to get reliable experimental results, it is important to evaluate the uncertainty of the measurements. This will be achieved by following the method outlined in the Guide to the expression of Uncertainty in Measurement (GUM) [23]. The necessary theoretical concepts from this document, which are crucial for understanding how uncertainties in the reported results are derived, are summarized below. Subsequently, these concepts will be applied to the specific case under consideration.

3.1 Theoretical concepts

The formal definition of the uncertainty of a measurement, as expressed in the GUM [23], is as follows: "the uncertainty (of measurement) is a parameter associated with the result of a measurement that characterizes the dispersion of the values that could reasonably be attributed to the measurand", where the measurand can be defined as a particular quantity subject to measurement.

When considering a specific measured quantity X_i, its estimate is denoted as x_i, and its standard uncertainty is represented by $u(x_i)$. This standard uncertainty can be assessed through two methods: a type A or a type B evaluation of uncertainty.

3.1.1 Type A evaluation of uncertainty

This type of uncertainty evaluation is used if n independent observations of X_i are performed. In this case, the best estimate is the average of the observations.

$$x_i = \overline{X_i} = \frac{1}{n} \sum_{k=1}^{n} X_{i,k} \tag{3.1}$$

The experimental standard deviation of the mean may be used as a measure of the uncertainty on x_i.

$$u(x_i) = s(\overline{X_i}) \tag{3.2}$$

The experimental variance of the mean $s^2(\overline{X_i})$ is the experimental variance of X_i divided by n.

$$s^2(\overline{X_i}) = \frac{s^2(X_i)}{n} = \frac{1}{n}\frac{1}{n-1}\sum_{k=1}^{n}(X_{i,k} - \overline{X_i})^2 \tag{3.3}$$

For this estimation to be correct, the number of independent observations n should be sufficiently large.

3.1.2 Type B evaluation of uncertainty

This evaluation type is used if the estimate x_i is not obtained from repeated observations. The standard uncertainty $u(x_i)$ is thus evaluated by scientific judgement based on available information. Those can be previous measurements, specifications, reference data, etc. The standard uncertainty will be computed differently according to the expression of the prescribed uncertainty. Indeed, the latter could be expressed as a multiple of the standard deviation, as an interval of confidence, or as a certain probability to lie within a given interval.

A common scenario arises when it is specified that X_i has a 100% probability of lying within a given interval $[a_-; a_+]$, which corresponds to a rectangular distribution. This often occurs when the accuracy of a measurement is provided in a sensor datasheet. For a rectangular distribution, the estimate on X_i is the midpoint of the interval, $x_i = (a_- + a_+)/2$, and its associated standard uncertainty is :

$$u^2(x_i) = \frac{(a_+ - a_-)^2}{12} = \frac{a^2}{3} \tag{3.4}$$

where a represents the half distance between the bounds, $a = (a_+ - a_-)/2$.

3.1.3 Combined standard uncertainty

Often, the measurand is not measured directly, but is rather determined from other measured quantities. The relationship between those N measured quantities and the measurand Y is given by a function f :

$$Y = f(X_1, X_2, ..., X_N) \tag{3.5}$$

The estimate y of the measurand is the result of the function f applied to the estimates x_i :

$$y = f(x_1, x_2, ..., x_N) \tag{3.6}$$

The estimated standard deviation of y is called the combined standard uncertainty and is denoted $u_c(y)$. It is determined from the standard uncertainties $u(x_i)$. Following the law of propagation of uncertainty, the combined uncertainty is computed as follows, if the input quantities are independent :

$$u_c^2(y) = \sum_{i=1}^{N}(c_i u(x_i))^2 \tag{3.7}$$

where c_i are the sensitivity coefficients. Those can be determined experimentally, but are typically computed as the partial derivative of f with respect to X_i, evaluated with the estimates of the input quantities :

$$c_i = \frac{\partial f}{\partial x_i} = \left.\frac{\partial f}{\partial X_i}\right|_{x_1, x_2, \ldots, x_N} \tag{3.8}$$

However, if the non-linearity of f is significant, higher-order terms of the Taylor series expansion must be included in the computation of the combined uncertainty.

In the case of correlated input quantities, the combined uncertainty is computed using an estimated covariance $u(x_i, x_j)$ between the measured quantities :

$$\begin{aligned} u_c^2(y) &= \sum_{i=1}^{N} \sum_{j=1}^{N} \frac{\partial f}{\partial x_i} \frac{\partial f}{\partial x_j} u(x_i, x_j) && \text{(3.9)a} \\ &= \sum_{i=1}^{N} (c_i u(x_i))^2 + 2 \sum_{i=1}^{N-1} \sum_{j=i+1}^{N} c_i c_j u(x_i, x_j) && \text{(3.9)b} \end{aligned}$$

One can define the correlation coefficient r :

$$r(x_i, x_j) = \frac{u(x_i, x_j)}{u(x_i) u(x_j)} \tag{3.10}$$

This quantity always falls within the range of -1 to +1. It is equal to 0 if X_i and X_j are independent. Equation (3.9)b then becomes :

$$u_c^2(y) = \sum_{i=1}^{N} (c_i u(x_i))^2 + 2 \sum_{i=1}^{N-1} \sum_{j=i+1}^{N} c_i c_j u(x_i) u(x_j) r(x_i, x_j) \tag{3.11}$$

The correlation coefficients can be estimated experimentally. If a change δ_i in x_i leads to a change δ_j in x_j, the correlation coefficient related to x_i and x_j can be approximated as :

$$r(x_i, x_j) \approx \frac{u(x_i) \delta_j}{u(x_j) \delta_i} \tag{3.12}$$

A type A covariance evaluation can be realised if the 2 quantities are observed from n independent pairs of observations made under the same conditions.

$$u(x_i, x_j) = s(\overline{X_i}, \overline{X_j}) = \frac{1}{n(n-1)} \sum_{k=1}^{n} (X_{i,k} - \overline{X_i})(X_{j,k} - \overline{X_j}) \tag{3.13}$$

It is important to note that such correlations cannot be disregarded; however, they can be avoided by introducing additional independent input quantities to account for common influences.

A combined uncertainty can also be the result of both a type A and a type B contribution on the uncertainty. In this case, the total combined uncertainty is found by taking the squared sum of the different contributions :

$$u_c^2(y) = u_A^2(y) + u_B^2(y) \tag{3.14}$$

where $u_A(y)$ and $u_B(y)$ are themselves also combined uncertainties, but one coming from a type A evaluation, and the other from a type B evaluation of uncertainty. Besides, one has to be careful not to "double-count" uncertainty components. Indeed, a type B uncertainty should be included as an independent component of the total combined uncertainty only if its effect does not contribute to the observed variability. In the latter case, this type B uncertainty would already be included in the type A uncertainty component.

3.1.4 Expanded uncertainty

The expanded uncertainty, denoted U, allows to provide a confidence interval on a measurand. It is obtained by multiplying the standard uncertainty by a coverage factor k_p :

$$U = k_p u(x_i) \tag{3.15}$$

The subscript p is the specified coverage probability or level of confidence (typically 90%, 95% or 99%). When X_i follows a normal distribution, the coverage factor k_p must be determined using a t-distribution :

$$k_p = t_p(\nu_i) \tag{3.16}$$

where ν_i is the number of degrees of freedom of the measured quantity X_i and t_p the t-factor evaluated for a level of confidence p. For a quantity estimated by the average of n independent observations (type A), ν_i is equal to $n-1$. From the level of confidence and the degrees of freedom, the t-factor can be obtain from tables or using *python* libraries. The confidence interval on an estimate x_i is therefore :

$$x_i - U \leq X_i \leq x_i + U \tag{3.17}$$

The expanded uncertainty can also be used to determine a confidence interval on Y, by multiplying the coverage factor by the combined uncertainty :

$$U = k_p u_c(y) \tag{3.18}$$

$$y - U \leq Y \leq y + U \tag{3.19}$$

If the combined uncertainty squared $u_c^2(y)$ is the sum of two or more uncertainty components $u_i^2(y)$, like in Equation (3.14), the coverage factor is determined with a *t-student* law and through an effective number of degrees of freedom ν_{eff} :

$$k_p = t_p(\nu_{eff}) \tag{3.20}$$

This effective number of degrees of freedom can be found with the Welch-Satterthwaite formula [31–33] :

$$\nu_{eff} = \frac{u_c^4(y)}{\sum_{i=1}^{N} \frac{u_i^4(y)}{\nu_i}} \tag{3.21}$$

where ν_i are the degrees of freedom of each of the uncertainty components.

As mentioned earlier, for a type A evaluation on an uncertainty component, ν is the number of independent observations minus one, $\nu_i = n - 1$. Determining the number of degrees of freedom for a type B uncertainty component is a bit more complex. It is evaluated using the fact that ν is a measure of the uncertainty of the variance :

$$\nu_i \approx \frac{1}{2}\frac{u^2(x_i)}{\sigma^2(u(x_i))} \approx \frac{1}{2}\left[\frac{\Delta u(x_i)}{u(x_i)}\right]^{-2} \tag{3.22}$$

with σ being the standard deviation. The quantity in brackets here is subjective and is therefore obtained through scientific judgement based on available information. In other words, it is an expression of how much one judges that the standard uncertainty $u(x_i)$ is reliable. If it is considered to be very certain, $\frac{\Delta u(x_i)}{u(x_i)}$ would tend to 0, and therefore $\nu_i \to \infty$.

3.2 Application on the case at hand

The theory presented above will now be applied to the case at hand. The way to obtain the uncertainty on the entrainment ratio will be investigated first. This requires to know the uncertainty on the mass flow rates and, of course, the value of those quantities, which is not straightforward since it requires to know the value of some case-specific coefficients. The pressure along the wall in the ejector is another a quantity of interest. How to get the uncertainty of its measurement will then also be explained.

It is important to note that the various values that are measured are averaged over time. However, the uncertainty linked to time variation was not included, since it does not represents the variation of independent measurements.

3.2.1 Computation and uncertainty of the entrainment ratio

The main result, or measurand that will be analyzed from the measurements is the entrainment ratio ER :

$$Y = ER = \frac{\dot{m}_2}{\dot{m}_1} = f(\dot{m}_1, \dot{m}_2) \tag{3.23}$$

For some reasons that will be explained further, the entrainment ratio may be computed using rather the difference between the outlet mass flow rate and the primary mass flow rate, instead of using directly the measured secondary mass flow rate :

$$Y = ER = \frac{\dot{m}_{out} - \dot{m}_1}{\dot{m}_1} = f(\dot{m}_1, \dot{m}_{out}) \tag{3.24}$$

To determine the entrainment ratio and its uncertainty, it is therefore necessary to compute estimates of the mass flow rates along with their uncertainties.

Mass flow rate computation

The mass flow rates are themselves measurands computed from direct measurements. Indeed, the measure of the pressure difference through the orifice plate, as well as the measure of the static temperature and pressure before the orifice plate will allow to compute the mass flow rate. According to the ISO 5167 standard [24], a mass flow rate is computed using the following equation :

$$\dot{m} = \frac{C_d}{\sqrt{1-\xi^4}} \epsilon A_t \sqrt{2\rho_a \Delta p} \tag{3.25}$$

assuming that state a is upstream of the orifice plate, and state b is downstream of the orifice plate. ξ is the diameter ratio,

$$\xi = \frac{d}{D} \tag{3.26}$$

where d is the orifice diameter and D is the pipe diameter. C_d is the discharge coefficient, ϵ is the expansibility factor, A_t is the throat cross-section area, Δp is the pressure difference measured through the orifice plate and ρ_a is the fluid density upstream. The throat area is :

$$A_t = \frac{\pi d^2}{4} \tag{3.27}$$

Since the fluid is air approximated as an ideal gas, ρ_a is :

$$\rho_a = \frac{p_a}{R T_a} \tag{3.28}$$

where p_a and T_a are the measured static pressure and temperature, and R is the specific gas constant. The latter can be computed by taking into account the humidity of the air. For humid air, the total R is found by weighting the specific gas constant related to water and dry air, using the absolute humidity x_v :

$$R = \frac{x_v}{x_v+1} \frac{R_u}{M_{m,w}} + \frac{1}{x_v+1} \frac{R_u}{M_{m,da}} \tag{3.29}$$

where R_u is the universal gas constant, $M_{m,w}$ is the molar mass of water and $M_{m,da}$ is the molar mass of dry air. The absolute humidity of humid air can be computed from the relative humidity, as well as the saturation pressure $p_{sat}(t)$ using :

$$x_v = \frac{M_{m,w}}{M_{m,da}} \frac{\phi\, p_{sat}(t)}{p - \phi\, p_{sat}(t)} \tag{3.30}$$

The saturation pressure itself is computed from the temperature t in [°C], using an empirical formula [34] :

$$p_{sat}(t) = \frac{\exp\left(34.494 - \frac{4924.99}{t+237.1}\right)}{(t+105)^{1.57}} \tag{3.31}$$

The relative humidity (ϕ) at each inlet and at the outlet is computed by LabView, based on the provided ambient relative humidity. The latter is retrieved from a sensor located in the same room as the installation. However, there was no humidity sensor located directly on the installation, and therefore the value measured is only an approximation of the real ambient value at the secondary inlet. The hypothesis was also made that the air coming out of the tank has a relative humidity of 1. That is why the various relative humidity values are approximations, giving approximate specific gas constants, but still closer to reality than considering a constant R. For those reasons, it was decided to not take into account the uncertainty on R, because it is not possible to quantify the uncertainty on ϕ. Moreover, this uncertainty would have a negligible impact on the combined uncertainty of the mass flow rates and entrainment ratio.

An estimate of the discharge coefficient can be found with the Reader-Harris/Gallagher formula [35, 36] :

$$\begin{aligned}C_d =&0.5961 + 0.0261\xi^2 - 0.216\xi^8 + 0.000521\left(\frac{10^6\xi}{Re_D}\right)^{0.7}\\&+ (0.0188 + 0.0063A)\xi^{3.5}\left(\frac{10^6}{Re_D}\right)^{0.3}\\&+ \left(0.043 + 0.080e^{-10L_1} - 0.123e^{-7L_1}\right)(1 - 0.11A)\frac{\xi^4}{1-\xi^4}\\&- 0.031(M_2' - 0.8M_2'^{1.1})\xi^{1.3}\end{aligned} \tag{3.32}$$

where $M_2' = \frac{2L_2'}{1-\xi}$ and $A = \left(\frac{19000\xi}{Re_D}\right)^{0.8}$. When the differential pressure is measured using tappings placed at a distance of D upstream and $D/2$ downstream of the orifice place, in accordance with the requirements of the ISO 5167 standard [25], the characteristic lengths are $L_1 = 1$ and $L_2' = 0.47$. The Reynolds number Re_D is :

$$Re_D = \frac{4\dot{m}}{\pi\mu_a D} \tag{3.33}$$

where μ_a is the dynamic viscosity of the fluid upstream of the orifice plate. The latter depends on the nature of the fluid and on its temperature. It can be approximated by Sutherland's law [37] :

$$\mu(T) \approx \mu_0\left(\frac{T}{T_0}\right)^{3/2}\frac{T_0 + S_\mu}{T + S_\mu} \tag{3.34}$$

The reference temperature T_0 is 273.15 [K]. For air, the reference dynamic viscosity μ_0 at T_0 and the Sutherland constant S_μ are respectively equal to 1.716×10^{-5} [Pa s] and 110.4 [K].

The expansibility factor can be estimated with an empirical formula [38] :

$$\epsilon = 1 - (0.351 + 0.256\xi^4 + 0.93\xi^8)\left[1 - \left(\frac{p_b}{p_a}\right)^{1/\gamma}\right] \tag{3.35}$$

where p_b is $p_a - \Delta p$.

Since the mass flow rate depends on the discharge coefficient, which itself depends on the mass flow rate through the Reynolds number, an iterative procedure must be applied to determine both quantities, as explained in the ISO 5167 standard

[24]. By replacing the expression of the mass flow rate from Equation (3.25) in Equation (3.33), the following relation is obtained :

$$\frac{Re_D}{C_d} = \frac{\epsilon d^2 \sqrt{2\rho_a \Delta p}}{\mu_a D \sqrt{1-\xi^4}} = I \tag{3.36}$$

In this relation, everything on the left-hand side is unknown, while the right-hand side regroups all known values. The latter term is then referred as the "invariant" member, hence the denotation I. The use of a linear algorithm for the iterative process allows a rapid convergence. The variable X used in this algorithm is :

$$X = Re_D = C_d I \tag{3.37}$$

The difference between the known and unknown members is δ. After making a first guess with $X_1 = C_{d\infty} I$, where $C_{d\infty}$ is the discharge coefficient at infinite Reynolds number, a difference $\delta_1 = I - \frac{X_1}{C_{d\infty}}$ is obtained. Then C_d is computed from X_1, which gives a second guess X_2, resulting in a difference δ_2. To get the next guesses, a linear algorithm is used instead of successive substitutions to have a faster convergence :

$$X_n = X_{n-1} - \delta_{n-1} \frac{X_{n-1} - X_{n-2}}{\delta_{n-1} - \delta_{n-2}} \tag{3.38}$$

Convergence is assumed to be reached when $\left|\frac{\delta_n}{I}\right| < 10^{-5}$. The mass flow rate is then :

$$\dot{m} = \frac{\pi \mu_a D}{4} X_n \tag{3.39}$$

It must be recalled that all measured quantities used in this iterative determination of the mass flow rate are actually the estimates of those quantities, and more precisely their average over the different independent observations. However, for the sake of readability the notation "$\bar{\cdot}$" representing the average was omitted in the preceding development.

Uncertainty on the mass flow rate

To compute the uncertainty on $\dot{m}$, Equation (3.9)b is applied on Equation (3.25). It is however assumed that the uncertainties of C_d, ϵ, d, Δp and ρ_a are independent. The contribution to the combined uncertainty due to the covariance terms can be neglected, as explained in the ISO 5167 standard [24]. Therefore, the expression for the uncertainty on $\dot{m}$ can be derived, taking into account the interdependence between C_d and throat and pipe dimensions. Also, the deviations of C_d due to the dependence on the Reynolds number are of second order and are thus included in the uncertainty on C_d. Similarly, the uncertainty in ϵ encompasses deviations arising from uncertainties on ξ, the pressure ratio, and γ.

Using these hypotheses and applying Equation (3.9)b, the equation that relates the relative uncertainty of the mass flow rate to the relative uncertainties of the quantities it depends on can be derived. The concept of relative uncertainty has not been introduced yet. It refers to the ratio of the uncertainty of a quantity to the estimate of that quantity. Using relative uncertainties greatly simplifies combined uncertainty equations. The relative uncertainty of the mass flow rate, $\dot{m}$, is then :

$$\left(\frac{u(\bar{\dot{m}})}{\bar{\dot{m}}}\right)^2 = \left(\frac{u(\overline{C_d})}{\overline{C_d}}\right)^2 + \left(\frac{u(\bar{\epsilon})}{\bar{\epsilon}}\right)^2 + \left(\frac{2\bar{\xi}^4}{1-\bar{\xi}^4}\right)^2 \left(\frac{u(\bar{D})}{\bar{D}}\right)^2 + \left(\frac{2}{1-\bar{\xi}^4}\right)^2 \left(\frac{u(\bar{d})}{\bar{d}}\right)^2 + \frac{1}{4}\left(\frac{u(\overline{\Delta p})}{\overline{\Delta p}}\right)^2 + \frac{1}{4}\left(\frac{u(\overline{\rho_a})}{\overline{\rho_a}}\right)^2 \tag{3.40}$$

The uncertainties on C_d and ϵ are determined from the standard ISO 5167 for the applicable part of orifice plates [25]. What is given in the standard concerning C_d is the value of its relative expanded uncertainty for $k_p = 2$. However, this value depends on the orifice plate geometry and Reynolds number. Since the orifice plates measuring the secondary and total mass flow rates have a ξ comprised between 0.2 and 0.6 (0.28 and 0.42, respectively), the relative expanded uncertainty for $k_p = 2$ on C_d is 0.5%. On the other hand, since the ξ of the primary stream orifice plate lies between 0.6 and 0.75 (approximately 0.71), the relative expanded uncertainty for $k_p = 2$ on C_d is $(1.667\xi - 0.5)\%$ for this one. Moreover, since its ξ exceeds 0.5, an additional 0.5% of uncertainty must be added if the Reynolds number Re_D of the primary stream happen to be inferior to 10 000.

The uncertainty on ϵ will depend on the pressure measurements. Indeed, the relative expanded uncertainty of ϵ at $k_p = 2$ is : $3.5\frac{\Delta p}{\gamma p_a}\%$, where γ is the isentropic exponent of the fluid, which is approximated to 1.4 for air. Those relative expanded uncertainties must be divided by k_p to recover the relative standard uncertainties used in Equation (3.40).

Concerning the uncertainties on the diameters D and d, those are found with the specifications for orifice plates from [25]. It states that the orifice diameter d shall not differ by more than 0.05%, while the pipe diameter D shall not differ by more than 0.3%. Those are assumed to be rectangular distribution, and therefore shall be divided by $\sqrt{3}$, according to Equation (3.4).

The pressure differential Δp is measured directly around the orifice plate. Its estimate will be evaluated as the mean of several independent observations. To compute the uncertainty on Δp, the type A uncertainty coming from the various independent measurements, computed with Equation (3.3), will be added to the type B uncertainty coming from the measuring instrument itself.

$$u^2(\overline{\Delta p}) = u_A^2(\overline{\Delta p}) + u_B^2(\overline{\Delta p}) \tag{3.41}$$

The sensors used to measure this differential pressure are PMD75 from Endress-Hauser. According to their datasheet, they have an accuracy of ±0.05% for the 'platinum' version. Assuming that this corresponds to a rectangular distribution, Equation (3.4) can be used to evaluate the standard uncertainty from the measuring instrument.

$$\frac{u_B(\overline{\Delta p})}{\overline{\Delta p}} = \frac{0.05\%}{\sqrt{3}} \approx 0.03\% \tag{3.42}$$

The air density being determined from the measurements of both the pressure and the temperature, a combined uncertainty will be used for ρ_a. The latter is a type

A uncertainty taking into account correlations between the two measured quantities (cfr. Equation (3.9)b). The ideal gas law (Equation (3.28)) leads to the following uncertainty formula :

$$u^2(\overline{\rho}_a) = \frac{1}{(R\overline{T}_a)^2}u^2(\overline{p}_a) + \left(\frac{\overline{p}_a}{R\overline{T}_a^2}\right)^2 u^2(\overline{T}_a) - \frac{2\overline{p}_a}{R^2\overline{T}_a^3}u(\overline{p}_a, \overline{T}_a) \tag{3.43}$$

Note that the minus sign before the covariance term comes from the negative sign of the partial derivative of ρ_a with respect to T_a. Equation (3.43) can be re-expressed in terms of relative uncertainties :

$$\left(\frac{u(\overline{\rho}_a)}{\overline{\rho}_a}\right)^2 = \left(\frac{u(\overline{p}_a)}{\overline{p}_a}\right)^2 + \left(\frac{u(\overline{T}_a)}{\overline{T}_a}\right)^2 - \frac{2}{\overline{p}_a\overline{T}_a}u(\overline{p}_a, \overline{T}_a) \tag{3.44}$$

The uncertainty of the measured quantities are the squared sum of a type A uncertainty from the n independent observations and a type B uncertainty coming from the measuring instruments.

$$u^2(\overline{p}_a) = u_A^2(\overline{p}_a) + u_B^2(\overline{p}_a) \tag{3.45}$$

$$u^2(\overline{T}_a) = u_A^2(\overline{T}_a) + u_B^2(\overline{T}_a) \tag{3.46}$$

The pressure sensor for the secondary stream is a PMP131 from Endress-Hauser. According to the datasheet, its accuracy is 0.5%, which means that the type B relative standard uncertainty for this sensor would be approximately 0.3%. The pressure sensor for the primary stream is from Kistler, and also has an accuracy of 0.5%, leading to the same relative standard uncertainty. The pressure sensor downstream of the ejector is a PMP21 from Endress-Hauser, with an accuracy of 0.3%, leading to a relative standard uncertainty of about 0.17%. The temperature probes are PT100 RTD. Their uncertainty depends on the measured temperature, but is at most 0.5 [°C]. As a reminder, the sensor locations and their accuracies are gathered in Table 2.1.

If a confidence interval is desired, the effective number of degrees of freedom have to be computed. It is considered that the accuracies prescribed in the datasheet are highly reliable, hence the effective degrees of freedom from the type B evaluation tending to infinity. Then, for instance, the effective number of degrees of freedom of Δp would be, using Equation (3.21) :

$$\nu_{\Delta p} = \frac{u^4(\overline{\Delta p})}{\frac{u_A^4(\overline{\Delta p})}{\nu_A}} \tag{3.47}$$

The same holds for p_a and T_a. Then, the effective number of degrees of freedom of ρ_a would be :

$$\nu_{\rho_a} = \frac{u^4(\overline{\rho_a})}{\frac{(u(\overline{p}_a)/R\overline{T}_a)^4}{\nu_{p_a}} + \frac{(\overline{p}_a u(\overline{T}_a)/R\overline{T}_a^2)^4}{\nu_{T_a}}} \tag{3.48}$$

In the same way, the effective number of degrees of freedom for $\dot{m}$ can be found using Equation (3.40).

$$\nu_{\dot{m}} = \frac{\left(u(\overline{\dot{m}})/\overline{\dot{m}}\right)^4}{\frac{\left(u(\overline{\Delta p})/2\overline{\Delta p}\right)^4}{\nu_{\Delta p}} + \frac{(u(\overline{\rho_a})/2\overline{\rho_a})^4}{\nu_{\rho_a}}} \tag{3.49}$$

Uncertainty on the entrainment ratio

Finally, the uncertainty on ER is :

$$u^2(\overline{ER}) = \left(\frac{\overline{\dot{m}}_2}{\overline{\dot{m}}_1^2}\right)^2 u^2(\overline{\dot{m}}_1) + \left(\frac{1}{\overline{\dot{m}}_1}\right)^2 u^2(\overline{\dot{m}}_2) \tag{3.50}$$

This can re-written using relative uncertainties :

$$\left(\frac{u(\overline{ER})}{\overline{ER}}\right)^2 = \left(\frac{u(\overline{\dot{m}}_1)}{\overline{\dot{m}}_1}\right)^2 + \left(\frac{u(\overline{\dot{m}}_2)}{\overline{\dot{m}}_2}\right)^2 \tag{3.51}$$

The correlated uncertainty between the mass flow rates is not taken into account, as these are not direct measurements but measurands computed from input quantities.

By evaluating the effective number of degrees of freedom of ER, an expanded uncertainty can be calculated to present a confidence interval.

$$\nu_{ER} = \frac{\left(u(\overline{ER})/\overline{ER}\right)^4}{\frac{(u(\overline{\dot{m}}_1)/\overline{\dot{m}}_1)^4}{\nu_{\dot{m}_1}} + \frac{(u(\overline{\dot{m}}_2)/\overline{\dot{m}}_2)^4}{\nu_{\dot{m}_2}}} \tag{3.52}$$

Typically, a confidence interval of 95% is chosen. With such a level of confidence, the coverage factor k_p is around 2.

If the entrainment ratio is computed using Equation (3.24), then its relative uncertainty is computed as follows :

$$\left(\frac{u(\overline{ER})}{\overline{ER}}\right)^2 = \left(\frac{\overline{\dot{m}}_{out} - \overline{\dot{m}}_1}{\overline{\dot{m}}_1}\right)^2 \left[\left(\frac{u(\overline{\dot{m}}_1)}{\overline{\dot{m}}_1}\right)^2 + \left(\frac{u(\overline{\dot{m}}_{out})}{\overline{\dot{m}}_{out}}\right)^2 - \frac{2}{\overline{\dot{m}}_1\overline{\dot{m}}_{out}} u(\overline{\dot{m}}_1, \overline{\dot{m}}_{out})\right] \tag{3.53}$$

The effective number of degrees of freedom is then :

$$\nu_{ER} = \frac{\left(u(\overline{ER})/\overline{ER}\right)^4}{\left(\frac{\overline{\dot{m}}_{out}-\overline{\dot{m}}_1}{\overline{\dot{m}}_1}\right)^4 \left(\frac{(u(\overline{\dot{m}}_1)/\overline{\dot{m}}_1)^4}{\nu_{\dot{m}_1}} + \frac{(u(\overline{\dot{m}}_{out})/\overline{\dot{m}}_{out})^4}{\nu_{\dot{m}_{out}}}\right)} \tag{3.54}$$

3.2.2 Measurement and uncertainty of the pressure along the wall

Another quantity of interest is the ratio $\frac{p_w}{p_{02}}$, where p_w is the static pressure measured along the wall in the ejector. This information is given by the 64 pressures taps as indicated on the P&ID. The pressure at each of those locations will be successively read by a pressure sensor. The latter is a Druck PTX1400, which has a maximum accuracy of 0.25%, leading to a maximum relative standard uncertainty of about 0.15%. The uncertainty on this wall pressure will once again be the combination of a type A uncertainty evaluation based on n independent measurements, and of a type B uncertainty evaluation based on the pressure sensor accuracy.

$$u^2(\overline{p}_w) = u_A^2(\overline{p}_w) + u_B^2(\overline{p}_w) \tag{3.55}$$

The effective number of degrees of freedom is then :

$$\nu_{p_w} = \frac{u^4(\overline{p_w})}{\frac{u_A^4(\overline{p_w})}{n-1}} \tag{3.56}$$

The uncertainty on p_{02} must also be determined. This total pressure can be obtained from the static pressure p_2 with :

$$p_0 = p + \frac{1}{2}\rho u^2 = p + \frac{1}{2\rho}\left(\frac{\dot{m}}{A}\right)^2 \tag{3.57}$$

However, since p_2 is measured in the plenum, the total pressure can be assumed to be equal to the directly measured static pressure. Therefore :

$$u^2(\overline{p}_{02}) \approx u^2(\overline{p}_2) = u_A^2(\overline{p}_2) + u_B^2(\overline{p}_2) \tag{3.58}$$

The sensor there is a PMP131 from Endress-Hauser with an accuracy of 0.5%, which leads to a type B relative standard uncertainty of about 0.3%.

Finally, the relative standard uncertainty on $\frac{p_w}{p_{02}}$ is :

$$\left(\frac{u(\overline{p_w/p_{02}})}{\overline{p_w/p_{02}}}\right)^2 = \left(\frac{u(\overline{p_w})}{\overline{p_w}}\right)^2 + \left(\frac{u(\overline{p_{02}})}{\overline{p_{02}}}\right)^2 - \frac{2}{\overline{p_w}\,\overline{p_{02}}} u(\overline{p_w}, \overline{p_{02}}) \tag{3.59}$$

The covariance between p_w and p_{02} can be determined using a type A covariance evaluation (Equation (3.13)), since those quantities are directly measured from independent measurements. The effective degrees of freedom must be computed to determine the expanded uncertainty corresponding to a confidence interval of 95%.

$$\nu_{p_w/p_{02}} = \frac{\left(\frac{u(\overline{p_w/p_{02}})}{\overline{p_w/p_{02}}}\right)^4}{\frac{(u(\overline{p_w})/\overline{p_w})^4}{\nu_{p_w}} + \frac{(u(\overline{p_{02}})/\overline{p_{02}})^4}{\nu_{p_{02}}}} \tag{3.60}$$

By following the methodology outlined in this chapter, which relies on fundamental theoretical concepts as described in the Guide to the expression of Uncertainty in Measurement (GUM) [23], and adhering to the principles laid out in the ISO 5167 standard for orifice plates [24, 25], one can ensure the attainment of reliable results accompanied by realistic uncertainties. These results are further presented and analyzed in the next chapter.

Chapter 4

Experimental results and comparison with RANS simulations

This chapter aims at presenting the results of the experimental campaign that was realized. The ejector performances have been tested for various operating conditions, by changing the pressure ratios p_{01}/p_{02} and $p_{0,out}/p_{02}$. Initially, the details of the experimental campaign are provided. Subsequently, the 1D models used for comparison with the experimental results are described. On parallel of the measurements, CFD simulations were conducted using a 2D RANS model established by G. Querinjean and N. Baguet [22] on the software Ansys Fluent; the setup for these simulations is briefly explained. The boundary conditions have been set based on the experimental values. For each of the conditions p_{01}/p_{02}, the measurements and simulations are compared through the characteristic curve, i.e. the entrainment ratio, as well as the pressure along the ejector wall. For further analysis, the sum of the inlet mass flow rates will be compared with the measured total mass flow rate.

4.1 Experimental Campaign

This section outlines the experimental campaign conducted to evaluate the performance of the ejector under various operating conditions. The choice of conditions and limitations restricting this choice, as well as the systematic approach to testing each scenario, are outlined.

4.1.1 Choice of the operating conditions

The choice of the tested operating conditions (p_{01}/p_{02} and $p_{0,out}/p_{02}$) was primarily inspired by the conditions assessed numerically by N. Baguet and G. Querinjean in their Master's thesis [22]. Concerning the inlet pressure ratio p_{01}/p_{02}, they investigated 6 cases : ratios of 3, 4, 5, 5.39, 6 and 7. The three first inlet conditions exhibit a compound-like regime, whereas the last two ratios, 6 and 7, feature a Fabri-like regime. Those regimes are a way to classify the conditions according to the flow topology. The case $p_{01}/p_{02} = 5.39$ corresponds to the transition between both regimes, at least in the RANS simulations.

A Fabri-like regime, present for lower p_{01}/p_{02} ratios, corresponds to conditions where the secondary flow reaches sonic speeds. This regime is characterized by the presence of Fabri-patterns in the Mach number field of the flow. Fabri-patterns are well-delimited areas, in which the secondary stream becomes supersonic. The entrance of this area is then a sonic section, whereas the exit is a normal shock, bringing back the secondary flow to a subsonic velocity and increasing its pressure. These Fabri-patterns are circled in black on the left of Figure 4.1, appearing as small pockets on the way of the secondary stream. The presence of Fabri-patterns does not necessarily indicate complete Fabri-choking.

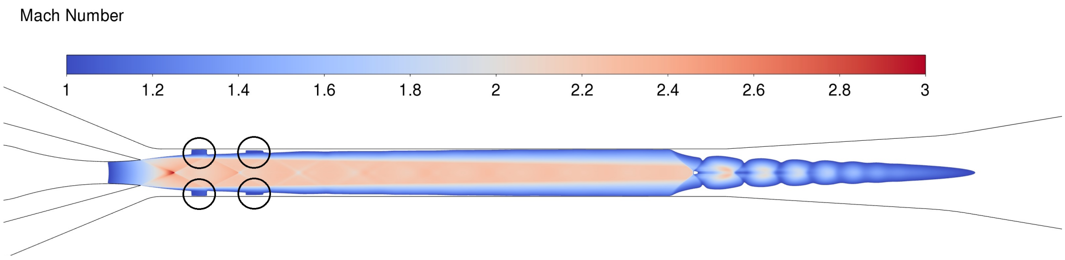

Figure 4.1: Evidence of the presence of Fabri-patterns for the case $p_{01}/p_{02} = 6$ and $p_{0,out}/p_{02} = 1.6$.

On the other hand, a flow in compound-like regime, present for higher p_{01}/p_{02} ratios, does not display Fabri-patterns, indicating that the secondary flow does not reach sonic speeds. As its name suggests, this regime must therefore exhibits a compound-like choking of the secondary flow, meaning that the latter becomes compound-sonic, as outlined by the theory of Bernstein et al. [5].

The ratio $p_{01}/p_{02} = 5.39$ is the condition were the first Fabri-pattern appears in the simulations. However, it was not tested experimentally. Indeed, reaching very precise conditions is difficult due to the oscillations of the inlet primary pressure. Capturing exactly the transition between compound-like and Fabri-like regime experimentally would then be very difficult, especially since the conditions for this transition would most likely not be exactly the same numerically and experimentally.

The ratio $p_{01}/p_{02} = 7$ was also not tested due to limitations with the ability of the compressor to maintain a stable primary inlet pressure above approximately 6.5 bar. This limitation arises from the high inlet flow rate demanded to the compressor. While achieving this ratio could have been possible by reducing the secondary inlet pressure through the butterfly valve located there, this option was disregarded due to time constraints on conducting the tests, as explained in subsection 1.3.1. Indeed, with limited time available, the decision was made to prioritize testing fewer ratios multiple times to obtain more refined uncertainties, rather than testing more ratios, which would lead to greater uncertainties. That is also part of the reason why the case $p_{01}/p_{02} = 5.39$ was not tested. Ultimately, the experimental testing focused on the inlet pressure ratios p_{01}/p_{02} of 3, 4, 5 and 6.

The choice of which $p_{0,out}/p_{02}$ to test for each p_{01}/p_{02} was also based on the conditions investigated by N. Baguet and G. Querinjean. However, due to the limitations in precision associated with a butterfly valve, the ratios investigated were rounded to the nearest cent. The conditions were chosen to capture the on-design plateau, the off-design linear behavior, as well as the transitory phase near the critical point. Additionally, more operating conditions were tested at $p_{01}/p_{02} = 6$ because, as it will be discussed later, the critical point found in the simulations is further away from the experimental critical point. Therefore, additional points need to be tested in order to well define both critical points.

The wall pressure profile along the ejector was measured for only some of the tested operating conditions. Measuring a pressure profile is time-consuming, making it impractical to do so for all conditions multiple times. Therefore, it was decided to measure the pressure profile for five different $p_{0,out}/p_{02}$ ratios for each p_{01}/p_{02}. Typically, these include two on-design conditions, one at the ratio corresponding to the critical point, and two off-design conditions. Table 4.1 summarizes all the tested operating conditions. The cases where the wall pressure profile was measured are in bold and underlined.

$\frac{p_{01}}{p_{02}}$	$\frac{p_{0,out}}{p_{02}}$	$\frac{p_{01}}{p_{02}}$	$\frac{p_{0,out}}{p_{02}}$	$\frac{p_{01}}{p_{02}}$	$\frac{p_{0,out}}{p_{02}}$	$\frac{p_{01}}{p_{02}}$	$\frac{p_{0,out}}{p_{02}}$
	1.1		**1.11**		**1.2**		**1.6**
	1.15		**1.3**		**1.6**		**1.8**
	1.16		1.46		**1.75**		1.98
	1.17		1.47		1.77		**2**
3	**1.20**	4	**1.48**	5	1.78	6	2.01
	1.25		1.5		1.79		2.03
	1.30		1.51		**1.8**		**2.05**
	1.35		1.52		1.81		2.06
	1.40		1.56		1.82		2.07
	1.45		**1.6**		**1.85**		2.08
			1.7		1.95		**2.1**
							2.2

Table 4.1: Tested operating conditions.

For each inlet pressure ratio p_{01}/p_{02}, the measurements were taken at least $n = 5$ times on different occasions to ensure independent measurements. This approach was used to have a meaningful type A evaluation of measurement uncertainties, as explained in the previous chapter.

4.1.2 Test execution procedure

For each operating condition, measurements were recorded over a specific period to be time-averaged, either over 100 seconds or approximately 20 minutes, depending on the tested condition. Averaging over 20 minutes was done when measuring the pressure profile for the current operating condition. In this case, each of the 64 pressure taps was successively switched on for about 15 seconds to obtain a stable static pressure measurement along the wall. Since it takes about 5 seconds for the measurement to stabilize, this allows for a time-averaged measurement over the remaining 10 seconds for each pressure tap. When a pressure profile measurement was not required, the averaging was done over approximately 100 seconds. Considering these factors, testing all the required $p_{0,out}/p_{02}$ ratios for a certain p_{01}/p_{02} took approximately 150 minutes.

Typically, the test sequence begins by setting the desired ratio p_{01}/p_{02} using the motive pressure to control the pressure regulator, as explained in chapter 2. Then, each of the ratios $p_{0,out}/p_{02}$ corresponding to the desired p_{01}/p_{02} is successively reached by adjusting the outlet butterfly valve. During off-design conditions, the motive pressure p_{01} must be modified between measurements at each $p_{0,out}/p_{02}$. This is necessary because changing this ratio beyond the critical point affects the secondary mass flow rate $\dot{m}_2$. The secondary inlet pressure p_{02} is measured in the plenum, which is located after the orifice plate used for measuring the mass flow rate. Consequently, as the mass flow rate changes, the differential pressure across the orifice plate also changes, leading to a variation in p_{02}. In other words, although the ambient pressure remains constant, the pressure loss changes, thereby altering p_{02}. Therefore, to maintain a constant ratio p_{01}/p_{02}, p_{01} must be adjusted accordingly, which will also cause $\dot{m}_1$ to vary during the test sequence.

4.2 1-D compound-choking models

Some 1-D thermodynamic models can be used to predict the performance of supersonic ejectors. These models were already introduced in subsection 1.2.3. The purpose of this section is to develop them. More specifically, the isentropic model developed by Bernstein et al. [5] to predict the entrainment ratio and equivalent critical pressure p^*_{eq} in on-design conditions will be firstly studied. Then, the non-isentropic model developed recently by Metsue et al. [14] will be exposed. The latter is able to predict the entrainment ratio in both on-design and off-design operation, using isentropic efficiencies.

A comparison between the non-isentropic model and RANS simulations was already performed in the master's thesis of N. Baguet and G. Querinjean [22]. The best fitting isentropic efficiencies were also determined for each key inlet pressure ratio in order to better match the simulations.

4.2.1 Isentropic compound-choking model

Based on the compound-choking theory of the secondary flow, and following the assumptions exposed in subsection 1.2.2, Bernstein et al. [5] developed a 1-D model to predict the performance of an ejector in on-design operation. This method was also applied by Lamberts in its PhD thesis [21]. Considering a flow with n streams composed of the same fluid (assuming same γ and R), the mass flow rate of the i^{th} stream is obtained with the following expression, provided the local cross-section

$A_i(x)$ and static pressure $p(x)$ of the stream at any position x :

$$\dot{m}_i = \frac{A_i(x)p_{0i}}{\sqrt{T_{0i}}} \left(\frac{p(x)}{p_{0i}}\right)^{\frac{1}{\gamma}} \sqrt{\frac{2}{R}\left(\frac{\gamma}{\gamma-1}\right)\left[1-\left(\frac{p(x)}{p_{0i}}\right)^{\frac{\gamma-1}{\gamma}}\right]} \tag{4.1}$$

This yields to :

$$\sum_{i=1}^{n} \frac{\dot{m}_i\sqrt{T_{0i}}}{p_{0i}} \left(\frac{p_{0i}}{p(x)}\right)^{\frac{1}{\gamma}} \left\{\frac{2}{R}\left(\frac{\gamma}{\gamma-1}\right)\left[1-\left(\frac{p(x)}{p_{0i}}\right)^{\frac{\gamma-1}{\gamma}}\right]\right\}^{-1/2} = \sum_{i=1}^{n} A_i(x) = A(x) \tag{4.2}$$

Considering only two streams, the following relation can be written :

$$\begin{aligned}\frac{\dot{m}_2}{\dot{m}_1}\sqrt{\frac{T_{02}}{T_{01}}} = &\left\{\frac{A(x)}{A_1^*}\left[\left(\frac{2}{\gamma-1}\right)\left(\frac{\gamma+1}{2}\right)^{\frac{\gamma+1}{\gamma-1}}\right]^{1/2}\right.\\ &\left. -\left(\frac{p_{01}}{p(x)}\right)^{\frac{1}{\gamma}}\left[1-\left(\frac{p(x)}{p_{01}}\right)^{\frac{\gamma-1}{\gamma}}\right]^{-1/2}\right\}\\ &\times\left[1-\left(\frac{p(x)}{p_{02}}\right)^{\frac{\gamma-1}{\gamma}}\right]^{1/2}\left(\frac{p_{02}}{p_{01}}\right)\left(\frac{p(x)}{p_{02}}\right)^{\frac{1}{\gamma}}\end{aligned} \tag{4.3}$$

where

$$A_1^* = \frac{\dot{m}_1\sqrt{T_{01}}}{p_{01}}\sqrt{\frac{R}{\gamma}\left(\frac{\gamma+1}{2}\right)^{\frac{\gamma+1}{\gamma-1}}} \tag{4.4}$$

Then, using the expression relating the local Mach number $M_i(x)$ to the local static pressure $p(x)$ of the i^{th} stream,

$$M_i^2(x) = \frac{2}{\gamma-1}\left[\left(\frac{p_{0i}}{p(x)}\right)^{\frac{\gamma-1}{\gamma}}-1\right] \tag{4.5}$$

and using the fact that when the flow is choked, its behaviour is determined by the throat, i.e. where $\beta = 0$, one can derive the following equation for two streams. It combines the above equation and the expression of β already defined in Equation (1.1).

$$\frac{\dot{m}_2}{\dot{m}_1}\sqrt{\frac{T_{02}}{T_{01}}} = \left(\frac{p_{02}}{p_{01}}\right)^{\frac{\gamma-1}{\gamma}} \frac{\left\{\frac{\gamma-1}{2}\left[\left(\frac{p_{eq}^*}{p_{01}}\right)^{\frac{1-\gamma}{\gamma}}-1\right]^{-1}-1\right\}\left[1-\left(\frac{p_{eq}^*}{p_{02}}\right)^{\frac{\gamma-1}{\gamma}}\right]^{1/2}}{\left\{1-\frac{\gamma-1}{2}\left[\left(\frac{p_{eq}^*}{p_{02}}\right)^{\frac{1-\gamma}{\gamma}}-1\right]^{-1}\right\}\left[1-\left(\frac{p_{eq}^*}{p_{01}}\right)^{\frac{\gamma-1}{\gamma}}\right]^{1/2}} \tag{4.6}$$

The variable p_{eq}^* is the static pressure corresponding to the compound-choking condition ($\beta = 0$). In order to determine the entrainment ratio, Equations (4.3) and (4.6) can be equated and solved iteratively. Indeed, if the local variables of Equation (4.3) are taken at the geometrical throat of the compound-choking, $p(x)$ becomes p_{eq}^*. Since the compound-choking happens in the mixing duct, $A(x)$ is actually A_m, the mixing duct cross-section. Also, since the primary flow is supposed to be isentropic, A_1^* corresponds to A_t, the cross-sectional area of the throat of the primary nozzle. Therefore, since the geometry of the ejector is known, and since both inlet total pressures and temperatures as well as γ are also known, the only unknown left when equating both equations is p_{eq}^*. The on-design entrainment ratio $ER = \frac{\dot{m}_2}{\dot{m}_1}$ can then be easily computed from one of the equations with the previously obtained p_{eq}^*.

4.2.2 Non-isentropic compound-choking model

The non-isentropic 1-D compound-choking model of Metsue et al. [14] will be used here. It is based on the model developed by Chen et al. [9]. This model, whose algorithm is described in [14], allows to predict the entrainment ratio of the ejector in both on-design and off-design operation. As the previous model, it takes as an input the total inlet pressures and temperatures, as well as the ejector geometry. On top of that, the back-pressure must also be provided to the model to determine if the operation is on-design or off-design, depending if it is smaller or greater than the critical back-pressure p_{out}^*. In the latter case, an iterative process is made on the pressure at the hypothetical throat of the compound-choking, in order to have an outlet pressure that matches the provided back-pressure. Also, this model requires several isentropic efficiencies, namely :

$$\begin{cases} \eta_1 & \text{Primary flow in the nozzle isentropic efficiency} \\ \eta_2 & \text{Secondary flow isentropic efficiency} \\ \eta_{1,y} & \text{Primary flow in the mixing chamber isentropic efficiency} \\ \eta_m & \text{Mixing isentropic efficiency} \\ \eta_d & \text{Diffuser isentropic efficiency} \end{cases}$$

For each inlet pressure ratio, a fitting of the isentropic efficiencies can be done to match the simulations as close as possible. The results of this model are shown and compared with simulations and experimental data in section C.4 of Appendix C.

4.3 CFD setup

The CFD setup that was used to obtain the simulated results will be briefly explained, based on the work of N. Baguet and G. Querinjean [22]. Most of the setup, i.e. the geometry, the mesh and all the parameters of the solver, was left unchanged compared to what has been used in their Master's thesis. In fact, the only major update, as mentioned earlier in subsection 2.1.1, is on the NXP whose value was changed to match the real one obtained through the assembly done by the technicians.

First, the software utilized throughout the year is *ANSYS Fluent 2023 R2* (student version), which implements the RANS equations to perform the simulations. The chosen flow solver is a pressure-based, in which the pressure field is obtained through a pressure correction equation, itself derived from the continuity and momentum equations.

Then, the turbulence closure model is a $k - \omega$ SST (Shear Stress Transport). It has been chosen according to the type of application, which involves supersonic velocities and stream mixing. The viscous heating and the compressibility effects are also considered.

Further, since the problem is axisymmetric, the geometry consists of half the ejector. The numerical domain starts at the end of the T-connection, or the beginning of the convergent section of the ejector shroud, and extends up to the end of the industrial divergent (see Figure 4.2).

Finally, the boundary conditions regarding the total pressures and total temperatures were the ones taken from the measurements to ensure reliable comparisons.

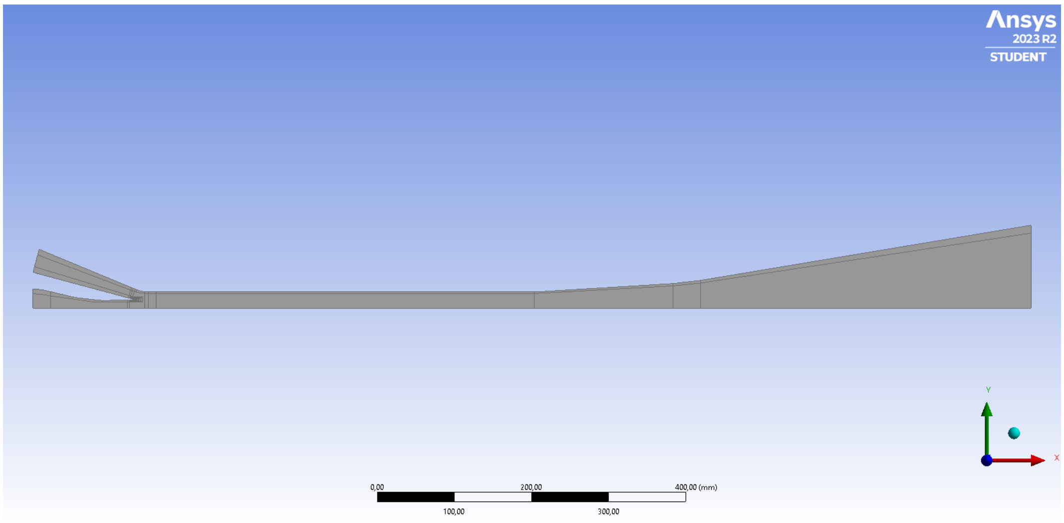

Figure 4.2: Geometry of the ejector used in the CFD setup.

4.4 Characteristic curves

Figure 4.3 displays the characteristic curves for each of the tested inlet pressure ratios p_{01}/p_{02}. The curves obtained from RANS simulations are depicted with hollow circles and dash-dot lines, while those from experimental data are shown with solid points and dashed lines. Error bars represent the uncertainty on the entrainment ratio for each operating condition, corresponding to the expanded uncertainty with a 95% confidence interval.

At first glance, two main observations can be made from this comparison. First, the experimental curve consistently lies below the RANS curve for every p_{01}/p_{02}. Specifically, the on-design entrainment ratio is overestimated by the RANS simulations. However, this discrepancy tends to diminish in absolute value as p_{01}/p_{02} increases. Secondly, the critical back-pressure $p^*_{0,out}/p_{02}$, which denotes the back-pressure at which the ejector is considered to be off-design, is observed to be lower in reality compared to the simulations, particularly at higher p_{01}/p_{02}. Additionally, the transition from on-design to off-design conditions is much smoother in the experimental data compared to the sharp decline observed in the CFD results at higher p_{01}/p_{02}. These observations will be investigated in further detail in the following subsections.

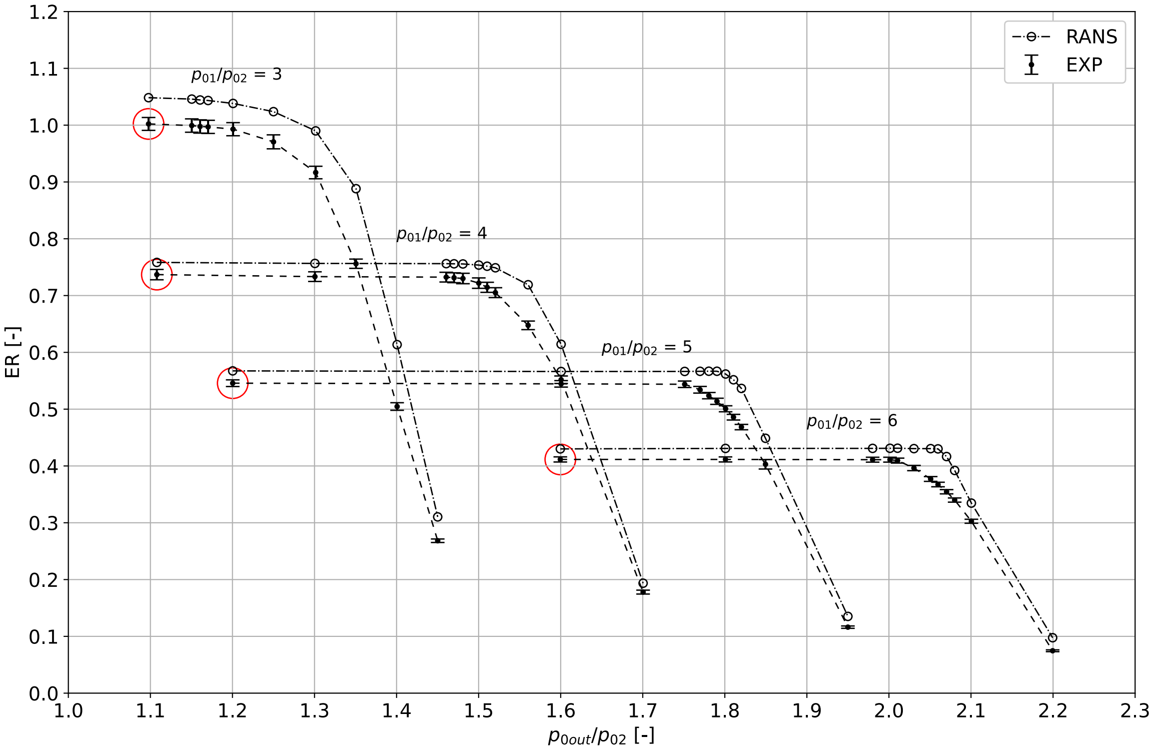

Figure 4.3: Experimental and numerical characteristic curves for each of the tested inlet pressure ratios p_{01}/p_{02}.

4.4.1 Investigation of the differences for on-design conditions

Entrainment ratio

First of all, the first on-design condition for each p_{01}/p_{02}, circled in red in Figure 4.3, will be studied here. The evolution of the on-design entrainment ratio, determined experimentally, from 2D RANS simulations, and from the 1D isentropic model by Bernstein et al. [5], with respect to p_{01}/p_{02}, is shown in Figure 4.4. The absolute difference between the CFD results and the experimental data appears to decrease slightly as the pressure ratio increases. To illustrate this more clearly, the on-design entrainment ratio predicted by the RANS simulations is plotted against the experimental entrainment ratio in Figure 4.5. The solid black line indicates where both entrainment ratios are equal, while the dashed lines represent a ±10%

difference between the simulations and the experimental data. The deviations are calculated relative to the experimental entrainment ratio. This presentation of results is inspired by [21]. The simulations consistently predict a higher entrainment ratio, but always remain within $+10\%$ of the experimental values. The relative error is fairly constant, ranging from about 2.91% to 4.61%. The exact values for each ratio are presented in Table 4.2.

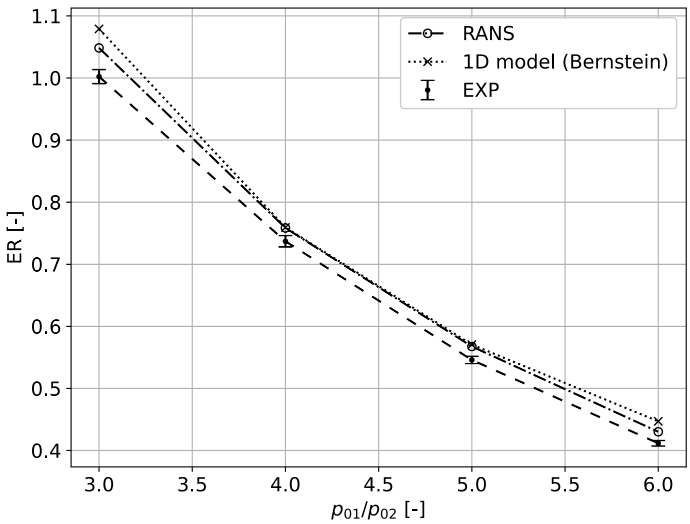

Figure 4.4: On-design entrainment ratio according to the inlet pressure ratio p_{01}/p_{02}.

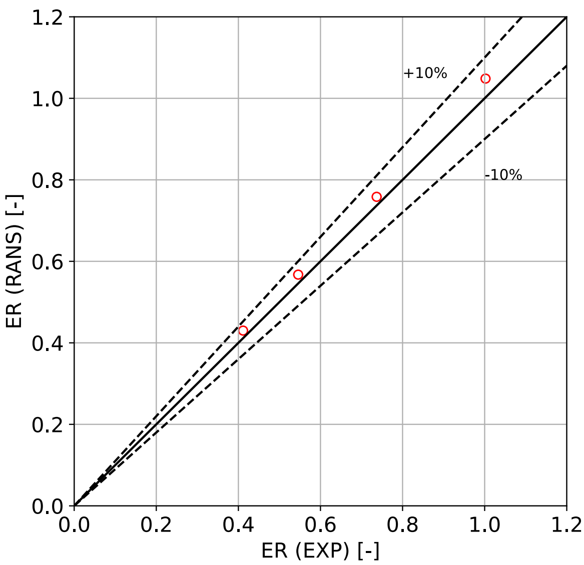

Figure 4.5: Comparison of the RANS simulations with the experimental data concerning the on-design entrainment ratio.

The 1D model also consistently over-predicts the entrainment ratio. However, its relative error varies significantly depending on the ratio, as shown in Figure 4.6. Specifically, the error is around 8% for $p_{01}/p_{02} = 3$ and 6, while it drops to 3% and 4.5%, nearly matching the CFD results, at ratios of 4 and 5. The precise deviation values are also reported in Table 4.2.

This behavior is anticipated. Indeed, G. Querinjean and N. Baguet [22] observed the occurrence of a perfectly expanded case for a pressure ratio of $p_{01}/p_{02} = 4.93$. In the scenario of a perfectly expanded primary flow, the static pressure at the outlet of the nozzle perfectly aligns with that of the secondary stream, avoiding the need for shockwaves or expansion fans. This optimal expansion allows the flow to be more accurately approximated by a 1D model, hence the alignment with the 2D RANS simulations at ratios of 4 and 5. For lower ratios, there is an over-expansion, whereas for higher ratios, there is an under-expansion of the primary flow.

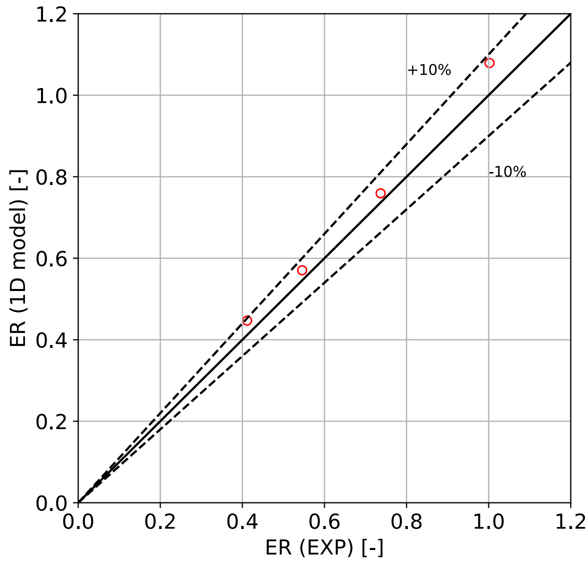

Figure 4.6: Comparison of the 1D compound-choking model from Bernstein et al. [5] with the experimental data concerning the on-design entrainment ratio.

p_{01}/p_{02}	ER (EXP)	ER (RANS)	Deviation [%]	ER (1D)	Deviation [%]
3	1.002 ± 0.011	1.048	+4.61	1.079	+7.67
4	0.737 ± 0.009	0.758	+2.91	0.759	+3.03
5	0.546 ± 0.006	0.567	+3.97	0.570	+4.53
6	0.411 ± 0.005	0.430	+4.51	0.447	+8.59

Table 4.2: On-design entrainment ratios obtained experimentally, with 2D RANS simulations and with the 1D isentropic model from Bernstein et al. [5]. The deviations are expressed in percentage of the experimental value.

Mass flow rates

To identify the origin of the deviation between the 2D RANS simulations and the experimental values more precisely, the comparison between the simulated on-design inlet mass flow rates and the measured counterparts is conducted, with respect to the inlet pressure ratio p_{01}/p_{02}. The conditions still correspond to those circled in red in Figure 4.3. The comparisons are presented in Figure 4.7 and Figure 4.8.

Note that here, the mass flow rates were not plotted as such, but rather pseudo non-dimensional mass flow rates were used. Those can be referred as Mass Flow Parameter (MFP) [39] and are computed using total temperature and total pressure.

$$MFP = \frac{\dot{m}\sqrt{T_0}}{p_0} \tag{4.7}$$

The necessity for a pseudo-dimensionless mass flow rate arises from the dimensionless nature of the x-axis, representing a pressure ratio. While typically only the primary inlet pressure is altered, instances may occur where adjustments to the secondary inlet pressure are made via the butterfly valve. Moreover, as explained in subsection 4.1.2, p_{02} also varies between measurements due to the change of $\dot{m}_2$. Consequently, direct comparison of mass flow rates from these tests is flawed, hence the computation of the MFP.

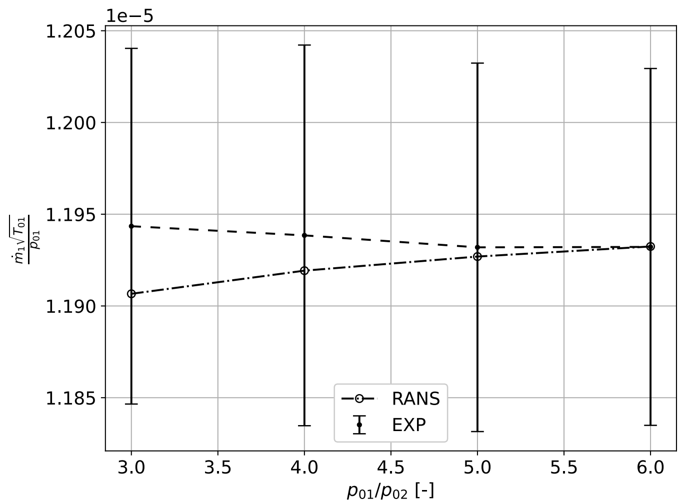

Figure 4.7: On-design primary inlet mass flow rate according to the inlet pressure ratio p_{01}/p_{02}.

To better visualize the deviation of the simulated flow rates from the experimental data, they are plotted in a similar manner as for the entrainment ratio in Figure 4.9. The precise values of the deviations of the predicted mass flow rates with respect to the measured mass flow rates under on-design conditions are presented in Table 4.3 and Table 4.4.

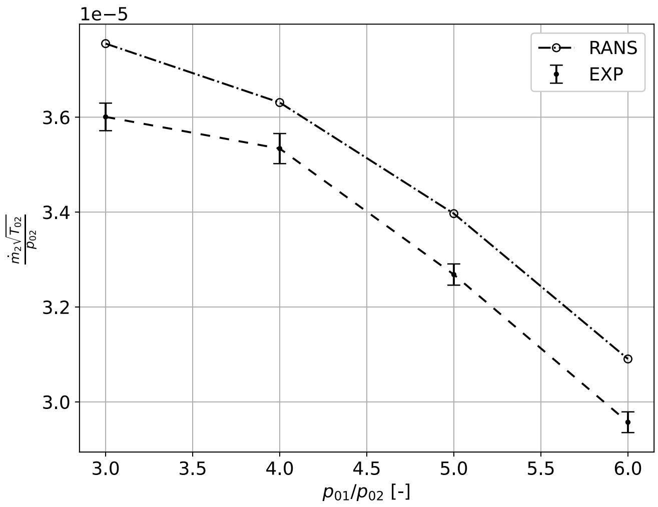

Figure 4.8: On-design secondary inlet mass flow rate according to the inlet pressure ratio p_{01}/p_{02}.

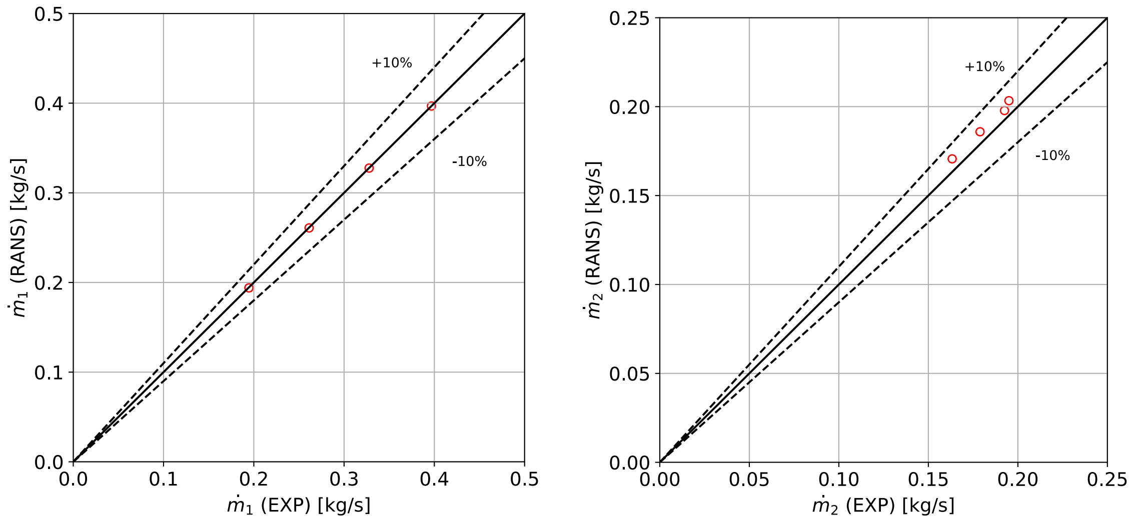

Figure 4.9: Comparison of the RANS simulations with the experimental data concerning the on-design mass flow rates

p_{01}/p_{02}	$\dot{m}_1$ (EXP) [kg/s]	$\dot{m}_1$ (RANS) [kg/s]	Deviation [%]
3	0.195 ± 0.002	0.194	-0.31
4	0.261 ± 0.002	0.261	-0.16
5	0.328 ± 0.003	0.328	-0.04
6	0.397 ± 0.003	0.397	+0.002

Table 4.3: On-design primary mass flow rates

p_{01}/p_{02}	$\dot{m}_2$ (EXP) [kg/s]	$\dot{m}_2$ (RANS) [kg/s]	Deviation [%]
3	0.195 ± 0.002	0.203	+4.29
4	0.193 ± 0.002	0.198	+2.75
5	0.179 ± 0.001	0.186	+3.93
6	0.163 ± 0.001	0.171	+4.51

Table 4.4: On-design secondary mass flow rates

The RANS simulations demonstrate good accuracy in predicting the primary mass flow rate. In fact, the deviation is no larger than 0.31% compared to the actual flow rate at $p_{01}/p_{02} = 3$, and it approaches the true value as the reservoir pressure increases. Furthermore, for each ratio, the predicted $\dot{m}_1$ consistently falls within the uncertainty bars of the experimental measurement.

Conversely, there is a larger deviation in predicting the secondary mass flow rate, although it remains within a range of about 3 to 5%. Specifically, the RANS simulations show a deviation of 4.51% in the worst-case scenario ($p_{01}/p_{02} = 6$), and 2.75% in the best case ($p_{01}/p_{02} = 4$). Hence, it becomes evident that the disparity between experimental data and RANS simulations of the entrainment ratio primarily comes from a difference in the entrained mass flow rate $\dot{m}_2$.

Figure 4.10 provides a summary of the situation by exposing the ratios of the estimated ER, $\dot{m}_1$ and $\dot{m}_2$ over their experimental counterparts. It clearly indicates that the relative deviation of the simulations from the experimental values primarily arises from a discrepancy in predicting the secondary mass flow rate $\dot{m}_2$.

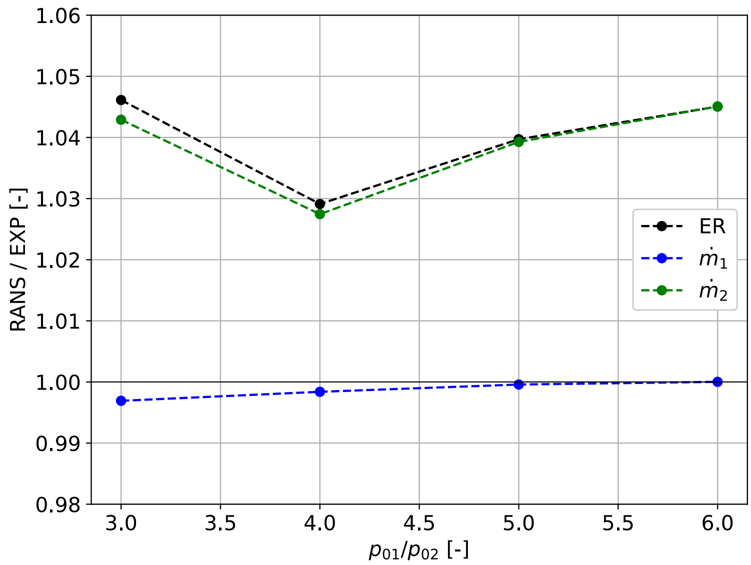

Figure 4.10: Ratios of the predicted on-design entrainment ratio and mass flow rates with 2D RANS simulations, over their experimental value.

Possible causes of the discrepancy

The origin of the discrepancy can be multifaceted. Firstly, it is not uncommon, as observed by the works of Lamberts [21], Hemidi et al. [1], Chen et al. [9], among others. Some effects are not fully considered in the CFD setup, such as 3D effects like wall frictions, as noted by Lamberts [21], and observed by Mazzelli et al. [40] when comparing 2D and 3D models to experimental data. However, the axisymmetric geometry was designed to mitigate these 3D effects. While not entirely eliminated, these effects were indeed reduced, with the on-design error decreasing from about 5.6 to 7.2% with the rectangular ejector in [21], to 2.9 to 4.6% with this axisymmetric ejector.

Regarding the secondary mass flow rate, Lamberts reported errors ranging from 7 to 9%, whereas the error here ranges from 2.8 to 4.5%. The disparity is more pronounced when examining $\dot{m}_2$ because the CFD results overestimated the experimental primary flow rate reported by Lamberts by about 2%, thereby reducing the error on the entrainment ratio. In this case, the 2D RANS simulations are in better agreement with experiments regarding $\dot{m}_1$. Overall, it represents a notable improvement, although some unconsidered effects must still remain to explain the remaining gap.

One possible clue to the origin of this deviation could be a difference between the measured static secondary pressure p_2, assumed to be equal to p_{02}, and the actual total secondary pressure. The approximation $p_2 \approx p_{02}$ was made because the location where p_2 is measured is a plenum, where the air velocity is close to 0. While not perfectly equal in practice, it is assumed to be sufficiently small to be negligible. However, it would still be valuable to examine the sensitivity of the on-design entrainment ratio with respect to this total secondary pressure p_{02}, i.e., to determine the relative variation $\frac{\Delta p_{02}}{p_{02}}$ for which the RANS simulations would perfectly match the experimental results. This analysis is conducted for the first on-design point with an inlet pressure ratio of $p_{01}/p_{02} = 5$. Those operating conditions are chosen because $\dot{m}_1$ is very well predicted at that point, allowing the investigation to focus solely on improvements in the entrainment ratio (ER) resulting from enhancements in $\dot{m}_2$. The result is that the total pressure of the secondary stream, p_{02}, must be reduced from 94263 [Pa] to 92250 [Pa], giving a relative variation $\frac{\Delta p_{02}}{p_{02}} = -2.13\%$. This means that the total pressure in the simulation must be reduced for both ERs to match, which implies that the total pressure should be lower than the measured static pressure. Since this is not possible, the differences between the simulated and experimental entrainment ratios do not stem from the approximation $p_2 \approx p_{02}$.

To investigate whether this difference originates from the CFD setup parameters, a different turbulence model was applied under the same operating conditions as before ($p_{01}/p_{02} = 5$, $p_{0,out}/p_{02} = 1.2$), i.e. in the on-design regime. Indeed, Hemidi et al. [1] have noted that the turbulence model affects both on-design and off-design predictions. In fact, changing the turbulence model from $k-\omega$ SST to $k-\epsilon$ RNG gives better results in terms of on-design entrainment ratio, as it went down from 0.5684 to 0.5616, reducing the relative error to the real entrainment ratio from 3.78% to 2.55%. However, the $k-\epsilon$ RNG turbulence model is unable to predict sub-critical operation (off-design) accurately, as the simulations return unrealistic values.

Another potential source of error could arise from small differences in geometry between the actual components and the dimensions used in the CFD setup. Even though the geometrical characteristics of the pieces were checked beforehand, some discrepancies may have gone unnoticed. Actually, simulations were conducted considering the lower and upper tolerances on the nozzle throat radius, as well as on the mixing duct radius, which are the most critical dimensions of the ejector setup. However, no significant improvements were observed, except when increasing the tolerances up to tenfold. However, this latter scenario is highly unrealistic.

What might be more plausible are assembly errors, such as the NXP not being correct (as actually was the case, but the numerical geometry was adjusted accordingly, as mentioned in subsection 2.1.1), or the primary pipe not being perfectly coaxial within the T-connection. Even if each piece was manufactured within the imposed tolerances, discrepancies could occur during assembly due to the accumulation of tiny individual errors. Additionally, the way the pieces are mounted together could lead to a loss of coaxiality or other issues that cannot be verified once everything is installed.

To determine if there is any radial pressure variation, the wall static pressure was measured at the four tapped holes located at the first axial position of the ejector shroud, equally spaced radially, under the same conditions. These measurement positions correspond to points 1 and 2, as well as the first two closed points in Figure 2.5. The operating conditions for this measurement were on-design, with $p_{01}/p_{02} = 4$ and $p_{0,put}/p_{02} = 1.11$. Figure 4.11 shows the radial variation of the ratio p_w/p_{02}.

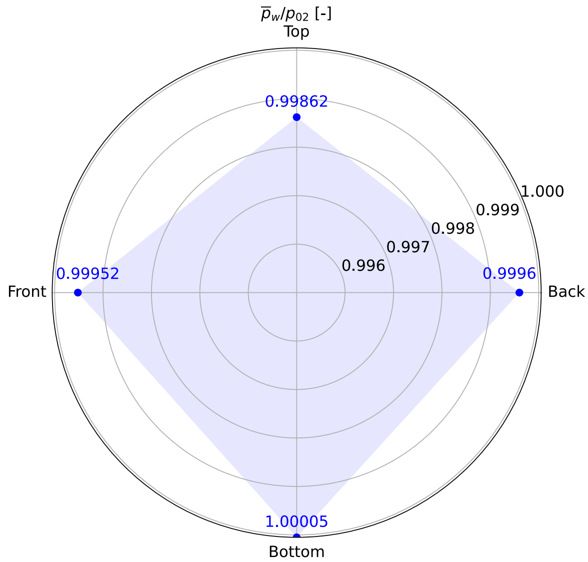

Figure 4.11: Radial variation of the wall static pressure at the first axial measurement position, under the conditions $\frac{p_{01}}{p_{02}} = 4$ and $\frac{p_{0,out}}{p_{02}} = 1.11$.

This axial position corresponds to the very beginning of the convergent section of the ejector. The secondary flow should have a pressure nearly equal to the measured p_{02}. However, only the bottom of the section has a pressure equal to p_{02}, while there is significant depression at the top. The pressures measured at the sides fall logically in between these extremes. This difference could be explained by the asymmetry of the upstream plenum. Specifically, the plenum has a "T" shape, with the sucked flow entering from the top. Consequently, the flow could accumulate at the bottom, leading to decreased pressure at the top compared to the mean pressure in the plenum. Another potential cause could be the primary nozzle not being exactly coaxial with the ejector shroud. For instance, if it is slightly tilted vertically, this misalignment could also cause pressure variations in the sucked flow above and below. This non-symmetry of the flow could contribute to the discrepancies between simulations and experiments.

4.4.2 Investigation of the differences regarding the onset of off-design conditions

As previously mentioned, the RANS simulations differ from the experimental results regarding the transition from on-design to off-design conditions. Specifically, the critical back-pressure $p^*_{0,out}$ is overestimated in CFD. Additionally, as this critical back-pressure is reached, the entrainment ratio decreases sharply in the simulations, while experimentally, the transition is smoother. In the experiments, the ER begins to decrease earlier but more gradually, eventually leading to the same slope of linear decrease for both curves. The behavior then aligns again, maintaining a small gap between the curves as they approach an entrainment ratio of 0.

However, these differences in the transition between on-design and off-design behavior tend to diminish for smaller p_{01}/p_{02} ratios, as the predicted transition becomes smoother and the predicted critical back-pressure aligns more closely with the experimental values. Estimates of the experimental and RANS simulated critical back-pressure ratios are presented in Table 4.5 and plotted in Figure 4.12.

p_{01}/p_{02}	$p^*_{0,out}/p_{02}$ (EXP)	$p^*_{0,out}/p_{02}$ (RANS)
3	1.17	1.17
4	1.47	1.48
5	1.75	1.79
6	2	2.06

Table 4.5: Estimates of the critical back-pressure ratios.

The overestimation of the critical back-pressure by the 2D RANS simulations is most likely due to 3D effects and wall roughness, as outlined by Mazzelli et al. [40]. Indeed, 3D models can capture wall effects, and a significant portion of the primary and secondary stream momentum is lost due to friction with the walls. This loss decreases both the entrainment ratio and the critical back-pressure. These additional losses cannot be captured by the 2D models, thereby delaying the transition to the off-design regime. Furthermore, since the effect of wall roughness is accentuated by the flow velocity, this would explain why the critical back-pressure is even more delayed at higher inlet pressure ratios p_{01}/p_{02}.

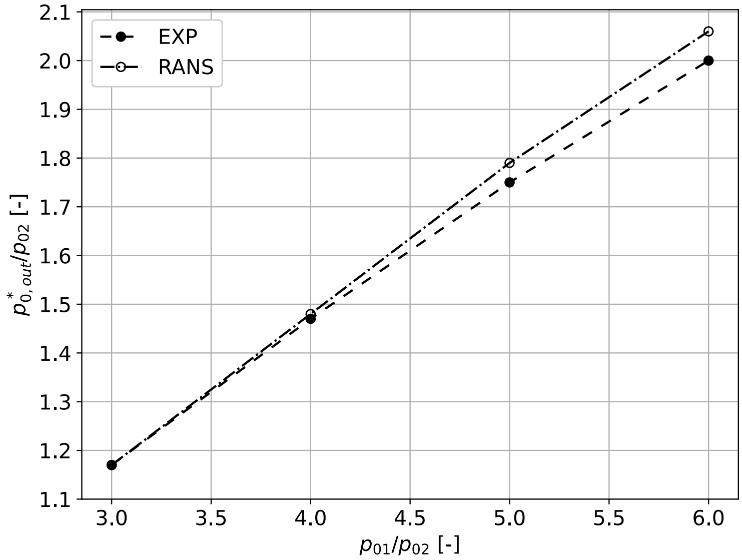

Figure 4.12: Estimates of the critical back-pressure ratios according to the inlet pressure ratio p_{01}/p_{02}.

The slight increase in the predicted entrainment ratio by RANS simulations before entering the predicted off-design regime originates from the delayed critical back-pressure (Mazzelli et al. [40]). This characteristic is especially visible on the curve for $p_{01}/p_{02} = 5$, and somewhat for $p_{01}/p_{02} = 6$. As explained in subsection 4.1.2, the primary inlet pressure must be increased in off-design conditions to compensate for the increased pressure loss through the orifice plate of the secondary stream. However, since the 2D model predicts a later transition to the off-design regime, this higher value of the primary pressure p_{01} is applied to simulations that are still in choked conditions, leading to an increased predicted entrainment ratio.

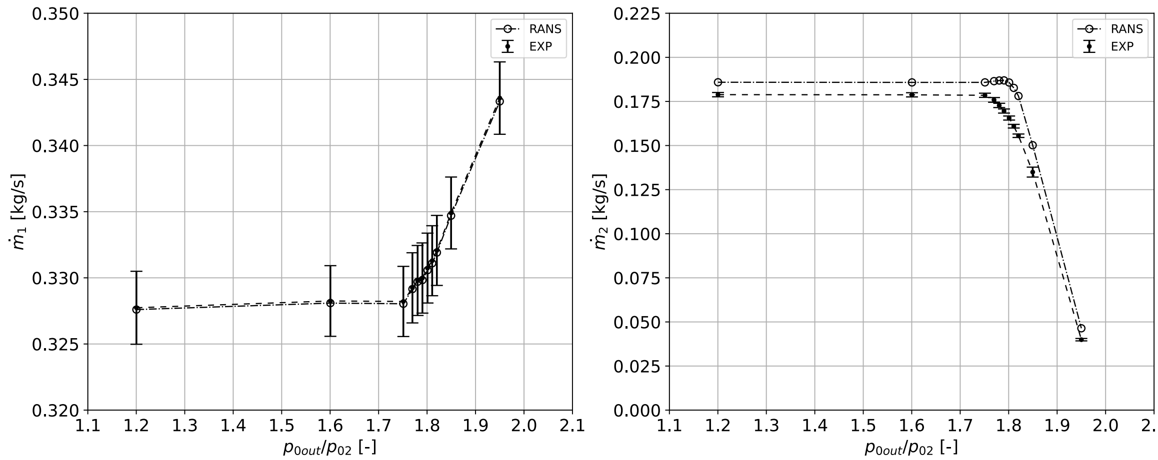

Figure 4.13: Inlet mass flow rates for $\frac{p_{01}}{p_{02}} = 5$.

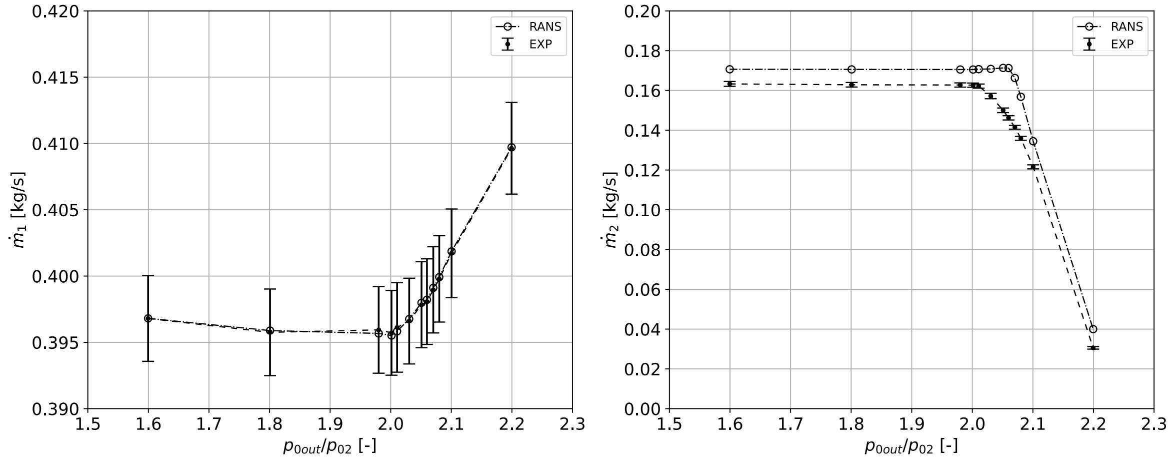

Figure 4.14: Inlet mass flow rates for $\frac{p_{01}}{p_{02}} = 6$.

In Figure 4.13 and Figure 4.14, which show the evolution of the inlet mass flow rates with respect to $p_{0,out}/p_{02}$ for $p_{01}/p_{02} = 5$ and 6, the sudden increase in the primary mass flow rate around the experimental critical back-pressure can be observed. The predicted secondary mass flow rate thus increases, as expected, between the experimental and predicted $p^*_{0,out}$.

4.5 Pressure profile & Flow topology

In this section, the pressure profiles are displayed, showing the evolution of the wall static pressure $\overline{p}_w/p_{02}$ along the ejector, including the convergent section of the secondary flow, the mixing duct, and the diffuser. These pressure profiles were measured for different outlet pressure ratios $p_{0,out}/p_{02}$ for each investigated inlet pressure ratio p_{01}/p_{02}. Typically, pressure profiles were measured for two on-design conditions, two off-design conditions, and at the critical back-pressure. By analyzing these curves, it is possible to identify where choking occurs and compare these observations with RANS simulations. More broadly, the pressure measurements reveal the flow topology within the ejector, allowing for an assessment of whether the observed behavior aligns with theoretical expectations and how the experimental profiles compare to the predicted ones.

The two main cases assessed in this section are the inlet pressure ratios of $p_{01}/p_{02} = 4$ and $p_{01}/p_{02} = 6$. These are representatives of the compound-like regime and Fabri-like regime, respectively. Their characteristic curves are displayed in Figure 4.15 and Figure 4.17. The pressure profiles measured at the outlet conditions outlined in Table 4.1 for these two inlet pressure ratios are shown in Figure 4.16 and Figure 4.18. For clarity, these operating conditions are circled with the corresponding color in the characteristic curves.

The same type of graphs for the cases $p_{01}/p_{02} = 3$ and $p_{01}/p_{02} = 5$ are presented in Appendix C, as they do not add significant information to the discussion compared to the cases already analyzed. Additionally, Appendix C includes the pressure profiles plotted individually for each of the cases.

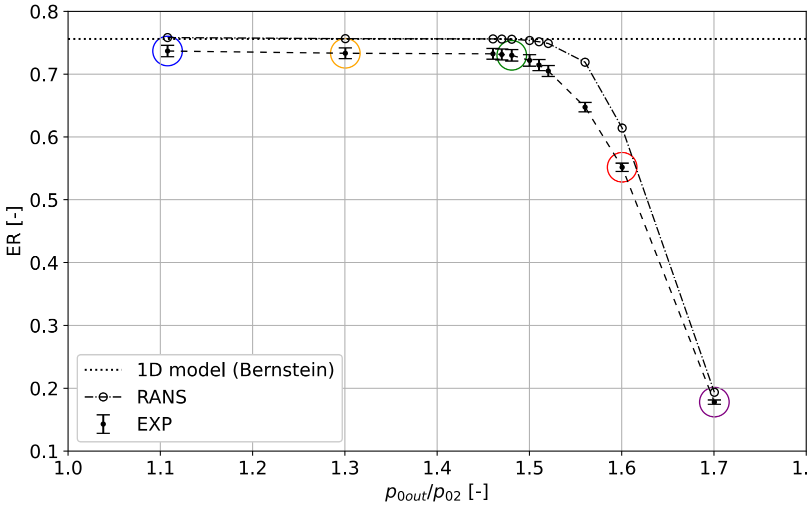

Figure 4.15: Characteristic curve for $\frac{p_{01}}{p_{02}} = 4$.

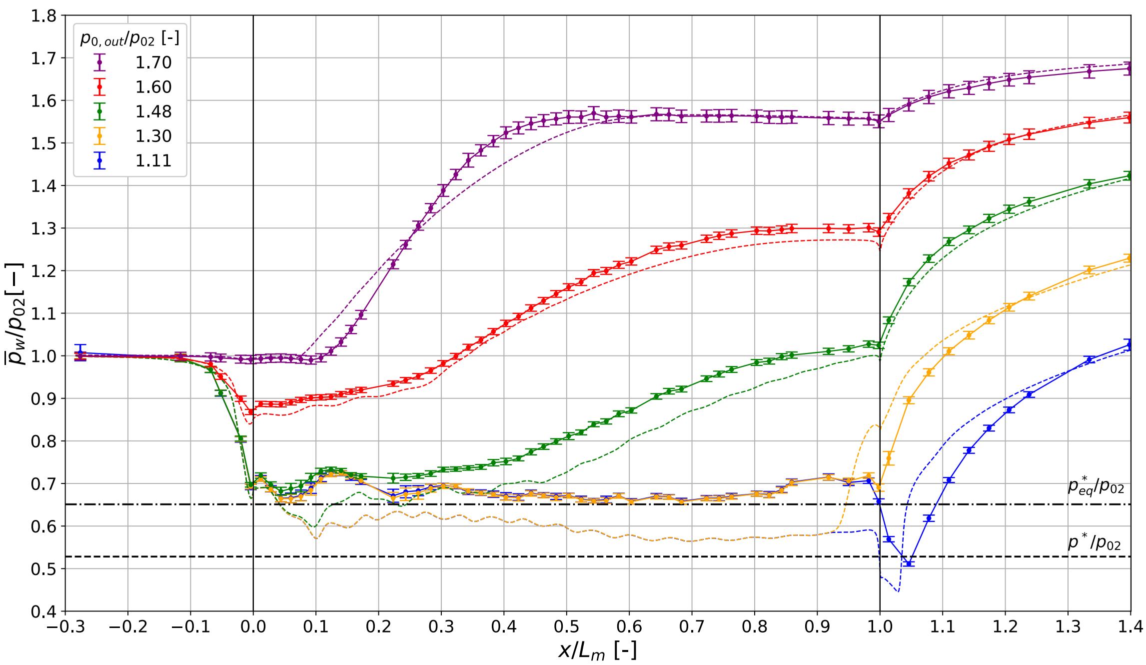

Figure 4.16: Wall static pressure profiles for $\frac{p_{01}}{p_{02}} = 4$.

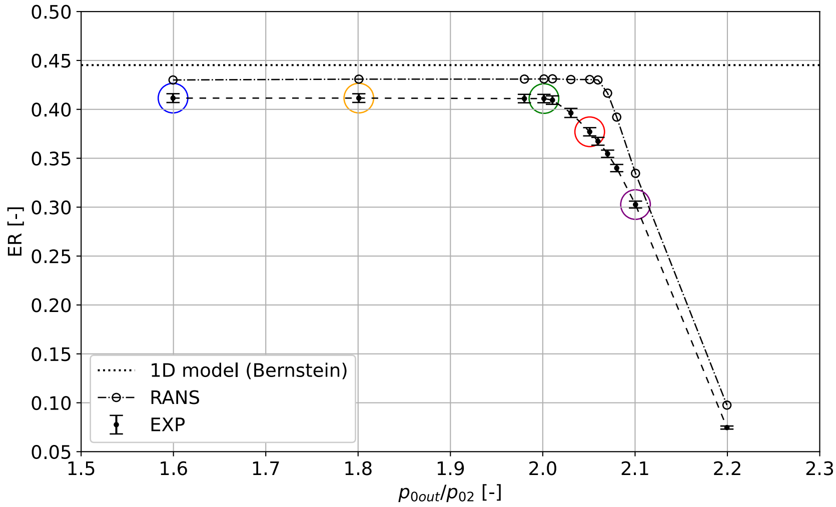

Figure 4.17: Characteristic curve for $\frac{p_{01}}{p_{02}} = 6$.

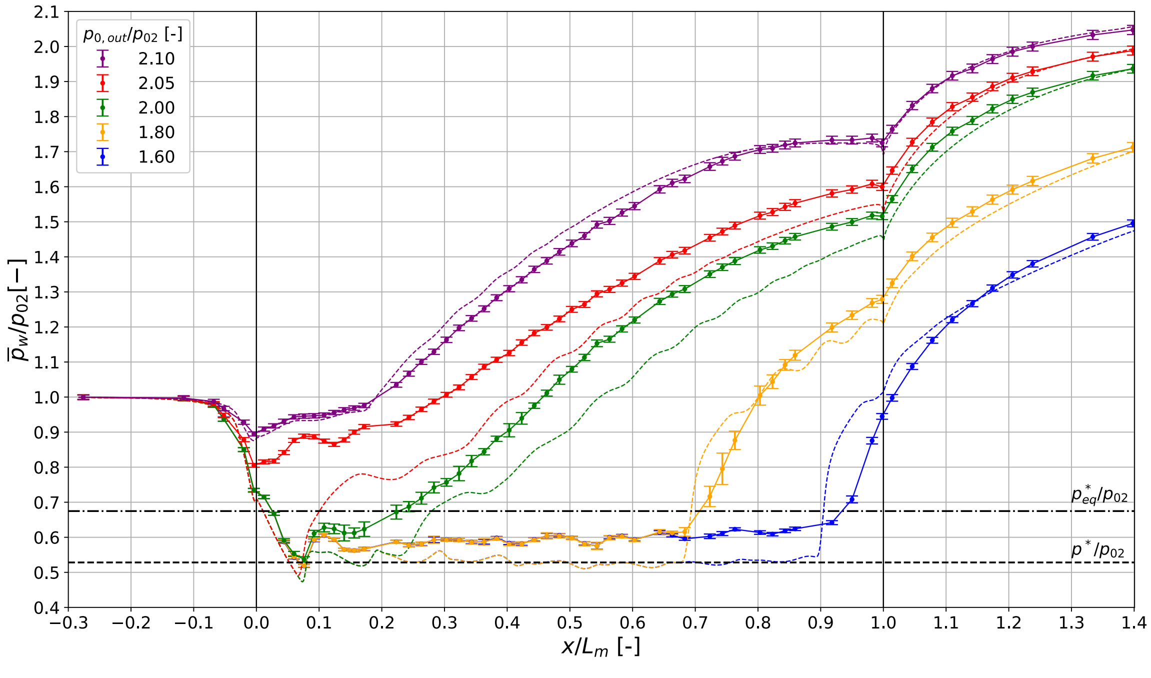

Figure 4.18: Wall static pressure profiles for $\frac{p_{01}}{p_{02}} = 6$.

The x-axis represents the position along the ejector, x, made dimensionless through the mixing duct length L_m. The position $x = 0$ was chosen to be at the beginning of the mixing duct. The experimental wall static pressure profiles are displayed with solid lines and error bars at each measured location, representing the expanded uncertainty for a confidence interval of 95%. It is important to note that the pressure profiles presented here were measured at least $n = 5$ times independently under the same conditions to account for type A uncertainty in the measurements. The corresponding predicted pressure profiles from 2D RANS simulations, obtained by applying the same conditions as the experimental tests, are represented with dashed lines in the corresponding colors.

The black vertical solid lines delimit the mixing duct. The convergent section lies before the first vertical line, while the divergent section is located after the second vertical line.

The horizontal black dashed line on each graph represents the value $\overline{p}_w/p_{02} = p^*/p_{02}$, with p^* being the sonic (or critical) pressure. It is computed as follows :

$$\frac{p^*}{p_{02}} = \left(\frac{\gamma+1}{2}\right)^{-\frac{\gamma}{\gamma-1}} \approx 0.528 \tag{4.8}$$

The horizontal black dash-dotted line, corresponding to p^*_{eq}/p_{02}, is also plotted on these graphs. As explained before, p^*_{eq} is the static pressure which matches the compound-choking condition, $\beta = 0$, in the case of an isentropic model. It can be derived using the method developed by Bernstein et al. [5], and exposed in subsection 4.2.1.

4.5.1 Flow topology

Typically, a pressure profile along the wall of the ejector exhibits the following behavior. Within most of the convergent section, the wall pressure, which corresponds to the pressure of the entrained secondary flow, remains at the inlet value. The pressure then drops to a certain value in the mixing duct, where it oscillates due to the flow patterns. For different on-design outlet conditions, the profile remains consistent up to a certain point because the secondary flow is choked, making it independent of downstream conditions. This point, referred to as the choking section, marks where the profile diverges from those with lower back-pressure. The pressure then increases within the rest of the mixing duct and the diffuser until it matches the required p_{out}. When the regime is off-design, i.e. when the required back-pressure exceeds $p^*_{0,out}$, the departure of the pressure profile occurs sooner, before entering the mixing duct and reaching sonic or compound-sonic conditions. Consequently, the entrained flow is not choked, resulting in the single-choking of the primary flow coming from the nozzle.

The flow behaviour for different regime and operating conditions can be visualized more easily with the Mach number and static pressure fields presented for p_{01}/p_{02} ratios of 4 and 6 in Figure 4.19 and Figure 4.20, respectively.

The first observation from these pressure profiles is that while the on-design entrainment ratio is quite well predicted by the 2D RANS simulations, they fail to accurately capture the real value of the static wall pressure, especially in on-design conditions. Specifically, both curves match very well until a certain point early in the mixing duct, where the experimental curve stops decreasing, while the prediction continues its descent.

In contrast, for strong off-design conditions, such as the cases $p_{0,out}/p_{02} = 1.6$ and $p_{0,out}/p_{02} = 1.7$ in Figure 4.16 and $p_{0,out}/p_{02} = 2.1$ in Figure 4.18, the simulations predict the experimental behavior quite well, with the RANS curve lying within the confidence interval of the experimental curve most of the time.

For on-design and weak off-design conditions, the experimental curve appears to lie with an offset above the predicted curve. Nevertheless, the choking section seems to be reasonably well captured, although this will be explained further in the next section. This offset affects the curve positioning with respect to the sonic pressures discussed earlier.

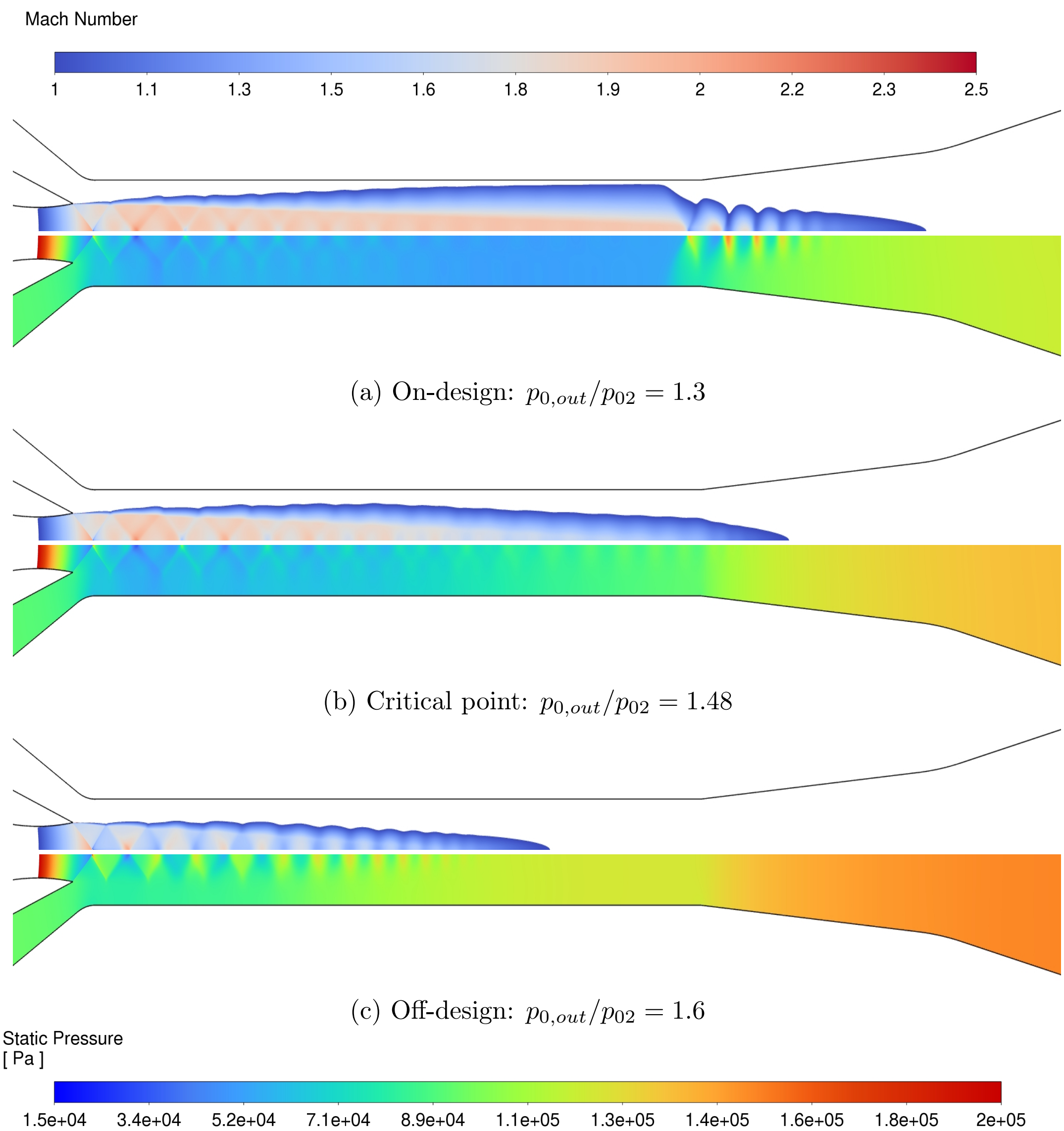

(a) On-design: $p_{0,out}/p_{02} = 1.3$

(b) Critical point: $p_{0,out}/p_{02} = 1.48$

(c) Off-design: $p_{0,out}/p_{02} = 1.6$

Figure 4.19: Mach number (top) and static pressure (bottom) fields for different operating conditions, with $p_{01}/p_{02} = 4$. The fields are presented with a twofold vertical stretching.

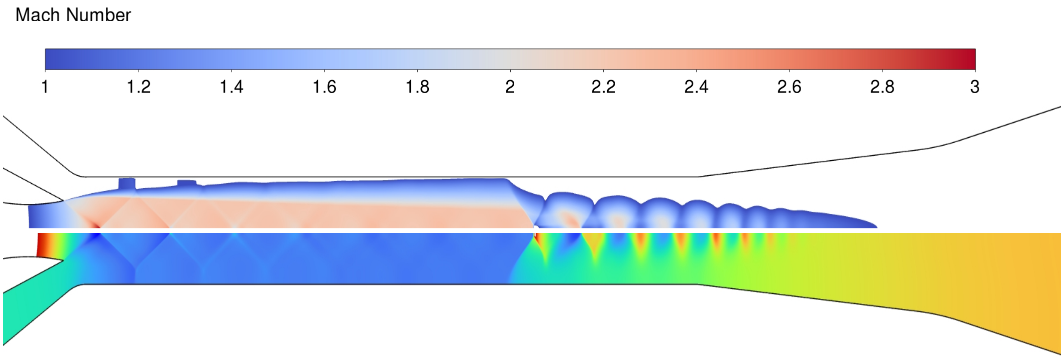

(a) On-design: $p_{0,out}/p_{02} = 1.8$

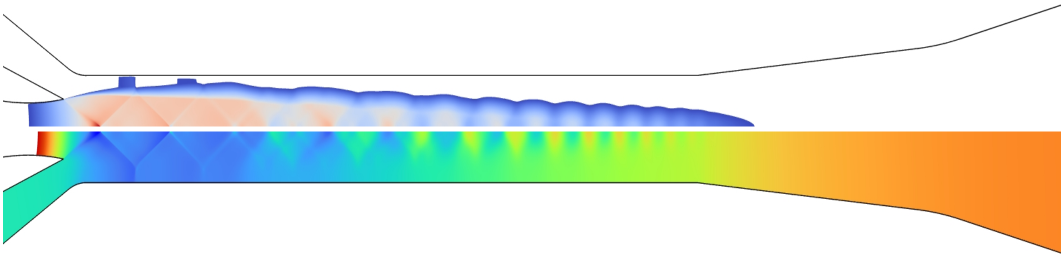

(b) Experimental critical point: $p_{0,out}/p_{02} = 2$

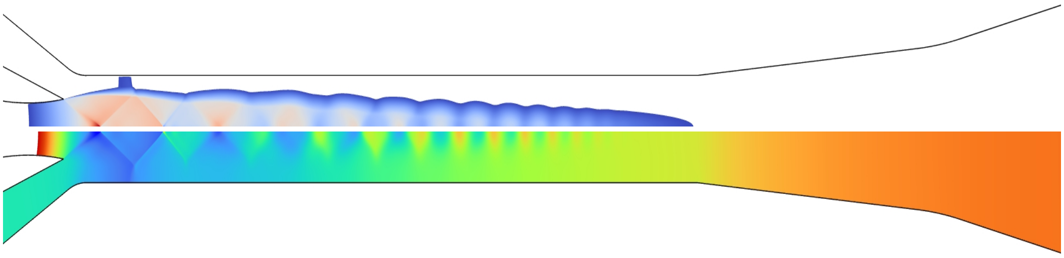

(c) Experimental critical point: $p_{0,out}/p_{02} = 2.05$

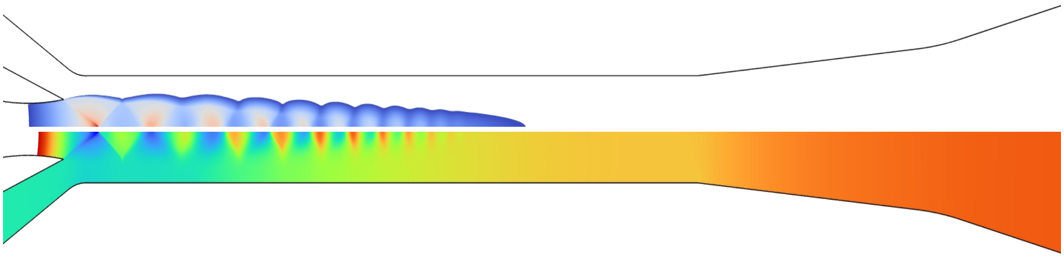

(d) Off-design: $p_{0,out}/p_{02} = 2.1$

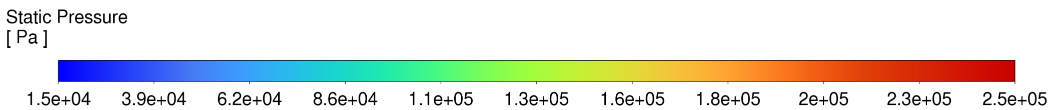

Figure 4.20: Mach number (top) and static pressure (bottom) fields for different operating conditions, with $p_{01}/p_{02} = 6$. The fields are presented with a twofold vertical stretching.

Critical pressure p^*

First, the sonic pressure p^* will be discussed. If a pressure profile drops below this threshold, it indicates that the secondary flow becomes supersonic in the mixing chamber. Reaching this value signifies the presence of a sonic section and thus the presence of Fabri-patterns. Having a pressure below the sonic pressure is therefore characteristic of a Fabri-like regime.

As observed, this occurs with the predicted RANS simulated static pressure for the case $p_{01}/p_{02} = 6$ under on-design conditions with back-pressure ratios of 1.6 and 1.8. To provide a more comprehensive analysis, G. Querinjean and N. Baguet [22] numerically observed that the first appearance of such a phenomenon in the simulations corresponds to the case $p_{01}/p_{02} = 5.39$. This is consistent with the notion that the Fabri-like regime occurs for inlet pressure ratios above 5.39. The characteristic Fabri-patterns can indeed be spotted in the first two cases in Figure 4.20, which both corresponds to on-design conditions in the simulations.

However, the experimental curve does not exhibit the same behavior. At first glance, it may seem that the experimental profile does not cross p^*/p_{02}. However, upon closer inspection, it becomes apparent that the on-design curves still briefly intersect the dashed line at approximately $x/L_m \approx 0.08$. This indicates that the real flow still possesses a sonic section, thus forming a small Fabri-pattern. For smaller p_{01}/p_{02}, the profile would likely not intersect the line. It is indeed the case for $p_{01}/p_{02} = 3$, as observed in Figure C.4. This suggests that the Fabri-choking theory may not be sufficient for the so-called Fabri-like regime, where compound-choking would likely also occur.

Equivalent critical pressure p^*_{eq}

Now, the case $p_{01}/p_{02} = 4$ will be examined, which is representative of the compound-like regime. The horizontal line of interest in this case is the one representing p^*_{eq}, the static pressure that matches the compound-choking condition. Having a wall static pressure below that value would indicate that the flow becomes compound-supersonic, thereby allowing for the compound choking of the secondary flow [21]. As expected, the 2D simulations predict the wall pressure to drop below that line in on-design conditions. No Fabri-pattern are present in that case, since the secondary flow does not become supersonic in the usual sense. The absence of Fabri-patterns for the on-design condition in Figure 4.19 proves it.

However, the experimental on-design curves barely graze the line without crossing it. This suggests that the compound-sonic pressure p^*_{eq} may be underestimated. This discrepancy could arise from the fact that the 1D model computing it assumes isentropic conditions.

It is worth noting that for the case $p_{01}/p_{02} = 5$, which is also a compound-like case and presented in Appendix C, the experimental on-design profiles cross the line p^*_{eq}/p_{02} quite well. This is logical since the on-design wall pressure in the mixing duct decreases as p_{01} increases.

Explanation of the oscillatory behaviour

The oscillatory behaviour of the wall pressure profiles can be explained by the "Y" shock waves visible on the static pressure fields. Indeed, this pattern lead to normal shocks at the wall, and each shock lead to a small pressure rise, and thus a "bump" in the pressure profile. In the case $p_{01}/p_{02} = 4$, the oscillation frequency is higher because the "Y" shock waves are more compact, as observed in Figure 4.19a. On the other hand, those shock waves are more widespread for $p_{01}/p_{02} = 6$, leading to a lower oscillation frequency. Therefore, the oscillatory character of the pressure profile arises from the passage through these shocks.

Possible causes of the difference between experimental and simulated profiles

The systemic discrepancies between the 2D RANS simulations and the experimental data, especially in on-design conditions, are suspected to mainly originate from 3D effects not accounted for in the simulations. Lamberts [21] also observed similar discrepancies and demonstrated that 3D CFD allowed for a better prediction of the static wall pressure. Although the 2D and 3D simulations he conducted predicted nearly the same secondary mass flow rates, the CFD model incorporating 3D effects exhibited a comparatively larger secondary flow passage in the mixing duct. Because static pressure is highly sensitive to the flow area, particularly when it is near its critical value, small variations in the secondary flow passage can lead to notable differences in static pressure. This could explain why the 3D simulations align better with reality. Confirming this hypothesis through the use of 3D CFD simulations on the geometry of this ejector would be an interesting avenue for further investigation.

Changing the 2D CFD turbulence model also have an impact on the estimated wall static pressure profile. In fact, it provides an on-design profile closer to experimental data with the $k-\epsilon$ RNG model. This can be observed on Figure 4.21, where the experimental data is compared to the predictions of the two turbulence models for the case $p_{01}/p_{02} = 5$ and $p_{0,out}/p_{02} = 1.2$. There is however a large pressure bump at the mixing duct which is not present in reality. Additionally, as already explained, this turbulence model fails to predict realistic results for the critical point and off-design regime.

Additionally, the pressure difference observed between the top and bottom of the ejector shroud at the inlet of the secondary flow in Figure 4.11 impacts at least the initial points of the profiles. Since the wall static pressure is only measured at the top (except at the first axial position) and is lower there, the wall static pressure averaged over the entire circumference of the ejector shroud would certainly be higher. This would slightly shift the experimental profiles upwards, thereby increasing the gap with the RANS simulated profiles.

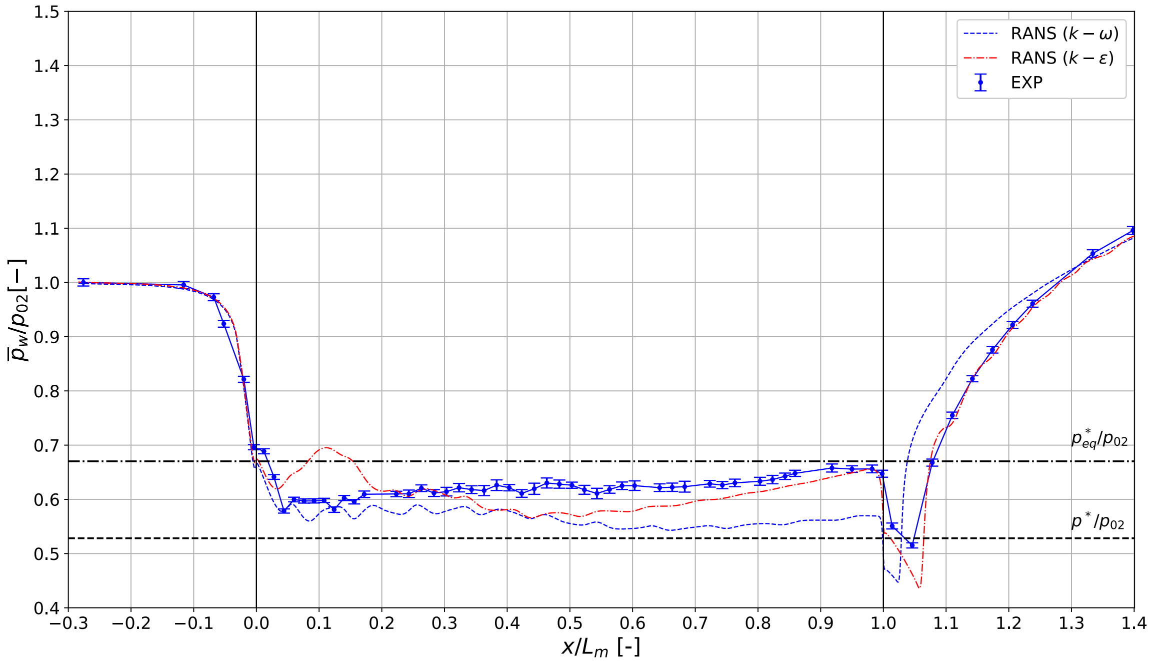

Figure 4.21: Comparison of the wall static pressure profile for $\frac{p_{01}}{p_{02}} = 5$ and $\frac{p_{0,out}}{p_{02}} = 1.2$, using experimental data and two different turbulence models in 2D RANS simulations.

4.5.2 Choking section position

Another notable feature that can be observed, as mentioned earlier, is the choking section. For a pressure profile at a specific outlet condition (i.e., $p_{0,out}/p_{02}$), the deviation from the curve compared to that of a lower outlet condition indicates that the secondary flow is no longer choked, allowing the pressure to rise through a shock train. This effect can also be visualized in the Mach number and pressure fields, with the flow being identical for two adjacent on-design conditions up to the a certain position, where the pressure suddenly increases. The flow is choked in that identical region. This is especially visible between Figure 4.20a and Figure 4.20b, where the first Fabri-patterns are identical.

As observed in the previous wall static pressure profiles (Figure 4.16 and Figure 4.18), the RANS simulations accurately predict the end of the double-choking regime in on-design conditions for both cases. Specifically, the pressure rise for the blue and yellow curves appears to separate at approximately the same location, although they both take slightly longer to rise experimentally compared to the simulations. To be more precise, the predicted separation between both curves is slightly delayed in the simulations compared to the experimental data for the case $p_{01}/p_{02} = 6$, while it is somewhat better predicted in the case $p_{01}/p_{02} = 4$.

Now, the green pressure profile of each case will be examined, which should correspond to the critical back-pressure of the experimental characteristic curve. The departure of this profile from the on-design profiles should occur at the very beginning of the mixing duct.

Regarding the case $p_{01}/p_{02} = 4$ in Figure 4.16, this behavior is well predicted by the simulations, with a departure at approximately $x/L_m \approx 0.05$. However, experimentally, the green curve seems to depart from the on-design profiles slightly earlier, just before the beginning of the mixing duct ($x/L_m \approx -0.004$). This suggests that this experimental profile is a bit off-design and that the real critical point may be slightly smaller. This observation is consistent with the characteristic curve in Figure 4.15, where the entrainment ratio starts decreasing at a slightly smaller $p_{0,out}/p_{02}$, around 1.46 or 1.47. It would be interesting in the future to measure the pressure profile of the actual critical back-pressure for this case.

Concerning the case $p_{01}/p_{02} = 6$ in Figure 4.18, it was more evident to distinguish the experimental critical back-pressure from the one estimated by the simulations. Therefore, the pressure profile was measured for both cases: the green curve, corresponding to $p_{0,out}/p_{02} = 2$, being the experimental critical back-pressure, and the red curve, representing $p_{0,out}/p_{02} = 2.05$, being the predicted critical back-pressure. The departure of the experimental green curve indeed occurs at the beginning of the mixing duct, around $x/L_m \approx 0.06$. The predicted profile at this back-pressure is clearly on-design, with a departure at $x/L_m \approx 0.21$. On the other hand, the experimental red curve clearly indicates an off-design condition with no choking of the secondary flow, as it separates from the other profile very early in the convergent section.

However, an interesting result emerges when examining the simulated profile of the red curve, corresponding to the estimated critical back-pressure. This simulated curve departs from the on-design profiles at nearly the same spot as the experimental green profile, corresponding to the experimental critical back-pressure ($x/L_m \approx 0.065$). This suggests that although the value of the critical back-pressure is not accurately predicted by the 2D RANS simulations, they can still capture the position of the critical choking section of the secondary flow quite well.

Additionally, as confirmed by the measured wall pressure, both the predictions and the experimental results indicate that there is no longer double-choking in the off-design regime. This is evident from the curves being directly detached from the on-design and critical cases.

4.5.3 Uncertainties on the pressure profiles

Another aspect worth discussing regarding these pressure profiles is their uncertainties. It appears that the uncertainties on the profile slightly increase with $p_{0,out}/p_{02}$. This is more visible with the case $p_{01}/p_{02} = 4$.

The higher uncertainty observed on the red and purple profiles in Figure 4.16 likely comes from the fact that these are highly off-design conditions. In such scenarios, the flow behavior becomes highly sensitive to the back-pressure. Consequently, even minor variations in the back-pressure between independent measurements can lead to significant fluctuations in the pressure profile, resulting in elevated uncertainties.

In Figure 4.18, the experimental pressure profile at the critical point (green curve) shows an increased uncertainty near the departure. It is expected, as this point is the shift between on- and off-design regimes. Small variations of the back-pressure between independent measurements can therefore lead to higher changes in the pressure profile.

4.6 Comparison between inlet and outlet flow rates

During the experimental campaign, the primary mass flow rate ($\dot{m}_1$), the secondary sucked mass flow rate ($\dot{m}_2$), and the total outlet mass flow rate ($\dot{m}_{out}$) were measured. This provides an opportunity to validate the mass flow rate measurements by comparing the sum of the inlet mass flow rates to the total mass flow rate.

It is important to note that the total mass flow rate could not be measured for some of the tests. One of the differential pressure transducers used to evaluate a mass flow rate started to malfunction during the last week of testing. Therefore, priority was given to measuring the inlet flow rates from that point, as no new pressure transducer could be found quickly enough. Consequently, some operating conditions are not present in this section. Moreover, the majority of the tests conducted at the conditions $p_{01}/p_{02} = 5$ and $p_{01}/p_{02} = 6$ were done without this total mass flow rate measurement. As a result, the outcomes presented for these two cases may be less certain.

$p_{0,out}/p_{02}$	$\dot{m}_1$	$\dot{m}_2$	$\dot{m}_1 + \dot{m}_2$	$\dot{m}_{out}$
1.11	0.262 ± 0.003	0.194 ± 0.002	0.456 ± 0.003	0.454 ± 0.004
1.30	0.263 ± 0.003	0.193 ± 0.002	0.457 ± 0.003	0.455 ± 0.004
1.46	0.264 ± 0.003	0.193 ± 0.002	0.457 ± 0.003	0.455 ± 0.004
1.47	0.264 ± 0.003	0.193 ± 0.002	0.457 ± 0.003	0.455 ± 0.004
1.48	0.264 ± 0.003	0.192 ± 0.002	0.456 ± 0.003	0.454 ± 0.004
1.50	0.264 ± 0.003	0.190 ± 0.002	0.454 ± 0.003	0.452 ± 0.004
1.51	0.264 ± 0.003	0.189 ± 0.002	0.453 ± 0.003	0.451 ± 0.004
1.52	0.265 ± 0.003	0.186 ± 0.002	0.451 ± 0.003	0.449 ± 0.004
1.56	0.267 ± 0.003	0.172 ± 0.002	0.439 ± 0.003	0.437 ± 0.004
1.60	0.270 ± 0.003	0.149 ± 0.002	0.418 ± 0.003	0.416 ± 0.004
1.70	0.278 ± 0.003	0.049 ± 0.001	0.327 ± 0.003	0.325 ± 0.003

Table 4.6: Mass flow rates obtained from experimental measurements for the case $p_{01}/p_{02} = 4$.

$p_{0,out}/p_{02}$	$\dot{m}_1$	$\dot{m}_2$	$\dot{m}_1 + \dot{m}_2$	$\dot{m}_{out}$
1.60	0.396 ± 0.003	0.164 ± 0.002	0.560 ± 0.003	0.558 ± 0.004
1.80	0.395 ± 0.003	0.164 ± 0.002	0.559 ± 0.004	0.557 ± 0.005
1.98	0.395 ± 0.003	0.163 ± 0.001	0.558 ± 0.003	0.556 ± 0.003
2.00	0.395 ± 0.003	0.163 ± 0.001	0.558 ± 0.003	0.556 ± 0.003
2.03	0.397 ± 0.003	0.159 ± 0.001	0.556 ± 0.003	0.554 ± 0.003
2.05	0.398 ± 0.003	0.152 ± 0.001	0.550 ± 0.003	0.548 ± 0.003
2.06	0.398 ± 0.003	0.147 ± 0.001	0.546 ± 0.003	0.543 ± 0.003
2.07	0.399 ± 0.003	0.143 ± 0.001	0.542 ± 0.003	0.540 ± 0.003
2.08	0.401 ± 0.003	0.138 ± 0.001	0.538 ± 0.003	0.536 ± 0.003
2.10	0.402 ± 0.003	0.123 ± 0.001	0.525 ± 0.003	0.523 ± 0.003
2.20	0.411 ± 0.003	0.032 ± 0.000	0.442 ± 0.003	0.438 ± 0.002

Table 4.7: Mass flow rates obtained from experimental measurements for the case $p_{01}/p_{02} = 6$.

The mass flow rates obtained for the cases $p_{01}/p_{02} = 4$ and $p_{01}/p_{02} = 6$ are presented in table Table 4.6 and table Table 4.7, respectively. The tables for the two other inlet pressure ratios are in Appendix C. Once again, those values do not take into account all of the performed experiments, but they give an idea of the order of magnitude and differences between the mass flow rates. To better visualize, the difference between the sum of the inlet mass flow rates and the total outlet mass flow rate measurements, i.e., $\Delta\dot{m} = \dot{m}_1 + \dot{m}_2 - \dot{m}_{out}$, is plotted for several operating conditions in Figure 4.22.

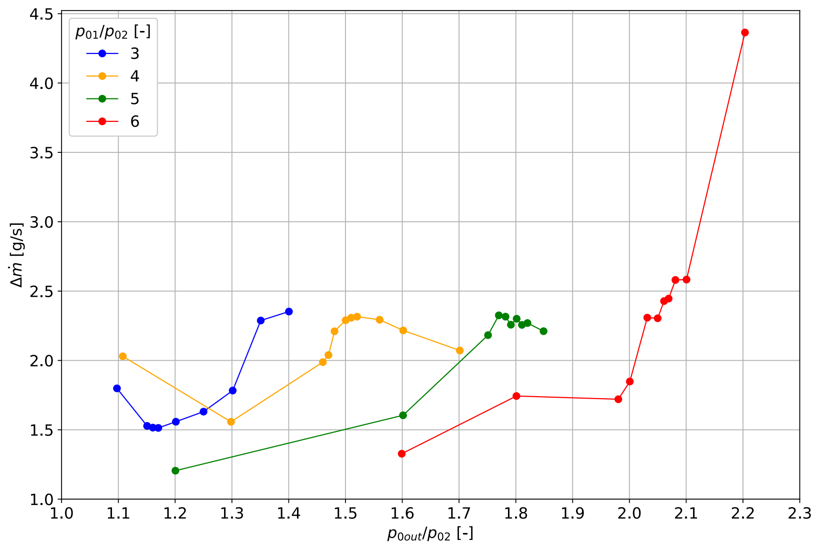

Figure 4.22: Difference between the sum of the inlet mass flow rates and the total outlet mass flow rate measurements.

For most cases, $\Delta\dot{m}$ is comprised between 1 and 2.5 [g/s], which is very small with respect to the value of the flow rates. However, there is an outlier for $p_{01}/p_{02} = 6$ and $p_{0,out}/p_{02} = 2.2$, where the difference is nearly 4.5 [g/s], although this is still quite small.

The most probable origin of this discrepancy would be leakages. Indeed, after the installation was operational, leakages were detected, mainly at the flanges. The flanges were tightened, and any apparent leak was corrected. However, there could still be some small leaks remaining here and there, especially in the outlet pipe, or even in the primary pipe, where some air could leave the pipes. Leakages could also come from the valves switching between the 64 pressure ports. Even though the most significant ones were detected and sealed, two valves remained untrustworthy due to remnant leakage. The values given at those two points were therefore removed, but tiny undetected leaks could still remain at other valves. All these small potential sources of leakage combined could account for the about 2 [g/s] of air leaving the system.

Chapter 5

Conclusion and perspectives

The main objective of this Master's thesis was to perform a complete testing campaign to gather experimental data, and provide reliable analyses by comparing the experiments with 2D RANS simulations. This manuscript also covered the final mechanical design that has been assembled throughout the year, with detailed explanations of the changes that were made to the initial design elaborated by G. Querinjean and N. Baguet [22]. Additionally, an in-depth presentation of uncertainties computation was provided, which have added relevance to the measured data.

Throughout the first semester, the assembly of the ejector took longer than expected. A few pieces had to be manufactured in-house, and all the parts were still to be mounted and sometimes welded together. However, this gave time to the authors to deepen their understanding on the subject by doing bibliographical researches, getting acquainted to the evaluation of uncertainties in measurements, already work on the acquisition system, and prepare the testing campaign for the following months.

Once the setup was finally operational, various tests were conducted under different operating conditions, and these were post-processed later on. Some interesting results came out of these analyses, and are summarized down below :

- The experimental on-design entrainment ratio was consistently lower than the 2D RANS simulations. However, the axisymmetric ejector design brought the simulations closer to the experimental data compared to the rectangular profile studied by Lamberts [21]. Actually, this was one of the main reason behind the conception of an axisymmetric design, as it reduces the impact of 3D effects, not captured by 2D simulations.

- The deviations that arise between the experimental data and the predicted ones, primarily come from the predicted secondary mass flow rate. These discrepancies probably have a few origins, such as the 3D effects not being considered, the real geometry not perfectly matching the one used in the CFD setup, and possibly the total pressure of the secondary stream not being uniform around the ejector shroud.

- The 2D RANS simulations predict a later critical back-pressure compared to what has been captured experimentally, with increasing differences at higher inlet pressure ratios. The origin of this discrepancy is mainly attributed to 3D effects and wall roughness.

- In on-design conditions, experimental wall static pressure profiles were higher than simulated ones within the mixing duct, while both profiles matched well in off-design conditions. This discrepancy is also attributed to 3D effects. The turbulence model also had an impact, with the $k - \epsilon$ RNG model performing better, but the latter is unable to predict realistic results in off-design conditions.

- Despite not accurately estimating the critical back-pressure, the simulations predicted the position of the choking section quite well. Specifically, the choking section of the critical point is located at the same place for both the experimental and estimated critical back-pressure.

- The compound-choking theory, compared to Fabri-choking theory, seems to be the most realistic one, even with operating conditions displaying a Fabri-like regime in the simulations. Indeed, the pressure profiles observed for the case $p_{01}/p_{02} = 6$ in on-design conditions barely cross the sonic pressure line, indicating a tiny Fabri-pattern. For a bit smaller p_{01}/p_{02}, the secondary flow would most likely not reach sonic conditions. Compound-choking must therefore happen at any on-design operating conditions in experiments.

Perspectives

Future studies may be conducted on this ejector, and the authors would like to give a few points worth exploring:

- As mentioned many times throughout the manuscript, a lot of differences seem to appear from 3D effects not being considered in the simulations. It may then be of interest to perform such simulations by incorporating those 3D particularities, as Lamberts did during his PhD thesis [22]. This would most probably reduce the deviations from the experimental results and hence better predict the behavior of this ejector.

- Expanding the testing campaign to include more inlet pressure ratios (e.g., 3.5, 4.5, 5.5, 5.39, 5.5, 6.5, and 7) and capturing additional pressure profiles, particularly around critical points, would provide a more comprehensive understanding of the behavior of the ejector.

- The overall experimental setup can be improved through some changes. Indeed, to get completely rid of leakage issues, the gaskets could be taken off, and the flanges be welded together instead. Regarding the ejector shroud, holes could be made on the bottom to take into account the possible non-uniformity of the pressure profile along the wall. An adaptor piece could also be realised to fit between the T-connection piece and the first piece of the ejector assembly in order to modify the NXP value. Finally, a section of the ejector shroud could be made transparent using Plexiglas or a similar material to visualize the phenomena occurring inside the mixing duct.

Appendix A

User manual

A.1 Description

This user manual concerns an axisymmetric supersonic air ejector. The assembly and use of this device are part of a thesis subject. The installation includes a primary circuit and a secondary circuit, a "T" piece to connect the two flows, a part called the "ejector", as well as a diffuser where the air is directed upward. The principle of this device is to send compressed air into the primary circuit, make it supersonic using a convergent-divergent, and drive the air from the secondary circuit to compress it in turn. The aim is therefore to observe the behaviors of the ejector under various inlet and outlet pressure conditions, in order to reveal different operating regimes.

Figure A.1: Picture of the complete installation

Responsible person

Yann Bartosiewicz (yann.bartosiewicz@uclouvain.be)

A.2 Training

No specific training is required to operate the ejector.

A.3 Risks

The sound level emitted by the compressor and ejector is high. Therefore, it is required to wear ear protection when using the ejector. Additionally, the wall containing the 64 pressure ports can become cold (close to 0 [°C]). It is advisable not to touch it when the ejector is in operation.

A.4 Startup procedure

1. Start the compressor (refer to its user manual or to the responsible persons for instructions).
2. Turn on the power of the electrical box and both power strips.
3. Connect the PC to the Ethernet cable and the USB cable for data acquisition and compressor control.
4. On the PC, launch the LabView instance (VISEJEC.llb) in the "VISEJEC 2" folder.
5. In the window that opens, launch "visu-complet.vi" and ensure that the compressor pressure ("Motive pressure") is set to 0 bar (see red box in Figure A.2).
6. Enter the values for relative humidity, ambient pressure, and ambient temperature (see green box in Figure A.2). These values can be determined using a measurement device in the room or by taking readings from the ejector's various sensors when the motive pressure is at 0 bar.
7. Launch "VISEJEC.vi" and click on the "Run" arrow at the top left of the window to start data acquisition.
8. Gradually increase the compressor pressure ("Motive pressure") to the desired value.

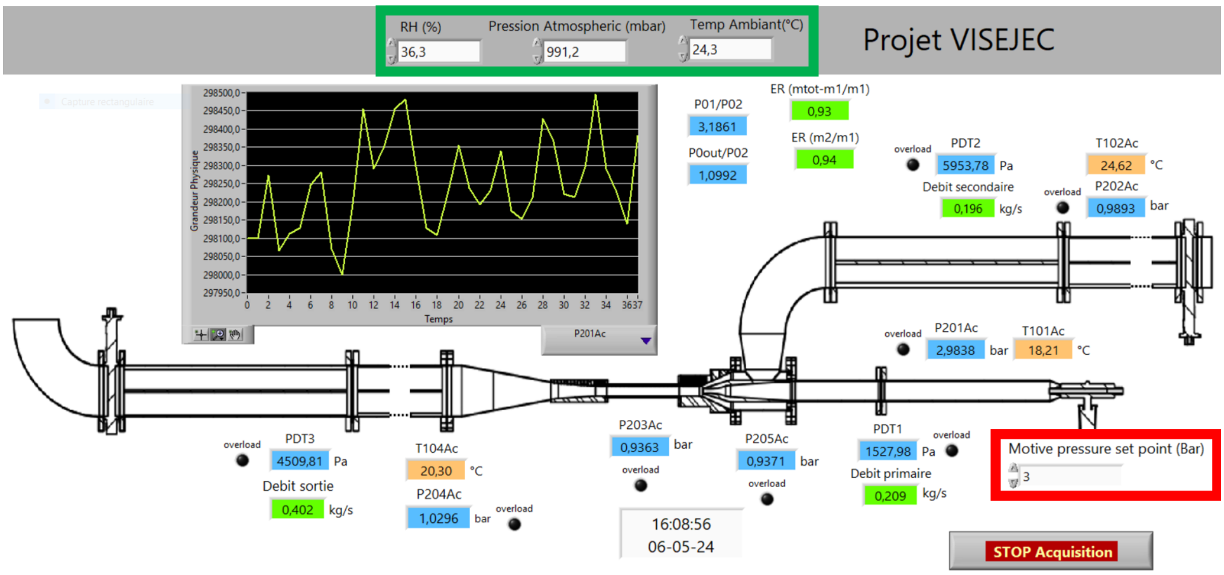

Figure A.2: LabView interface

The pressure scanners allow for the sequential opening of all 64 pressure ports, and the measurement is displayed as *P203Ac*. Switching from one pressure port to another can be done automatically ("PLC séquence"), as shown in Figure A.3, or manually ("PLC manuel") by changing the "Mode multiplexeur". The time spent on each point can be adjusted in the sequence mode ("Interval de temps").

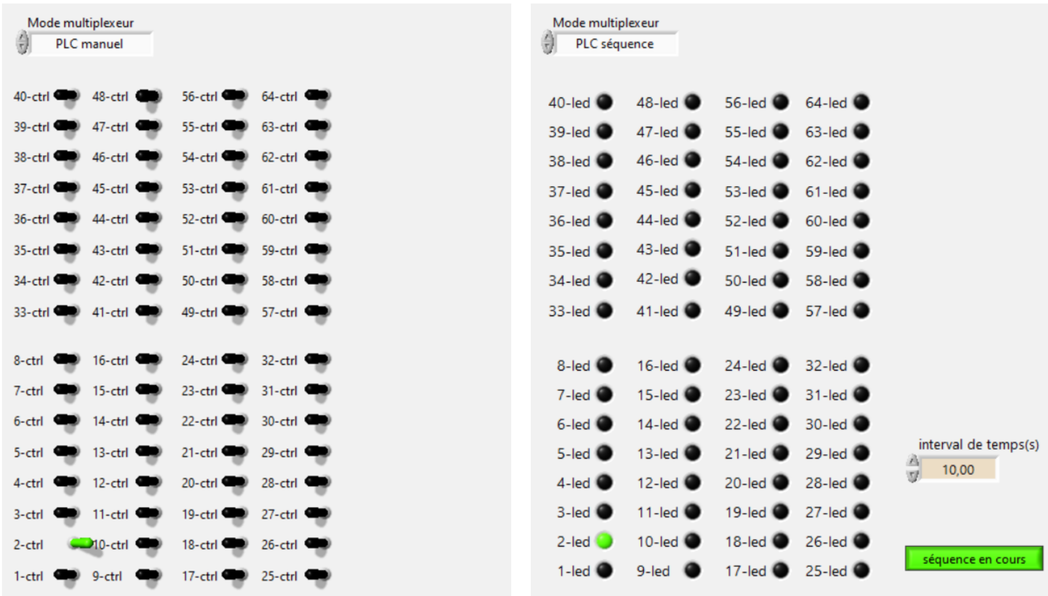

(a) Manual mode (b) Automatic mode

Figure A.3: LabView interface for the operation of the 64 valves

Once the ejector is started, it is possible to modify the inlet conditions of the secondary circuit or the outlet conditions using butterfly valves.

A.5 Shutdown procedure

1. In the LabView instance, set the compressor pressure ("Motive pressure") to 0 bar and stop the data acquisition.

2. Turn off the compressor (refer to its user manual or to the responsible persons for instructions).

3. Disconnect the Ethernet cable and USB cable from the PC.

4. Turn off both power strips and the power of the electrical box.

Appendix B

Acquisition system

B.1 DAQ

The DAQ is the data acquisition file which contains all necessary information about the sensors. This includes their name, description, desired range, actual range, location on the installation and reference. Those information are displayed on Table B.2.

On top of that, the DAQ also contains information about the sensors cabling (to which channel they are connected and the corresponding resistance) and the linear relationships to convert the voltage returned by the sensors into physical quantities (coefficient A, B and C of Ax^2+Bx+C). The coefficients of the relationships were not determined using minimum and maximum tension and physical quantities, but through a calibration procedure. Those values are reported in Table B.1.

DAQ USB-6341									
AI									
Canal	**ohms**	Val. Phys. Min	Tension Min	Val. Phys. Max	Tension Max	A	B	C	Unité
AI0	**499,13271**	0	1,9965	1000000	9,9827	0	125560,0000	-252960,0000	Pa
AI1	**499,00512**	0	1,9960	50	9,9801	0	6,2625	-12,5000	°C
AI2	**498,94517**	0	1,9958	10000	9,9789	0	1252,6000	-2528,5000	Pa
AI3	**499,00451**	0	1,9960	0	9,9801	0	0,0000	0,0000	
AI4	**498,94082**	0	1,9958	50	9,9788	0	6,2633	-12,5000	°C
AI5	**499,03793**	0	1,9962	160000	9,9808	0	19953,0000	-39117,0000	Pa
AI6	**498,94183**	0	1,9958	10000	9,9788	0	1253,2000	2485,2000	Pa
AI7	**498,95263**	0	1,9958	160000	9,9791	0	20041,0000	-40180,0000	Pa
AI8	**498,97676**	0	1,9959	0	9,9795	0	0,0000	0,0000	
AI9	**498,98382**	0	1,9959	0	9,9797	0	0,0000	0,0000	
AI10	**498,85240**	0	1,9954	1000000	9,9770	0	125562,0000	-245900,0000	Pa
AI11	**499,30309**	0	1,9972	50	9,9861	0	6,2587	-12,5000	°C
AI12	**498,88652**	0	1,9955	1000000	9,9777	0	75226,0000	-49982,0000	Pa
AI13	**498,91095**	0	1,9956	50000	9,9782	0	6242,6000	-12439,0000	Pa
AI14	**498,95263**	0	1,9958	0	9,9791	0	0,0000	0,0000	
AI15	**499,15501**	0	1,9966	0	9,9831	0	0,0000	0,0000	

Table B.1: DAQ file of the sensors (Part 2)

DAQ USB-6341								
AI								
Nom	Description	Gamme souhaitée	Gamme capteur	Unité	Emplacement	Instrument	Instrument Reference	Canal
P201Ac	Pression relative	3-7	0-10	bar	Circuit primaire - Amont diaph.	Kistler RAG25R10BC1H	SN1802909	**AI0**
T101Ac	Température sonde PT100	0-40	0-100	°C	Circuit primaire - Amont diaph.	Thermibel élément Pt 100 CI.A	T57694/1,1	**AI1**
PDT1	Pression différentielle au diaphragme	+-0,1	+-0,1	bar	Circuit primaire	E.H. PMD75- ACA7D212AAU	D705570109D	**AI2**
								AI3
T102Ac	Température sonde PT100	15-25	0-100	°C	Circuit secondaire - Amont diaph.	Thermibel élément Pt 100 CI.A	T57694/1,4	**AI4**
P202Ac	Pression absolue	0-1,2	0-1,6	bar	Circuit secondaire - Amont diaph.	E.H. PMP131-A1111A2H	D715B401052	**AI5**
PDT2	Pression différentielle au diaphragme	+-0,1	+-0,1	bar	Circuit secondaire	E.H. PMD75-ACA7D212AAU	D5071F0109D	**AI6**
P205Ac	Pression absolue	0-1,2	0-1,6	bar	Circuit secondaire - T	E.H. PMP131-A1111A2H	D715B601052	**AI7**
								AI8
								AI9
P203Ac	Pression absolue	0,4-2,5	0-10	bar	Ejecteur - 64 prises de pression	Druck PTX 1400	R01542/15	**AI10**
T104Ac	Température Couple K	0-40	0-650	°C	Aval éjecteur	Thermibel Couple K	T32893/1,10	**AI11**
P204Ac	Pression absolue	0,8-2,4	0-10	bar	Aval éjecteur	E+H PMP21-AA1U2PJWBJ	S704CA0116A	**AI12**
PDT3	Pression différentielle au diaphragme	+-0,5	+-0,5	bar	Aval éjecteur	E.H. PMD75-ACA7F212AAU	8207350109D	**AI13**
								AI14
								AI15

Table B.2: DAQ file of the sensors (Part 1)

B.2 Calibration data

The calibration procedure is detailed in this section. It includes a table for each pressure sensor, listing the measured voltage for each tested relative pressure, which corresponds to a specific weight applied to the calibration device. For absolute pressure sensors, this relative pressure is added to the current atmospheric pressure. These data points were then plotted, and their linear regression lines were obtained, as shown in Figure B.1 and Figure B.2. The calibration of the temperature sensors, however, was performed by a CREDEM technician, not by the authors.

P201Ac	
tension (V)	***relative pressure (bar)***
2,0955	0,1
2,8909	1,1
3,6877	2,1
4,4855	3,1
5,2774	4,1
6,0745	5,1
6,871	6,1
7,6675	7,1
8,469	8,1
9,2635	9,1

Table B.3: Calibration data - P201Ac

P202Ac		
tension (V)	***relative pressure (bar)***	***absolute pressure (bar)***
7,506	0,1	1,1063
8,004	0,2	1,2063
8,5063	0,3	1,3063
9,0116	0,4	1,4063
9,50925	0,5	1,5063
10,01	0,6	1,6063

Table B.4: Calibration data - P202Ac

P203Ac		
tension (V)	***relative pressure (bar)***	***absolute pressure (bar)***
2,8439	0,1	1,1062
3,6351	1,1	2,1062
4,4305	2,1	3,1062
5,2269	3,1	4,1062
6,0236	4,1	5,1062
6,8203	5,1	6,1062
7,6173	6,1	7,1062
8,4145	7,1	8,1062
9,2115	8,1	9,1062
10,009	9,1	10,1062

Table B.5: Calibration data - P203Ac

P204Ac		
tension (V)	***relative pressure (bar)***	***absolute pressure (bar)***
2,1089	0,1	1,0859
3,4372	1,1	2,0859
4,7656	2,1	3,0859
6,0955	3,1	4,0859
7,425	4,1	5,0859
8,755	5,1	6,0859
10,0843	6,1	7,0859

Table B.6: Calibration data - P204Ac

P205Ac		
tension (V)	***relative pressure (bar)***	***absolute pressure (bar)***
7,4785	0,1	1,0957
7,967	0,2	1,1957
8,4666	0,3	1,2957
8,9676	0,4	1,3957
9,468	0,5	1,4957
9,9705	0,6	1,5957

Table B.7: Calibration data - P205Ac

PDT1		PDT2		PDT3	
tension (V)	*differential pressure (Pa)*	*tension (V)*	*differential pressure (Pa)*	*tension (V)*	*differential pressure (Pa)*
2,016	0	1,9885	0	1,9925	0
4,018	2500	3,972	2500	2,3931	2500
4,813	3500	4,7745	3500	2,5532	3500
5,6107	4500	5,5738	4500	2,7133	4500
6,4094	5500	6,3718	5500	2,8738	5500
7,2078	6500	7,1705	6500	3,0339	6500
8,0053	7500	7,968	7500	3,1938	7500
8,8038	8500	8,7668	8500	3,3541	8500
9,6027	9500	9,565	9500	3,5145	9500
				3,6745	10500
				3,8348	11500
				3,9948	12500
				4,1552	13500

Table B.8: Calibration data - PDT1, PDT2 and PDT3

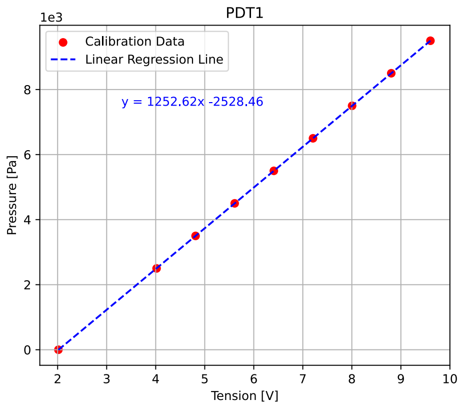

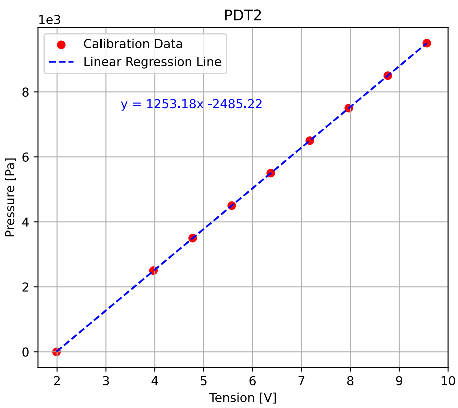

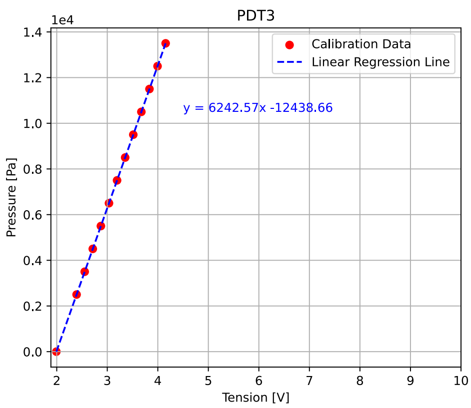

Figure B.1: Linear relationships for PDT1, PDT2 and PDT3

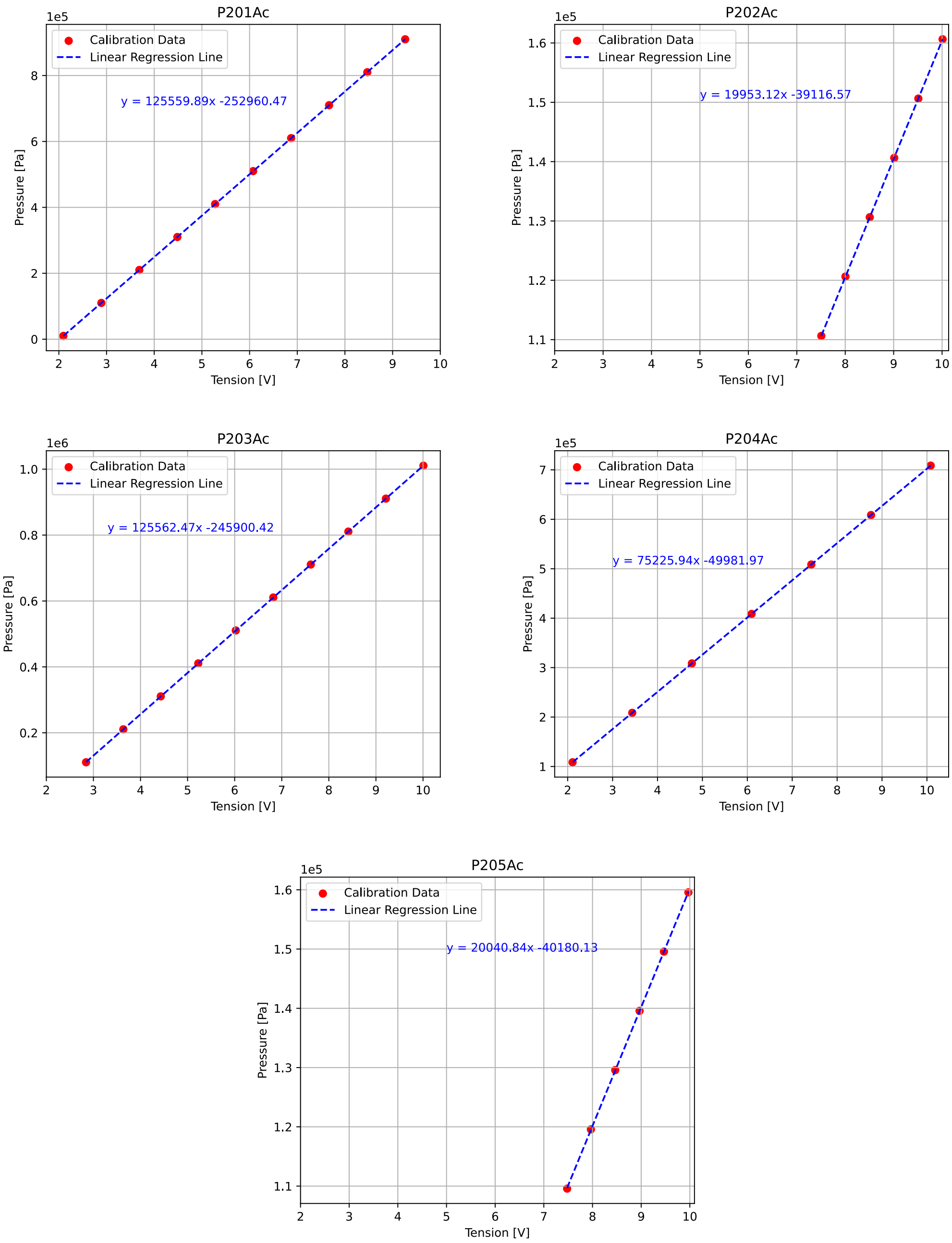

Figure B.2: Linear relationships for P201Ac, P202Ac, P203Ac, P204Ac and P205Ac

Appendix C

Detailed results

C.1 Entrainment ratios

The entrainment ratios obtained from experimental data and from the 2D RANS simulations are presented here for every operating conditions. The deviation of the simulated ER from the experimental value is also indicated.

p_{01}/p_{02}	$p_{0,out}/p_{02}$	ER (EXP)	ER (RANS)	Deviation [%]
3	1.10	1.002 ± 0.011	1.048	+4.61
	1.15	0.999 ± 0.012	1.046	+4.66
	1.16	0.998 ± 0.012	1.044	+4.67
	1.17	0.997 ± 0.012	1.043	+4.66
	1.20	0.993 ± 0.012	1.038	+4.57
	1.25	0.971 ± 0.012	1.024	+5.48
	1.30	0.917 ± 0.011	0.990	+8.00
	1.35	0.756 ± 0.008	0.888	+17.47
	1.40	0.505 ± 0.007	0.614	+21.58
	1.45	0.268 ± 0.003	0.310	+15.65
4	1.11	0.737 ± 0.009	0.758	+2.91
	1.30	0.733 ± 0.009	0.757	+3.17
	1.46	0.732 ± 0.009	0.756	+3.24
	1.47	0.731 ± 0.009	0.756	+3.36
	1.48	0.730 ± 0.009	0.756	+3.51
	1.50	0.722 ± 0.009	0.754	+4.40
	1.51	0.715 ± 0.009	0.752	+5.19
	1.52	0.705 ± 0.009	0.749	+6.21
	1.56	0.648 ± 0.008	0.719	+11.04
	1.60	0.552 ± 0.007	0.614	+11.31
	1.70	0.178 ± 0.003	0.194	+8.78
5	1.20	0.546 ± 0.006	0.567	+3.97
	1.60	0.545 ± 0.006	0.566	+3.99
	1.75	0.544 ± 0.006	0.566	+4.16
	1.77	0.534 ± 0.006	0.567	+6.08
	1.78	0.524 ± 0.006	0.567	+8.21
	1.79	0.514 ± 0.005	0.567	+10.30
	1.80	0.501 ± 0.005	0.562	+12.22
	1.81	0.486 ± 0.005	0.552	+13.55
	1.82	0.468 ± 0.005	0.537	+14.53
	1.85	0.403 ± 0.008	0.449	+11.36
	1.95	0.116 ± 0.002	0.135	+16.28
6	1.60	0.411 ± 0.005	0.430	+4.51
	1.80	0.412 ± 0.004	0.431	+4.71
	1.98	0.411 ± 0.004	0.431	+4.85
	2.00	0.411 ± 0.004	0.431	+4.88
	2.01	0.409 ± 0.004	0.431	+5.32
	2.03	0.396 ± 0.005	0.431	+8.63
	2.05	0.377 ± 0.004	0.430	+14.16
	2.06	0.367 ± 0.004	0.430	+17.08
	2.07	0.355 ± 0.004	0.417	+17.48
	2.08	0.340 ± 0.004	0.392	+15.33
	2.10	0.303 ± 0.004	0.335	+10.55
	2.20	0.075 ± 0.002	0.098	+30.77

Table C.1: Values of the experimental and simulated entrainment ratio at every operating condition.

C.2 Mass flow rates

The primary and secondary mass flow rates obtained from experimental data and from the 2D RANS simulations are presented here for every operating conditions, in Table C.2 and Table C.3. The deviation of the simulated $\dot{m}_1$ and $\dot{m}_2$ from the experimental value is also indicated.

Additionally, the mass flow rates evolution with $p_{0,out}/p_{02}$ for the cases p_{01}/p_{02} = 3 and 4 are presented in Figure C.1 and Figure C.2, respectively.

The measured mass flow rates at the primary inlet, secondary inlet, and at the outlet for the inlet pressure ratios of 3 and 5 are also indicated in Table C.4 and Table C.5.

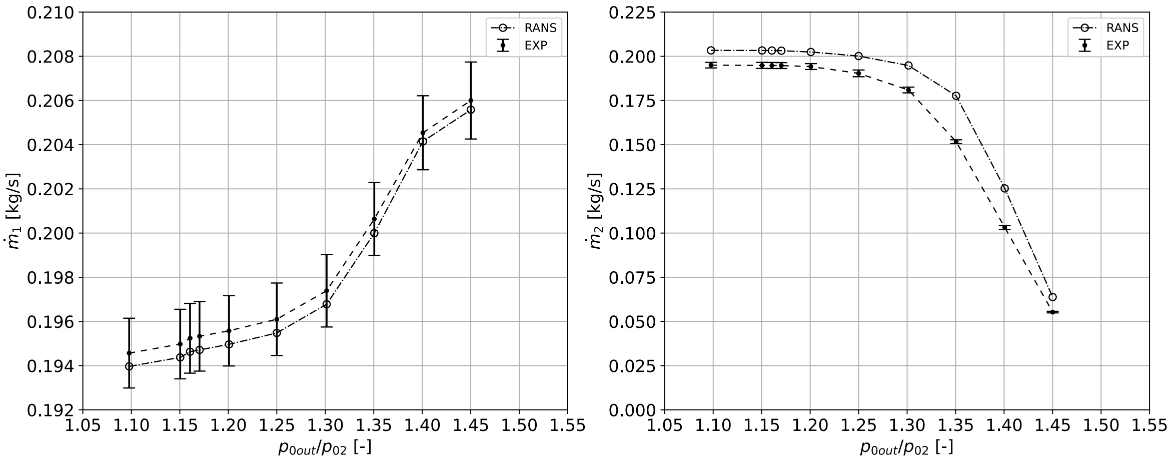

Figure C.1: Inlet mass flow rates for $\frac{p_{01}}{p_{02}} = 3$.

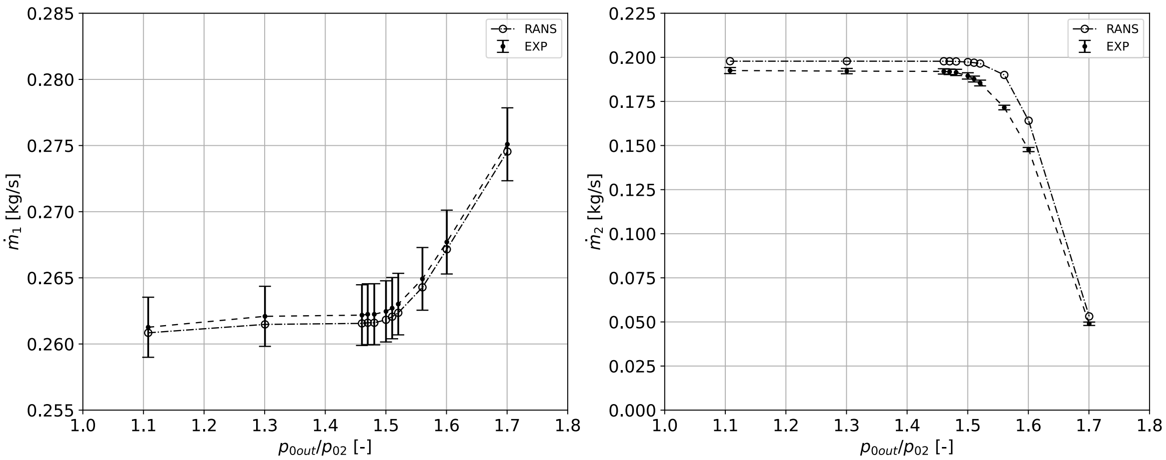

Figure C.2: Inlet mass flow rates for $\frac{p_{01}}{p_{02}} = 4$.

p_{01}/p_{02}	$p_{0,out}/p_{02}$	$\dot{m}_1$ (EXP) [kg/s]	$\dot{m}_1$ (RANS) [kg/s]	Deviation [%]
3	1.10	0.195 ± 0.002	0.194	-0.31
	1.15	0.195 ± 0.002	0.194	-0.31
	1.16	0.195 ± 0.002	0.195	-0.31
	1.17	0.195 ± 0.002	0.195	-0.32
	1.20	0.196 ± 0.002	0.195	-0.31
	1.25	0.196 ± 0.002	0.195	-0.32
	1.30	0.197 ± 0.002	0.197	-0.31
	1.35	0.201 ± 0.002	0.200	-0.32
	1.40	0.205 ± 0.002	0.204	-0.19
	1.45	0.206 ± 0.002	0.206	-0.20
4	1.11	0.261 ± 0.002	0.261	-0.16
	1.30	0.262 ± 0.002	0.261	-0.23
	1.46	0.262 ± 0.002	0.262	-0.24
	1.47	0.262 ± 0.002	0.262	-0.24
	1.48	0.262 ± 0.002	0.262	-0.24
	1.50	0.262 ± 0.002	0.262	-0.24
	1.51	0.263 ± 0.002	0.262	-0.25
	1.52	0.263 ± 0.002	0.262	-0.25
	1.56	0.265 ± 0.002	0.264	-0.24
	1.60	0.268 ± 0.002	0.267	-0.20
	1.70	0.275 ± 0.003	0.275	-0.20
5	1.20	0.328 ± 0.003	0.328	-0.04
	1.60	0.328 ± 0.003	0.328	-0.05
	1.75	0.328 ± 0.003	0.328	-0.05
	1.77	0.329 ± 0.003	0.329	-0.03
	1.78	0.330 ± 0.003	0.330	-0.03
	1.79	0.330 ± 0.003	0.330	-0.05
	1.80	0.331 ± 0.003	0.331	-0.05
	1.81	0.331 ± 0.003	0.331	-0.06
	1.82	0.332 ± 0.003	0.332	-0.05
	1.85	0.335 ± 0.003	0.335	-0.06
	1.95	0.344 ± 0.003	0.343	-0.07
6	1.60	0.397 ± 0.003	0.397	+0.002
	1.80	0.396 ± 0.003	0.396	+0.03
	1.98	0.396 ± 0.003	0.396	-0.07
	2.00	0.396 ± 0.003	0.396	-0.05
	2.01	0.396 ± 0.003	0.396	-0.07
	2.03	0.397 ± 0.003	0.397	+0.04
	2.05	0.398 ± 0.003	0.398	+0.04
	2.06	0.398 ± 0.003	0.398	+0.04
	2.07	0.399 ± 0.003	0.399	+0.04
	2.08	0.400 ± 0.003	0.400	+0.03
	2.10	0.402 ± 0.003	0.402	+0.04
	2.20	0.410 ± 0.003	0.410	+0.02

Table C.2: Values of the experimental and simulated primary mass flow rate at every operating condition.

p_{01}/p_{02}	$p_{0,out}/p_{02}$	$\dot{m}_2$ (EXP) [kg/s]	$\dot{m}_2$ (RANS) [kg/s]	Deviation [%]
3	1.10	0.195 ± 0.002	0.203	+4.29
	1.15	0.195 ± 0.002	0.203	+4.34
	1.16	0.195 ± 0.002	0.203	+4.35
	1.17	0.195 ± 0.002	0.203	+4.33
	1.20	0.194 ± 0.002	0.202	+4.24
	1.25	0.190 ± 0.002	0.200	+5.14
	1.30	0.181 ± 0.002	0.195	+7.66
	1.35	0.152 ± 0.001	0.178	+17.10
	1.40	0.103 ± 0.001	0.125	+21.35
	1.45	0.0553 ± 0.0004	0.064	+15.41
4	1.11	0.193 ± 0.002	0.198	+2.75
	1.30	0.192 ± 0.002	0.198	+2.93
	1.46	0.192 ± 0.002	0.198	+3.00
	1.47	0.192 ± 0.002	0.198	+3.10
	1.48	0.191 ± 0.002	0.198	+3.25
	1.50	0.189 ± 0.002	0.197	+4.15
	1.51	0.188 ± 0.002	0.197	+4.94
	1.52	0.185 ± 0.002	0.196	+5.94
	1.56	0.172 ± 0.001	0.190	+10.77
	1.60	0.148 ± 0.001	0.164	+11.09
	1.70	0.049 ± 0.001	0.053	+8.56
5	1.20	0.179 ± 0.001	0.186	+3.93
	1.60	0.179 ± 0.001	0.186	+3.94
	1.75	0.178 ± 0.001	0.186	+4.10
	1.77	0.176 ± 0.001	0.187	+6.05
	1.78	0.173 ± 0.001	0.187	+8.18
	1.79	0.170 ± 0.001	0.187	+10.25
	1.80	0.166 ± 0.001	0.186	+12.17
	1.81	0.161 ± 0.001	0.183	+13.49
	1.82	0.156 ± 0.001	0.178	+14.47
	1.85	0.135 ± 0.003	0.150	+11.30
	1.95	0.040 ± 0.001	0.046	+16.19
6	1.60	0.163 ± 0.001	0.171	+4.51
	1.80	0.163 ± 0.001	0.171	+4.74
	1.98	0.163 ± 0.001	0.171	+4.78
	2.00	0.163 ± 0.001	0.171	+4.83
	2.01	0.162 ± 0.001	0.171	+5.24
	2.03	0.157 ± 0.001	0.171	+8.67
	2.05	0.150 ± 0.001	0.171	+14.21
	2.06	0.146 ± 0.001	0.171	+17.12
	2.07	0.141 ± 0.001	0.166	+17.52
	2.08	0.136 ± 0.001	0.157	+15.37
	2.10	0.122 ± 0.001	0.134	+10.59
	2.20	0.031 ± 0.001	0.040	+30.79

Table C.3: Values of the experimental and simulated secondary mass flow rate at every operating condition.

$p_{0,out}/p_{02}$	$\dot{m}_1$	$\dot{m}_2$	$\dot{m}_1 + \dot{m}_2$	$\dot{m}_{out}$
1.10	0.196 ± 0.002	0.196 ± 0.002	0.392 ± 0.003	0.39 ± 0.004
1.15	0.196 ± 0.002	0.196 ± 0.002	0.392 ± 0.003	0.391 ± 0.004
1.16	0.196 ± 0.002	0.196 ± 0.002	0.392 ± 0.003	0.391 ± 0.004
1.17	0.196 ± 0.002	0.196 ± 0.002	0.392 ± 0.003	0.391 ± 0.004
1.20	0.197 ± 0.002	0.195 ± 0.002	0.392 ± 0.003	0.39 ± 0.004
1.25	0.197 ± 0.002	0.191 ± 0.002	0.388 ± 0.003	0.387 ± 0.004
1.30	0.198 ± 0.002	0.182 ± 0.002	0.380 ± 0.003	0.379 ± 0.004
1.35	0.201 ± 0.002	0.152 ± 0.001	0.352 ± 0.002	0.35 ± 0.002
1.40	0.205 ± 0.002	0.104 ± 0.001	0.308 ± 0.002	0.306 ± 0.002

Table C.4: Mass flow rates obtained from experimental measurements for the case $p_{01}/p_{02} = 3$.

$p_{0,out}/p_{02}$	$\dot{m}_1$	$\dot{m}_2$	$\dot{m}_1 + \dot{m}_2$	$\dot{m}_{out}$
1.20	0.328 ± 0.003	0.179 ± 0.002	0.508 ± 0.003	0.506 ± 0.003
1.60	0.328 ± 0.003	0.179 ± 0.002	0.507 ± 0.003	0.506 ± 0.003
1.75	0.328 ± 0.003	0.179 ± 0.002	0.507 ± 0.003	0.505 ± 0.003
1.77	0.328 ± 0.003	0.177 ± 0.001	0.505 ± 0.003	0.502 ± 0.003
1.78	0.328 ± 0.003	0.173 ± 0.001	0.502 ± 0.003	0.500 ± 0.003
1.79	0.329 ± 0.003	0.170 ± 0.001	0.499 ± 0.003	0.496 ± 0.003
1.80	0.330 ± 0.003	0.166 ± 0.001	0.496 ± 0.003	0.493 ± 0.003
1.81	0.330 ± 0.003	0.161 ± 0.001	0.491 ± 0.003	0.489 ± 0.003
1.82	0.331 ± 0.003	0.156 ± 0.001	0.487 ± 0.003	0.485 ± 0.003
1.85	0.334 ± 0.003	0.136 ± 0.021	0.470 ± 0.010	0.468 ± 0.009

Table C.5: Mass flow rates obtained from experimental measurements for the case $p_{01}/p_{02} = 5$.

C.3 Pressure profiles

The remaining pressure profiles for the cases $p_{01}/p_{02} = 3$ and $p_{01}/p_{02} = 5$ are shown in this section, with the corresponding operating conditions circled with the corresponding colors on their characteristic curve.

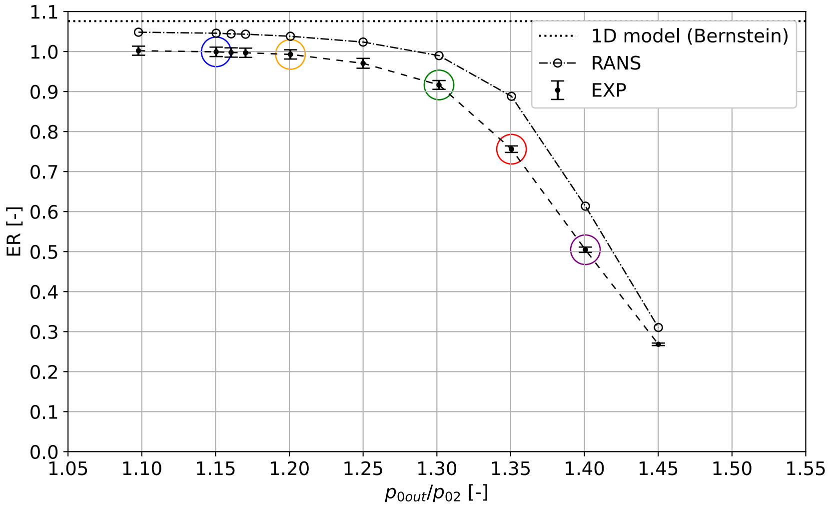

Figure C.3: Characteristic curve for $\frac{p_{01}}{p_{02}} = 3$.

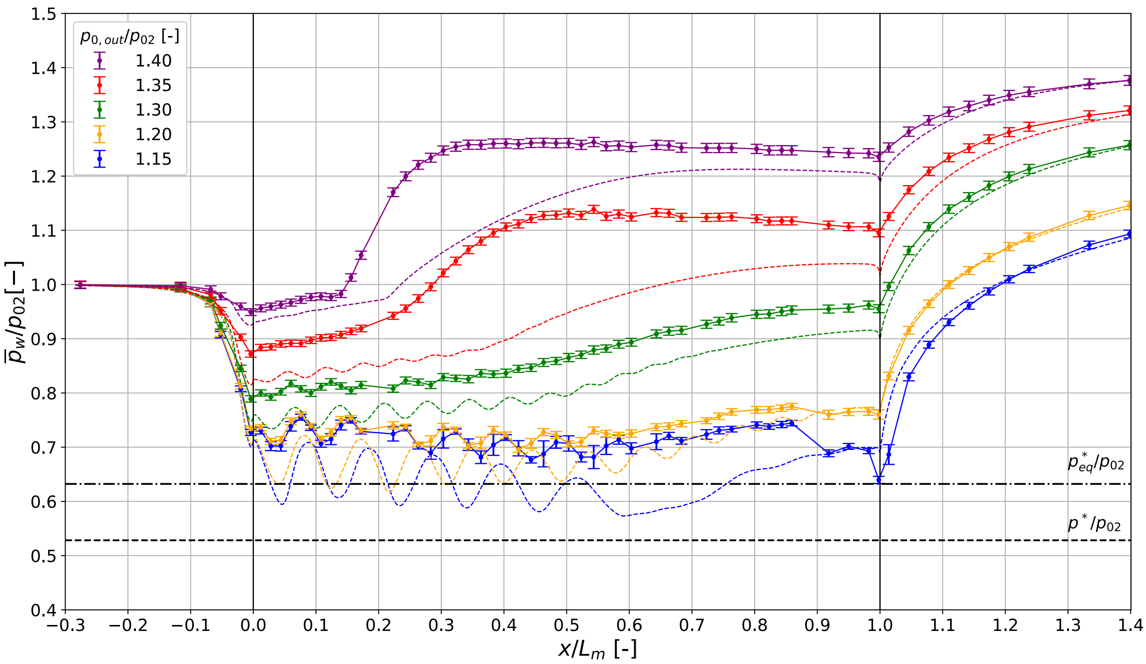

Figure C.4: Wall static pressure profiles for $\frac{p_{01}}{p_{02}} = 3$.

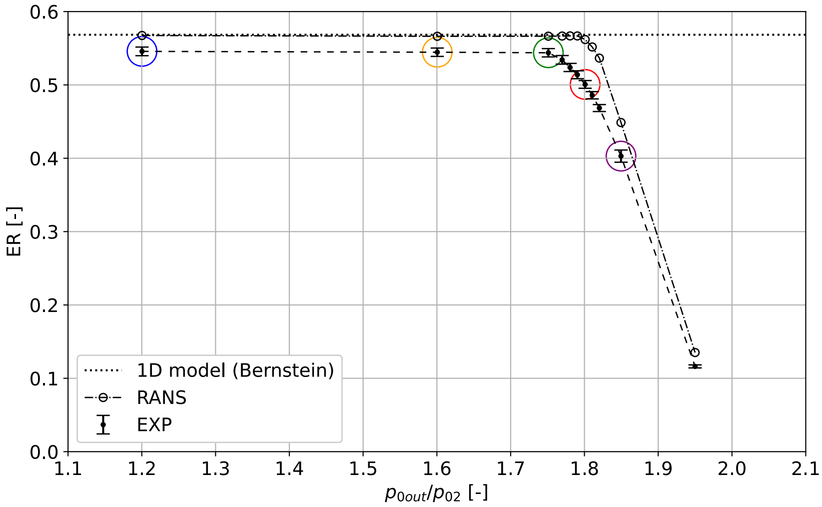

Figure C.5: Characteristic curve for $\frac{p_{01}}{p_{02}} = 5$.

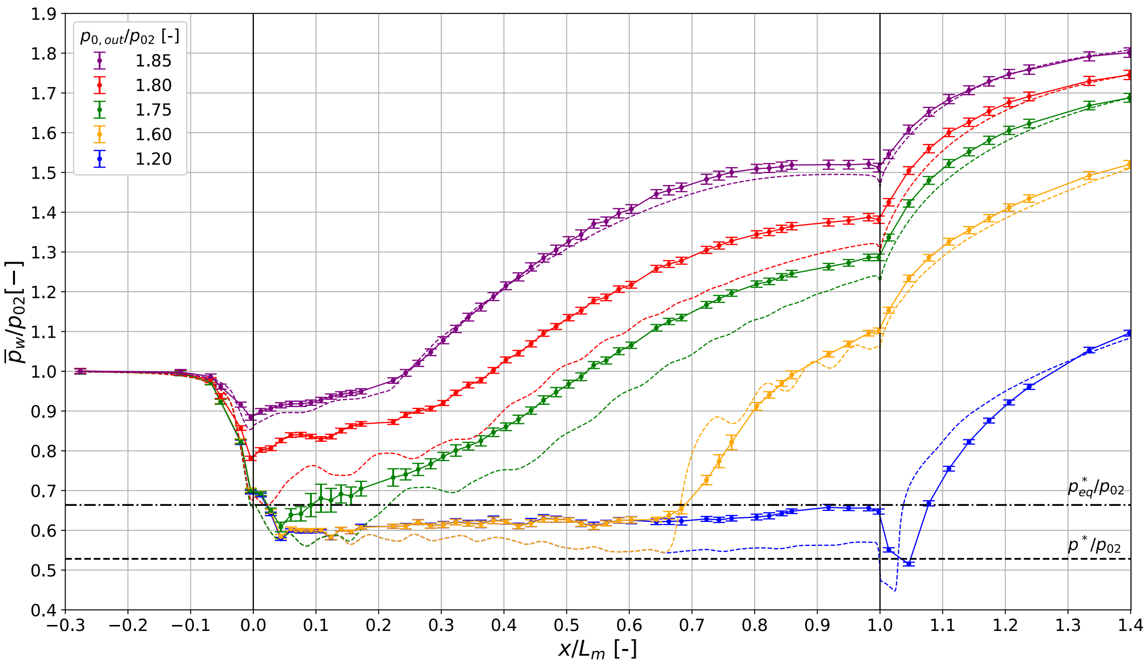

Figure C.6: Wall static pressure profiles for $\frac{p_{01}}{p_{02}} = 5$.

For a clearer and more distinct view of each pressure profile, they are displayed individually for each operating condition.

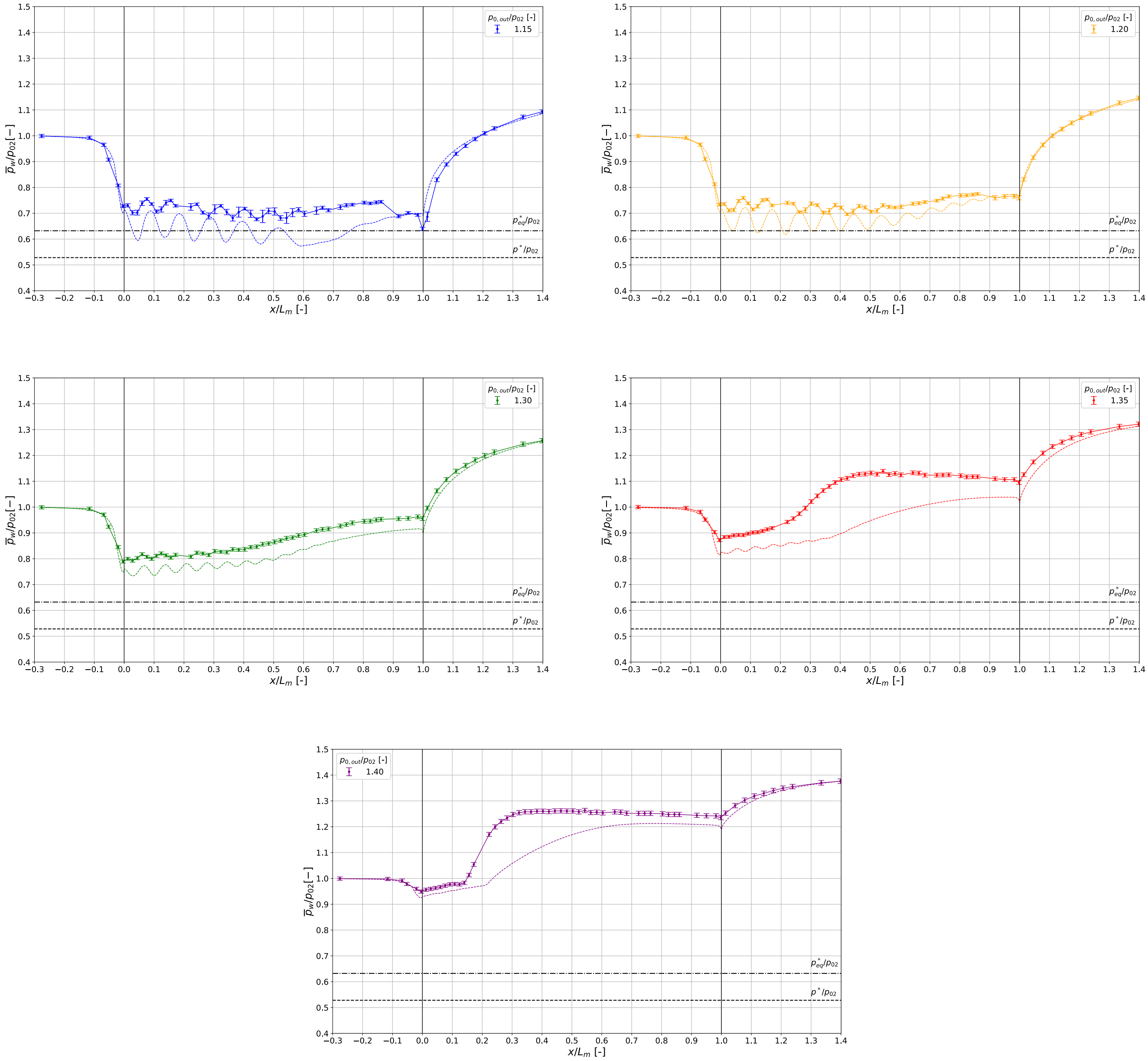

Figure C.7: Pressure profiles for the case $p_{01}/p_{02} = 3$, for each measured outlet condition.

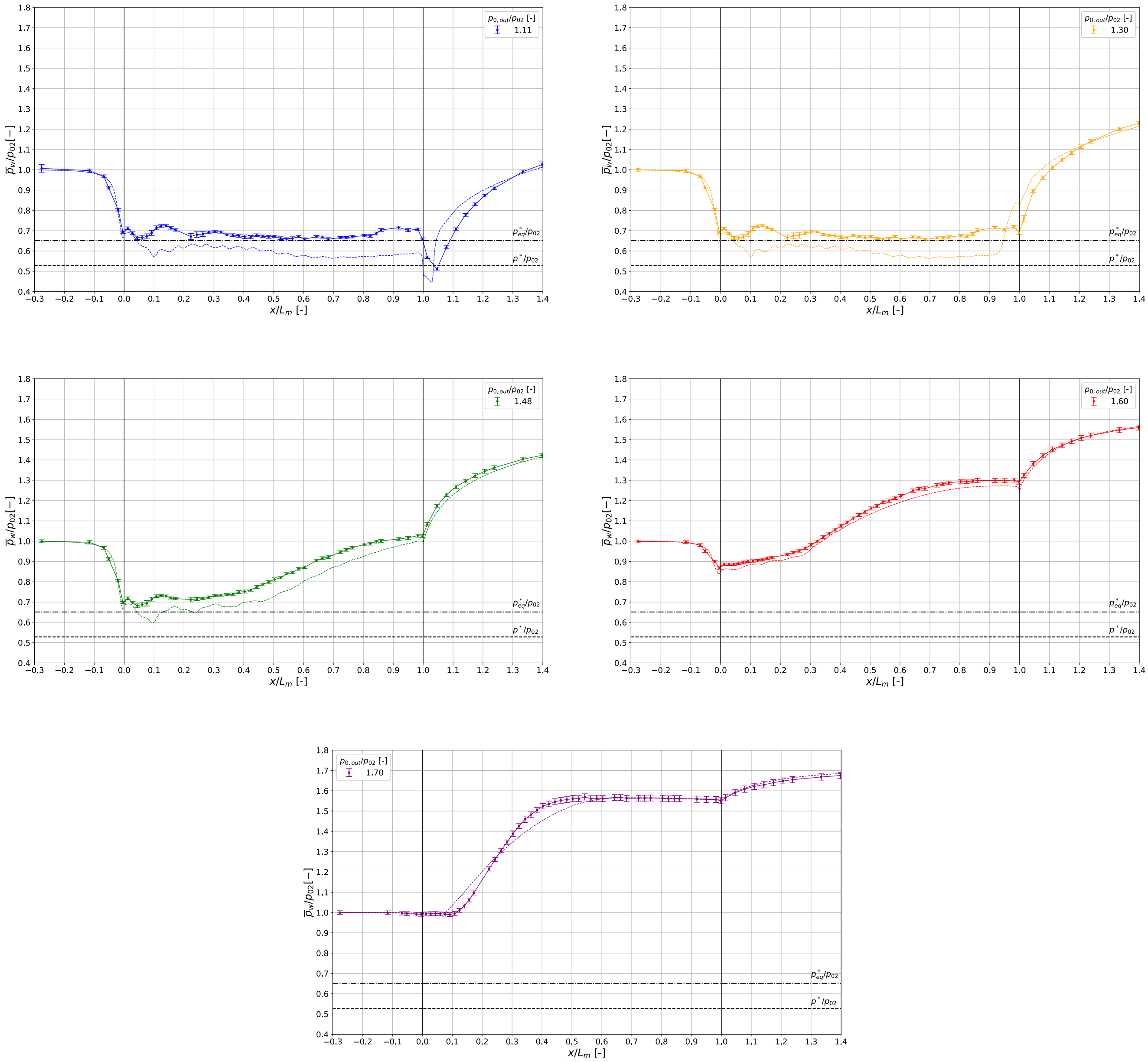

Figure C.8: Pressure profiles for the case $p_{01}/p_{02} = 4$, for each measured outlet condition.

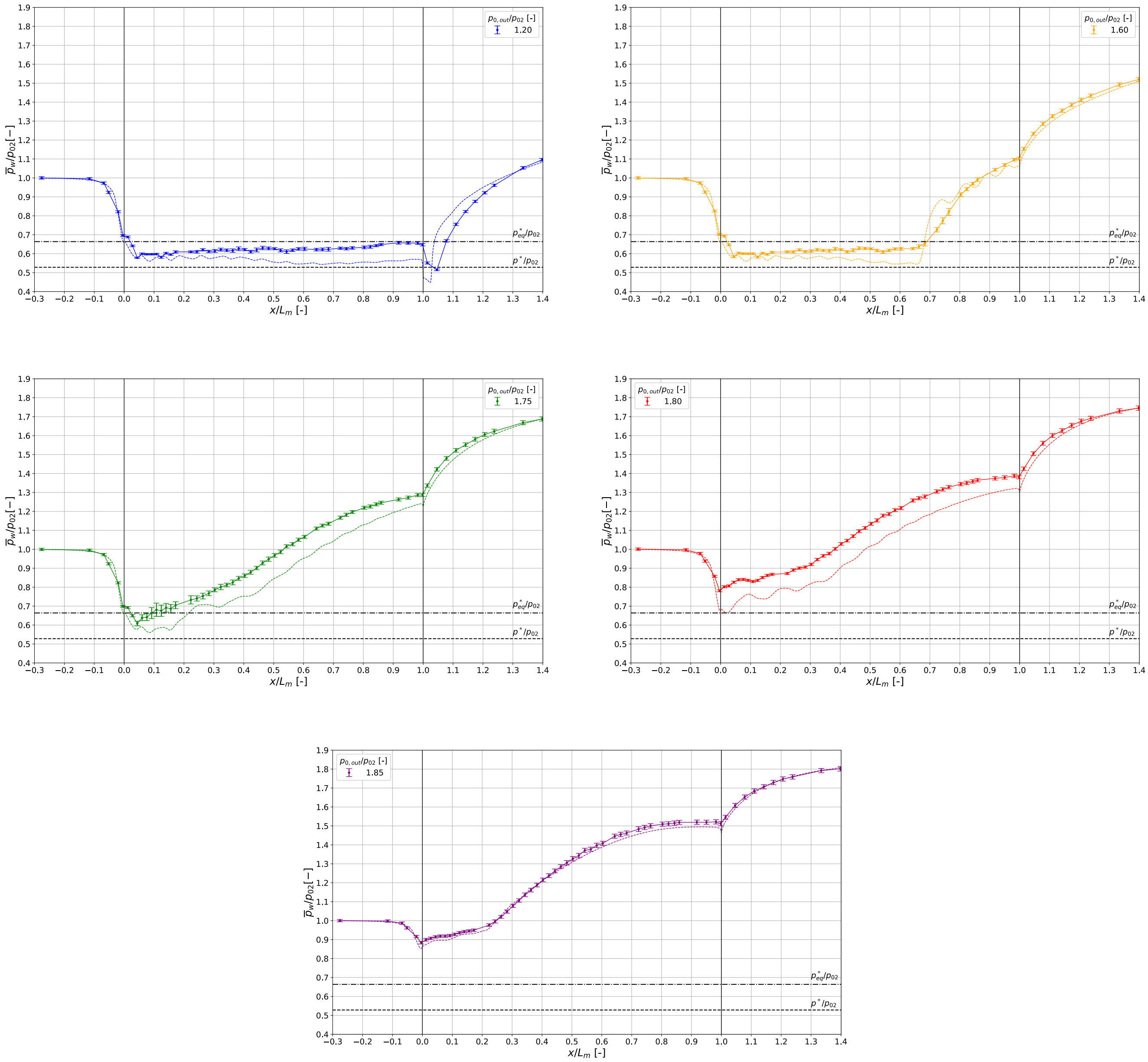

Figure C.9: Pressure profiles for the case $p_{01}/p_{02} = 5$, for each measured outlet condition.

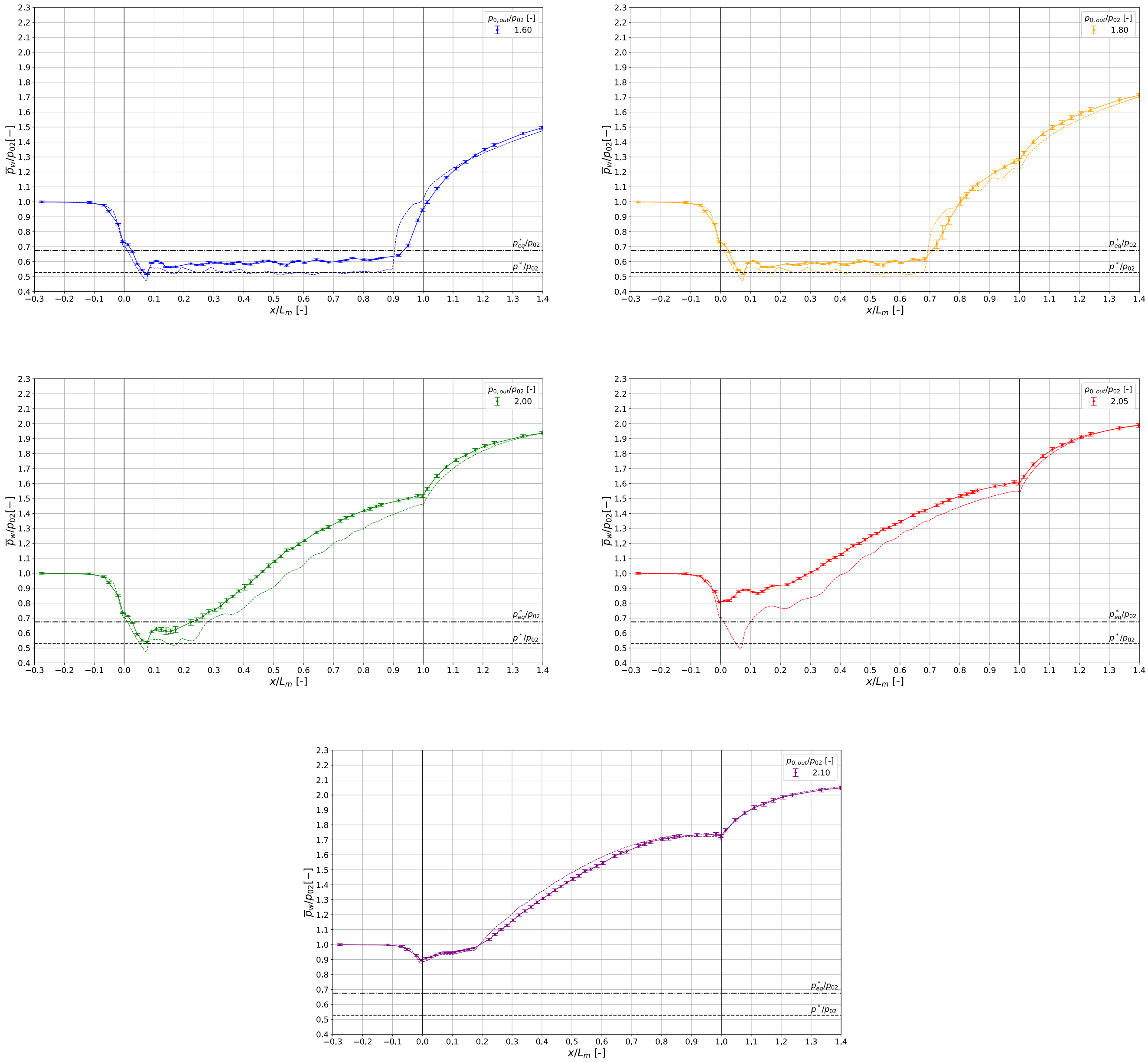

Figure C.10: Pressure profiles for the case $p_{01}/p_{02} = 6$, for each measured outlet condition.

C.4 Comparison with 1D non-isentropic model

The 1D non-isentropic compound-choking model developed by Metsue et al. [14] was briefly explained in subsection 1.2.3. The results obtained by applying this model to the tested operating conditions are displayed along with the experimental and RANS characteristic curves in Figure C.11. The authors did not have the time to perform the fitting of the isentropic efficiencies. Therefore, their value was directly taken from [22].

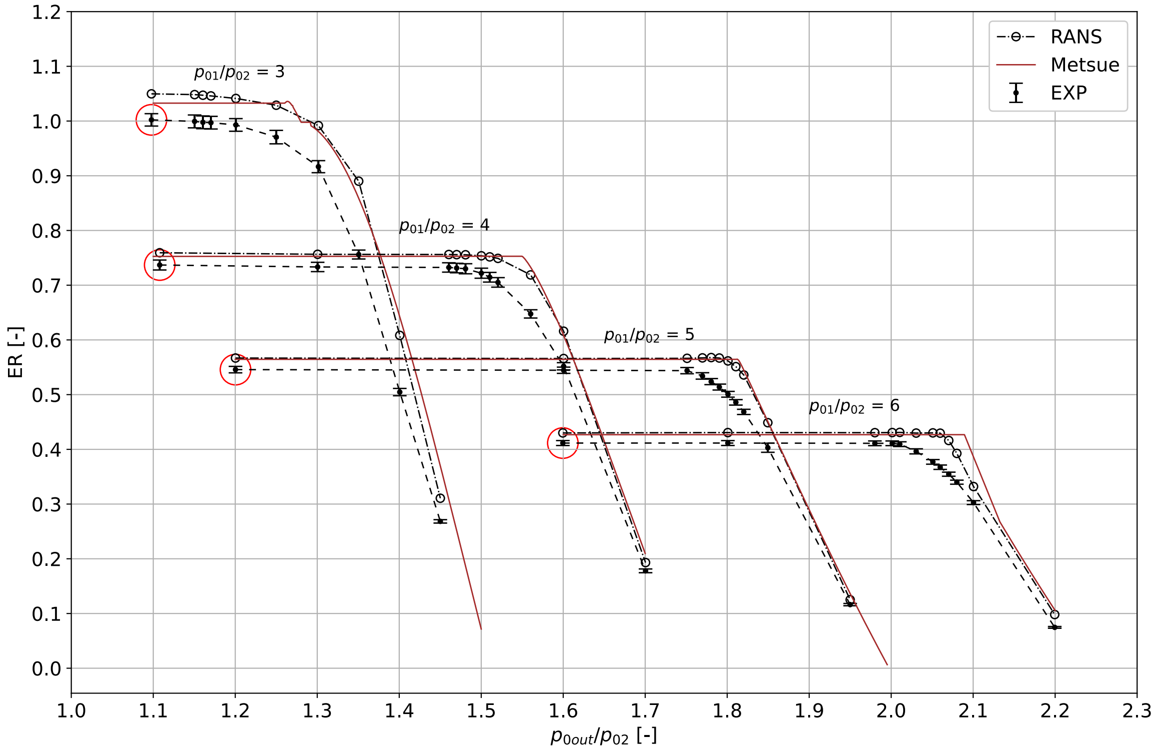

Figure C.11: Experimental and numerical characteristic curves, as well as characteristic curves obtained with the 1D model of Metsue et al. [14], for each of the tested inlet pressure ratios p_{01}/p_{02}.

As explained in [22], the 1D model is in strong agreement with the 2D RANS simulations at $p_{01}/p_{02} = 5$. This scenario is in fact very close to the perfectly expanded case.

Bibliography

[1] A. Hemidi, F. Henry, S. Leclaire, J.-M. Seynhaeve, and Y. Bartosiewicz. CFD analysis of a supersonic air ejector. Part I: Experimental validation of single-phase and two-phase operation. *Applied Thermal Engineering*, 29(8-9):1523–1531, 2009.

[2] S. Elbel and P. Hrnjak. Ejector Refrigeration: An Overview of Historical and Present Developments with an Emphasis on Air-Conditioning Applications. *International Refrigeration and Air Conditioning Conference*, 884, 2008.

[3] J.H. Keenan, E.P. Neumann, and F. Lustwerk. An Investigation of Ejector Design by Analysis and Experiment. *Journal of Applied Mechanics*, 17(3):299–309, 1950.

[4] J. Fabri and R. Siestrunck. Supersonic Air Ejectors. volume 5, pages 1–34. 1958.

[5] A. Bernstein, W.H. Heiser, and C. Hevenor. Coumpound-compressible nozzle flow. *Journal of Applied Mechanics*, 34(3):548–554, 1967.

[6] P. Venkatakrishnan, S. Palani, M. R. Rahamathullah, K. Palani, T. Aridass, and Sathiamourthy. A Review On Historical And Present Developments In Ejector Systems. *International Journal of Engineering Research and Applications (IJERA)*, 3(2):010–034, 2013.

[7] J.T. Munday and D.F. Bagster. A New Ejector Theory Applied to Steam Jet Refrigeration. *Industrial & Engineering Chemistry Process Design and Development*, 16(4):442–449, 1977.

[8] B.J. Huang, J.M. Chang, C.P. Wang, and V.A. Petrenko. A 1-D analysis of ejector performance. *International Journal of Refrigeration*, 22(5):354–364, 1999.

[9] W. Chen, M. Liu, D. Chong, J. Yan, A.B. Little, and Y. Bartosiewicz. A 1D model to predict ejector performance at critical and sub-critical operational regimes. *International Journal of Refrigeration*, 36(6):1750–1761, 2013.

[10] O. Lamberts, P. Chatelain, N. Bourgeois, and Y. Bartosiewicz. The compound-choking theory as an explanation of the entrainment limitation in supersonic ejectors. *Energy*, 158:524–536, 2018.

[11] K. R. Hedges and P. G. Hill. Compressible Flow Ejectors: Part II—Flow Field Measurements and Analysis. *Journal of Fluids Engineering*, 96(3):282–288, 09 1974.

[12] J.H. Keenan and E.P. Neumann. A Simple Air Ejector. *Journal of Applied Mechanics*, 9(2):A75–A81, 1942.

[13] Y. Zhu, W. Cai, C. Wen, and Y. Li. Shock circle model for ejector performance evaluation. *Energy Conversion and Management*, 48(9):2533–2541, 2007.

[14] A. Metsue, R. Debroeyer, S. Poncet, and Y. Bartosiewicz. An improved thermodynamic model for supersonic real-gas ejectors using the compound-choking theory. *Energy*, 238:121856, 2022.

[15] Nor Azwadi Che Sidik, Siti Nurul Akmal Yusof, Yutaka Asako, S. Mohamed, and Arif Aziz. A Short Review on RANS Turbulence Models. *CFD Letters*, 12:83–96, 11 2020.

[16] Pietro Catalano and Marcello Amato. An evaluation of RANS turbulence modelling for aerodynamic applications. *Aerospace Science and Technology*, 7(7):493–509, 2003.

[17] S. B. Riffat, G. Gan, and S. Smith. COMPUTATIONAL FLUID DYNAMICS APPLIED TO EJECTOR HEAT PUMPS. *Applied Thermal Engineering*, 16(4):291–297, 1996.

[18] T. Sriveerakul, S. Aphornratana, and K. Chunnanond. Performance prediction of steam ejector using computational fluid dynamics: Part 1. Validation of the CFD results. *International Journal of Thermal Sciences*, 46(8):812–822, 2006.

[19] S. Croquer, O. Lamberts, S. Poncet, S. Moreau, and Y. Bartosiewicz. Large Eddy Simulation of a supersonic air ejector. *Applied Thermal Engineering*, 209:118177, 2022.

[20] B. Bozkir. *Design and performance analysis of double-flux supersonic air ejector.* PhD thesis, Middle East Technical University, 2018.

[21] O. Lamberts. *Choking and mixing phenomena in supersonic ejectors.* PhD thesis, Université Catholique de Louvain, 2018.

[22] N. Baguet and G. Querinjean. Experimental and numerical characterization of an axisymmetric supersonic ejector. Master's thesis, Université Catholique de Louvain, 2023.

[23] BIPM, IEC, IFCC, ILAC, ISO, IUPAC, IUPAP, and OIML. Evaluation of measurement data — Guide to the expression of uncertainty in measurement. Joint Committee for Guides in Metrology, JCGM 100:2008.

[24] ISO 5167-1:2022(E). Measurement of fluid flow by means of pressure differential devices inserted in circular cross-section conduits running full — Part 1: General principles and requirements. Standard, International Organization for Standardization, Geneva, CH, 2022.

[25] ISO 5167-2:2022(E). Measurement of fluid flow by means of pressure differential devices inserted in circular cross-section conduits running full — Part 2: Orifice plates. Standard, International Organization for Standardization, Geneva, CH, 2003.

[26] Kistler. K-Line Pressure Transmitter. RAG25R. http://web.rfoe.net:8000/SENSORS/ZLXIAZAI/KISTLER/000-080e-08.07.pdf, 2007.

[27] Endress+Hauser. Differential pressure transmitter with metallic measuring cells. Deltabar S PMD75. https://bdih-download.endress.com/files/DLA/005056A500261EDEBF91239D67F5977D/TI00382PEN_3524-00.pdf, 2024.

[28] Endress+Hauser. Pressure transducer with ceramic and metallic sensors. Cerabar T PMP131. https://bdih-download.endress.com/files/DLA/0200030000091ED6BA902E2A9E6B5742/TI00415PEN_2017.pdf, 2017.

[29] Druck. Industrial Pressure Transmitter. PTX1400. https://docs.rs-online.com/77ec/0900766b80114317.pdf, n.d.

[30] Endress+Hauser. Pressure transducer with ceramic and metal sensors. Cerabar PMP21. https://bdih-download.endress.com/files/DLA/005056A500261EEBA4D66CAE6E928480/TI01133PEN_0721.pdf, 2021.

[31] B. L. Welch. *J. R. Stat. Soc. Suppl.*, 3:29–48, 1936. ; *Biometrika* 29:350-362, 1938 ; *ibid.* 34:28-35, 1947.

[32] H. Fairfield-Smith. *J. Counc. Sci. Indust. Res.*, 9(3):211, 1936.

[33] F. E. Sattherthwaite. *Psychometrika*, 6:309–316, 1941. ; *Biometrics Bull* 2(6):110-114, 1946.

[34] J. Huang. A Simple Accurate Formula for Calculating Saturation Vapor Pressure of Water and Ice. *Journal of Applied Meteorology and Climatology*, 57(6):1265–1272, 2018.

[35] M.J. Reader-Harris and J.A. Sattary. The orifice plate discharge coefficient equation - the equation for ISO 5167-1. *Proc. of 14th North Sea Flow Measurement Workshop, Peebles, Scotland*, page 24, 1996.

[36] M.J. Reader-Harris. *Orifice plates and Venturi tubes.* Springer, 2015.

[37] W. Sutherland. LII. The viscosity of gases and molecular force. *Philosophical Magazine Series 5*, 36(223):507–531, 1893.

[38] M.J. Reader-Harris. The equation for the expansibility factor for orifice plates. *Proc. of FLOMEKO 98*, pages 209–214, 1998.

[39] A.M.I. Bin Mamat, A. Romagnoli, and R.F. Martinez-Botas. Characterization of a low pressure turbine for turbocompounding applications in a mild-hybrid gasoline engine. In IMechE, editor, *10th International Conference on Turbochargers and Turbocharging*, pages 281–293. Woodhead Publishing, 2012.

[40] F. Mazzelli, A.B. Little, S. Garimella, and Y. Bartosiewicz. Computational and experimental analysis of supersonic air ejector: Turbulence modeling and assessment of 3D effects. *International Journal of Heat and Fluid Flow*, 56:305–316, 2015.

UNIVERSITÉ CATHOLIQUE DE LOUVAIN
École polytechnique de Louvain
Rue Archimède, 1 bte L6.11.01, 1348 Louvain-la-Neuve, Belgique | **www.uclouvain.be/epl**